Universität Rostock

gegründet 1419

Traditio et Innovatio

Computational Perspectives on Environmental Applications of Two-dimensional Materials

Dissertation zur Erlangung
des akademischen Grades
doctor rerum naturalium (Dr. rer. nat.) der
Mathematisch–Naturwissenschaftlichen Fakultät
der Universität Rostock

Vorgelegt von:
Moyassar Meshhal
Matrikel-Nr.: 219204950

Eingereicht am:
11.12.2023

Betreuer:
Dr. Ashour Ahmed
Prof. Dr. Oliver Kühn

https://doi.org/10.18453/rosdok_id00004724

Universität Rostock | Mathematisch Naturwissenschaftliche Fakultät
Institut für Physik
Albert Einstein Straße 23–24, D–18059, Rostock | Tel: +49–381–498–6961

Gutachter: Prof. Dr. Oliver Kühn, University of Rostock, Institute of Physics
Dr. Ashour Ahmed, University of Rostock, Institute of Physics
Prof. Dr. Thomas Heine, Technical University of Dresden

Tag der Einreichung: 11.12.2023
Tag der Verteidigung: 07.03.2024

Abstract

The escalating environmental challenges of our era demand innovative solutions, and 2D materials emerge as promising candidates with remarkable properties and tunability across diverse applications. This thesis explores the potential of harnessing 2D materials for environmental remediation through three comprehensive case studies.

The first investigation delves into the intricacies of water diffusion confined between graphene oxide (GO) layers, utilizing extended tight-binding (xTB)-based molecular dynamics simulations. Emphasis is placed on the impact of inter-layer H-bonded bridges, revealing novel insights into slowing down water diffusion. These findings not only hold implications for membrane technology but also offer a fresh perspective on selectively permitting species' movement for applications in selective separation processes.

The second case study investigates the behavior of hydrophobic and hydrophilic polymers, including polystyrene, polyethylene, and polyethylene oxide, at the graphene/water interface. Analysis of polymer dynamics uncovers graphene's ability to adsorb polymers, showcasing promise for the effective removal of nanoplastics from aqueous environments. This study not only calls for further exploration of the dynamics of polymers and water at the proximity of graphene and other 2D materials but also introduces valuable insights into understanding the adsorption capacities of graphene and graphene-based 2D materials.

In the third case study, the focus shifts to the potential of antimonene to capture the highly toxic organic molecule, 2,3,7,8-tetrachlorodibenzo-p-dioxin (TCDD). DFT calculations demonstrate the promising capability of antimonene in adsorbing TCDD, with the exploration of different dopants revealing improved performance. These findings not only open avenues for optimizing antimonene properties but also underscore the nuanced effects of doping on the material's capturing capabilities.

Collectively, these case studies contribute to our understanding of 2D materials in environmental remediation, introducing novel insights into water diffusion, polymer adsorption, and toxic molecules capture. The interconnected nature of these studies underscores their potential impact on membrane technology, environmental remediation, and tailored materials design for adsorption purposes. This work marks initial steps towards practical applications, emphasizing the importance of interdisciplinary collaborations and the potential significance of these findings for addressing broader environmental challenges.

Zusammenfassung

Die zunehmenden Umweltherausforderungen unserer Zeit erfordern innovative Lösungen und 2D-Materialien erweisen sich als vielversprechende Kandidaten mit bemerkenswerten und einstellbaren Eigenschaften für verschiedene Anwendungen. Diese Arbeit untersucht das Potenzial der Nutzung von 2D-Materialien für die Bindung von Schadstoffen anhand von drei Fallstudien.

Die erste Untersuchung befasst sich mit den Details der Wasserdiffusion zwischen Graphenoxidschichten (GO) unter Verwendung erweiterter Molekulardynamik-Simulationen auf der Basis eines Tight-Binding Zugangs(xTB). Der Schwerpunkt liegt auf der Auswirkung von H-Brücken zwischen den Schichten und es werdene neue Erkenntnisse zur Verlangsamung der Wasserdiffusion liefern. Diese Erkenntnisse haben nicht nur Auswirkungen auf die Membrantechnologie, sondern bieten auch eine neue Perspektive für Anwendungen in selektiven Trennprozessen.

Die zweite Fallstudie untersucht das Verhalten von Polymeren, einschließlich Polyethylen (PE), Polyethylenoxid (PEO) und Polystyrol (PS), an der Grenzfläche zwischen Graphen und Wasser. Die Analyse der Polymerdynamik deckt die Fähigkeit von Graphen auf, Polymere zu adsorbieren und weist auf eine wirksame Entfernung von Nanoplastik aus wässrigen Umgebungen hin. Diese Studie legt nicht nur eine weitere Erforschung der Dynamik von Polymeren und Wasser in unmittelbarer Nähe von Graphen und anderen 2D-Materialien nahe, sondern liefert auch wertvolle Erkenntnisse zum Verständnis der Adsorptionskapazitäten von Graphen und graphenbasierten 2D-Materialien.

In der dritten Fallstudie verlagert sich der Fokus auf das Potenzial von Antimonen, das hochgiftige organische Molekül 2,3,7,8-Tetrachlordibenzo-p-dioxin (TCDD) zu binden. Dichtefunktionaltheorie-Berechnungen belegen die vielversprechende Fähigkeit von Antimonen zur Adsorption von TCDD, wobei die Untersuchung verschiedener Dotierungen eine verbesserte Leistung ergab. Diese Erkenntnisse eröffnen nicht nur Möglichkeiten zur Optimierung der Antimoneneigenschaften, sondern unterstreichen auch die differenzierten Auswirkungen der Dotierung auf dieAdsorptionseigenschaften an diesem Materials.

Zusammengenommen tragen diese Fallstudien zum Verständnis von 2D-Materialien in umweltrelevanten Anwendungen bei und liefern neue Einblicke in die Wasserdiffusion, Polymeradsorption und das Einfangen toxischer Moleküle. Die Resultate unterstreichen mögliche Einsatzszenarien in der Membrantechnologie, der Umweltsanierung und dem maßgeschneiderten Materialdesign für Adsorptionszwecke. Diese Arbeit markiert einen ersten Schritte in Richtung praktischer Anwendungen und betont die Bedeutung interdisziplinärer Zusammenarbeit.

Acknowledgments

I extend my sincere gratitude to the individuals who have been instrumental in supporting and guiding me during the course of this research. Particularly, Prof. Dr. Oliver Kühn and Dr. Ashour Ahmed. Their invaluable assistance has played a pivotal role in the successful completion of this thesis.

Prof. Dr. Oliver Kühn provided unwavering support, insightful guidance, and mentorship throughout my PhD. His expertise significantly influenced the direction and depth of this work.

My heartfelt thanks go to Dr. Ashour Ahmed for his limitless support from the inception of my PhD journey. I not only consider him my mentor but also a friend and a brother. Having him in my life over the past few years is undoubtedly one of the best gifts I've received.

Acknowledgment is due to my fellow researchers and colleagues for their collaborative spirit and contributions. The discussions and inputs from these individuals have played a crucial role in shaping many ideas and methodologies explored in this thesis.

I am deeply thankful to my family for their unwavering love, encouragement, and understanding throughout this academic pursuit. To my parents, your constant belief in me and sacrifices have been the foundation of my journey. Your unwavering support has been my rock, and I express my deepest gratitude.

To my wife and my son, your patience, love, and understanding have been my greatest source of strength. Your presence has made every challenge more manageable, and I am truly blessed to have you by my side.

I want to pay tribute to Prof. Dr. Ahmed El-Nahas and Prof. Dr. M. H. Elnagdi. Their guidance prior to and during my master's study laid the groundwork for my academic pursuits. I believe that if I had not meet them, I might not have decided to do a PhD and pursue an academic career! Unfortunately, both of them passed away during my PhD journey. Their impact on my intellectual development is immeasurable, and I am forever grateful for the knowledge they imparted.

I want also to convey my heartfelt appreciation to all those who, directly or indirectly,

contributed to this research endeavor. Your support and encouragement have been invaluable and are deeply appreciated.

Finally, I would like to thank the Deutsche Forschungsgemeinschaft (DFG, German Research Foundation) - SFB 1477 ”Light-Matter Interactions at Interfaces” for funding my research.

Contents

1 Introduction 1
1.1 2D Materials: A Revolutionary Era of Materials Science 2
1.2 Properties of 2D Materials 2
1.3 Environmental Applications of 2D Materials 6
1.4 Project Objective 6
1.5 Thesis Structure 7

2 Theoretical Foundations and Computational Methods 9
2.1 Density Functional Theory (DFT) 11
2.1.1 Gaussian Plane Wave (GPW) Method 13
2.2 Extended Tight Binding (xTB) method 14
2.3 Classical Force Field Methods 15
2.4 Molecular Dynamics (MD) simulations 17
2.5 Software Packages and Tools Used in The Study 18

3 Graphene Oxide Membranes and Diffusion of Confined Water 19
3.1 Motivation 19
3.2 Computational Models and Methods 21
3.2.1 Molecular Models 21
3.2.2 Computational details 24
3.3 Results and Discussion 26
3.3.1 Structural Analysis 26
3.3.2 H-Bonds (HBs) Analysis 29
3.3.3 Water Diffusion 32
3.3.4 HBs Bridges and Water Diffusion Mechanism 35
3.4 Summary 39

4 Nanoplastics-Graphene Interaction in Solution 41

- 4.1 Motivation 41
- 4.2 Computational Models and Methods 43
  - 4.2.1 Molecular Models 43
  - 4.2.2 Computational Details 46
- 4.3 Results and Discussion 48
  - 4.3.1 NPs in water 49
  - 4.3.2 NPs on a mono-layer graphene 51
  - 4.3.3 NPs confined between two graphene layers 56
  - 4.3.4 NPs-graphene interaction energies 63
  - 4.3.5 Adsorption of NPs on rigid graphene 67
- 4.4 Summary 68

5 Adsorption of Dioxin on 2D Antimonene 71

- 5.1 Motivation 71
- 5.2 Computational Models and Methods 73
  - 5.2.1 Molecular Models 73
  - 5.2.2 Computational Details 75
- 5.3 Results and Discussion 77
  - 5.3.1 Adsorption of TCDD on pristine and doped antimonene 77
  - 5.3.2 Electronic properties 82
- 5.4 Summary 86

6 Summary and Outlook 89

Appendices 93

A Supplementary Information for Chapter 3 93

- A.1 Chemical reactivity of GO in neat water 93
- A.2 Validation of xTB 94
- A.3 Home-made python scripts for HBs-bridges analysis 96

B Supplementary Information for Chapter 4 101

- B.1 Validating the Adequacy of the produced trajectories 101

C Supplementary Information for Chapter 5 103

- C.1 CP2K input examples: 103
  - C.1.1 General example 103

C.1.2 BSSE calculations . . . 105

D Publications **109**

D.1 Related to The Current Thesis . . . 109

D.1.1 Published . . . 109

D.1.2 In preparation . . . 109

D.2 Other Publications . . . 109

Bibliography **111**

List of abbreviations

DFT density functional theory

SCF self consistent field

GPW gaussian and plane wave

GTH goedecker–teter–hutter

PBE perdew–burke–ernzerhof

LDA local density approximation

GGA generalized gradient approximation

BSSE basis set superposition error

DOS density of states

PDOS partial density of states

DFTB density functional tight binding

xTB extended tight binding

FF force field

MD molecular dynamics

PBC periodic boundary conditions

NVT canonical ensemble
(constant number of atoms, volume and temperature)

NPT isothermal–isobaric ensemble
(constant temperature and constant pressure ensemble)

CSVR	canonical sampling through velocity rescaling
GO	graphene oxide
HB	hydrogen bond
NPs	nanoplastics
NP	nanoplastic
PS	polystyrene
PE	polyethylene
PEO	polyethylene oxide
TCDD	2,3,7,8-tetrachlorodibenzo-p-dioxin

List of Figures

1.1 From left to right: 0D buckyball, 1D carbon nanotube and 2D graphene. . . 1

1.2 A timeline of experimental realization of several recent elemental 2D materials after the isolation of graphene where “Th.” means theoretical. (Glavin et al., 2020) 3

3.1 HB bridge: where one water molecule forms HBs with both GO sheets simultaneously. 21

3.2 GO Models with different arrangement of functional groups. OGO denotes the GO with an ordered distribution of functional groups on the graphene surface, whereas RGO refers to the GO with randomly distributed functional groups. 23

3.3 Hydrated GO Models: (a) GO with 1 layer of confined water, (b) GO with 2 layers of confined water, and (c) GO with 3 layers of confined water. . . . 25

3.4 Visual represntation of the geometrical criteria utilized in the structural analysis presented in this section: (a) d_{CC}, (b) θ_{CCC}, (c) θ_{COC}, and (d) θ_{COH}. . . 27

3.5 Histograms of structural parameters: (a) C-C bonds lengths (d_{CC}), the reference line corresponds to the case of pristine graphene (Khoei and Khorrami, 2016; Delhaes, 2000), (b) C-C-C angles (θ_{CCC}), (c) C-O-C angles (θ_{COC}), (d) C-O-H angles (θ_{COH}). 28

3.6 (Top row) Three types of HBs, O_{ep}, HO_{acc}, and OH_{don}, whose characterization in terms of histograms is given in the lower panels of the respective columns: (a–c) number of HBs; (d–f) donor–acceptor distances $d_{don\text{-}acc}$; (g–i) HB angle $\theta_{acc\text{-}don\text{-}H}$ 31

3.7 Mean square distances (MSD) [blue points] and their linear fits [red lines]. . 33

3.8 Two-dimensional diffusion coefficient of the confined water in our models versus bulk water. Numerical values are given in Table 3.1. 34

3.9 Histograms of the numbers of HB Bridges (bridge/pair of functional groups). Panels (a-c) show the number on nth order bridges in OGOn and RGOn as indicated. 36
3.10 Snapshots of the H-Bonded bridges illustrate the patterns used for classification of the type of HBs that form the bridge. For instance, the pattern $\mathrm{OH_{don}}$ - $\mathrm{OH_{don}}$ (panel (a)) means that the water molecule forms two HBs of type $\mathrm{OH_{don}}$ with the two GO layers simultaneously. 37
3.11 Distributions of R_1 and R_2 values in OH_{don} - OH_{acc} HB bridges of (a) OGO1, (b) RGO1. R_1 is the donor-acceptor distance in the GO-water HB $\mathrm{OH}_{\mathrm{d}on}$, while R_2 is the donor-acceptor distance in the GO-water HB $\mathrm{OH}_{\mathrm{a}cc}$. 38

4.1 Left: the monomers (i.e., building units) from which the NPs were built. Right: initial structures of the corresponding NPs. 44
4.2 Initial NPs-w models. 45
4.3 Simulations boxes of the initial NPs-1L models. 45
4.4 Initial NPs-2L-d. The representative snapshots displayed here are for PE. . . 46
4.5 (a) The radius of gyration and (b) the corresponding SASA of the NPs-w models. 49
4.6 Snapshots of folded NPs in NPs-w models. 50
4.7 (a) The radius of gyration and (b) their corresponding SASA of the NPs-1L models. 51
4.8 Snapshots from the the MD trajectory of PS-1L; (a) depicts the initial configuration post-equilibration, (e) captures the state at the end of simulation, while (b)-(d) showcase intermediate configurations. The water molecules are hidden for clearer visualization of the molecular structure of PS. 52
4.9 Snapshots from the the MD trajectory of PE-1L; (a) depicts the initial configuration post-equilibration, (e) captures the state at the end of simulation, while (b)-(d) showcase intermediate configurations. The water molecules are hidden for clearer visualization of the molecular structure of PE. 53
4.10 Snapshots from the the MD trajectory of PEO-1L; (a) depicts the initial configuration post-equilibration, (e) captures the state at the end of simulation, while (b)-(d) showcase intermediate configurations. The water molecules are hidden for clearer visualization of the molecular structure of PEO. 54

4.11 Partial mass densities along z-axis for NPs and graphene in the NPs-1L models. For better comparison, all partial densities were normalized according to Eq. 4.4. 55
4.12 Snapshots of the NPs-1L models depicting the curved configuration of the graphene surface. Water molecules are omitted for better visualization. . . . 55
4.13 Snapshots of the NPs-1L models showcasing the diffusion of PE in the xy plane on the graphene surface, with configurations: (a) within the first 5 ns, (b) within the second 5 ns, and (c) within the last 5 ns. The water molecules are hidden for clearer visualization. 56
4.14 The R_g of NPs for (a) NPs-2L-10 models, (b) NPs-2L-15 models and (c) NPs-2L-20 models. 57
4.15 Snapshots depicting the NPs in the ultra-confined case (top) versus their folded unconfined analogues (bottom). In the case of NPs-2L-10 models, only one graphene sheet is shown (i.e., the upper graphene layer is hidden) for better visualization of the polymer chains. 58
4.16 The perturbation of the graphene layers (at inter-layer distance of 10 Å) due to PS. 59
4.17 Summary of the average R_g value for the three polymer chains in different environments. The error bars represent the corresponding RMSD values given in Table 4.1 60
4.18 The partial densities along z-axis ($\rho(z)$) for the polymers and graphene in (a) NPs-2L-10 models, (b) NPs-2L-15 models and (c) NPs-2L-20 models. . . 61
4.19 Snapshots depicting the dynamical behavior of the graphene layers in the NPs-2L-d models. 62
4.20 The NPs-graphene interaction energies (E_{int}) for (a) NPs-1L models, (b) NPs-2L-10 models, (c) NPs-2L-15 models and (d) NPs-2L-20 models during the production run (i.e., 15 ns of NVT simulations). 64
4.21 Snapshots of the the two distinct orientations of PS in the PS-2L-20 model. . 65
4.22 Summary of the NPs-graphene interaction energies (i.e., relative E_{int}). 66
4.23 $\rho(z)$ for PEO in the PEO-1L-fix model. Its counterpart in the PEO-1L model is also displayed for comparsion. 67
4.24 PEO-graphene interaction energies (E_{int}) under two conditions: (left) graphene held fixed during the simulation and (right) graphene without any constraints applied. 68

4.25 R_g and SASA results for PEO under two conditions: (left) graphene held fixed during the simulation and (right) graphene without any constraints applied. 69

5.1 Schematic chemical structure of TCDD. 72
5.2 The optimized molecular structures of isolated TCDD, pristine and doped antimonene. 74
5.3 Illustration of the incapability to obtain optimized structures of TCDD perpendicular to the surface of X-doped-antimonene (X=Ca, Ti) through the O atom, and the tendency of these standing configurations to turn to the parallel ones. 78
5.4 Optimized geometries of all considered configurations of the TCDD/Sb and TCDD/doped-Sb complexes. 79
5.5 BSSE-corrected adsorption energies for the complexes depicted in Figure 5.4, their fragments relaxation energies (higher values indicate larger deformation of TCDD upon adsorption), and the corresponding basis set superposition error (BSSE) values. 80
5.6 Top row: charge density difference isosurface plots (color map shows green for charge accumulation, while red is for depletion) of parallel TCDD over antimonene. Bottom row: $\Delta\rho(z)$ and $\Delta Q(z)$ curves of the corresponding isosurface. 83
5.7 DOS of antimonene and doped antimonene. In the bottom row a direct comparison is given. 84
5.8 DOS of pristine and doped antimonene versus their corresponding complexes (only parallel configuration) 85
5.9 PDOS of oxygen (TCDD) and dopant atoms of the doped antimonene. The corresponding total DOS for each system is shown in the background. 86

A.1 (a) Potential energy surface of GO-water-GO H-bonded bridge, and (b) H-bonded bridge model. 95

B.1 (a) The radius of gyration of the NPs-1L models from the longer production run (i.e., extra 50 ns of NVT simulations) and (b) their corresponding SASA. 101

B.2 Partial mass densities along z-axis for NPs and graphene in the NPs-1L models. These results are based on the extended (50 ns of NVT) MD trajectories. For better comparison, all partial densities were normalized according to Eq. 4.4. 102

List of Tables

3.1 Values of the lateral diffusion coefficients, D_{W} ($\times 10^{-5}$ cm^2/s) for bulk water and confined water in the six GO/water models. The table presents results obtained from linear fits of the MSD (cf. Figure 3.7 and Figure 3.8). 34

3.2 Weighted averages of the numbers of HBs bridges (HB bridge/pair of functional groups). The first row contains the sum of all brides patters, whereas the numbers of each pattern are represented in the following rows. 36

4.1 Summary of R_g (Å) and their RMSD values for the three polymer chains in different environments. $<R_g>$ refers to the average R_g. 60

5.1 DFT-calculated structural parameters (namely, C-O, C-C , and C-Cl bonds, and C-O-C angle) of TCDD versus their experimental counterparts. 73

5.2 Lattice and geometrical parameters of the optimized supercells depicted in Figure 5.2. X = Sb, Ni, Ca, or Ti. 75

5.3 Numerical values (in eV) of BSSE-corrected adsorption energies for the complexes depicted in Figure 5.4, their fragments relaxation energies (larger values indicate larger deformation of TCDD upon adsorption), and the corresponding basis set superposition error (BSSE) values. 81

1 Introduction

In the realm of materials science, it has long been believed that the properties and behavior of a material, and consequently its potential applications, are primarily determined by its composition. For instance, the electrical conductivity of metals can be attributed to the presence of metallic bonds among their atoms, which allow electrons to freely drift through the material when an electric field is applied (Simon, 2013). Similarly, the rigidity of concrete is associated with the inclusion of cement that firmly binds incompressible sand and gravel particles together (Mindess et al., 2003). Due to such examples, it was widely assumed that a material's characteristics were solely dependent on its composition.

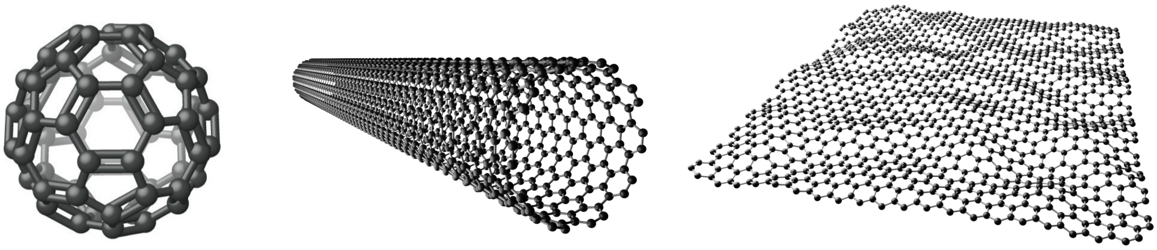

Figure 1.1: From left to right: 0D buckyball, 1D carbon nanotube and 2D graphene.

However, the remarkable discoveries in materials science over the past two decades have highlighted the importance of another factor that can be as influential as the composition of the material, namely, the size of the material, specifically when one or more of its dimensions are reduced to the nanoscale. In this context, materials are categorized based on the number of their nanoscopic dimensions into bulk (three-dimensional, 3D), two-dimensional (2D), one-dimensional (1D), and zero-dimensional (0D) materials (Novoselov et al., 2005). For example, when all dimensions of a material are in the nanoscale (e.g., quantum dots), the material is referred to as a 0D material (also known as a nanoparticle). Conversely, a 1D material, such as a carbon nanotube, has two nanoscopic dimensions, while a 2D material like graphene extends in the xy plane with only the z dimension in the nanoscale. If a material does not have any dimensions small enough to be considered nanosized, it is not classified as a nanomaterial but rather as a “bulk” material, which is the category of materials we encounter in daily life.

1.1 2D Materials: A Revolutionary Era of Materials Science

In 2004, Konstantin Novoselov and Andre Geim succeeded in isolating a single layer of carbon atoms from graphite (Novoselov et al., 2004). Their pioneering work earned them the Nobel Prize in Physics in 2010 and marked the initiation of a new era of materials science, propelling researchers from different disciplines into a race to discover more members of the family now known as 2D materials (Mas-Balleste et al., 2011; Rao et al., 2013), cf. Figure 1.2. The “Scotch tape method”, where layers of graphite are peeled away until only one layer remains, served as the gateway to exploring an array of atomically thin materials (Raidongia et al., 2010; Rao and Nag, 2010).

Shortly after graphene discovery, 2D transition metal dichalcogenides (TMDs) such as MoS_2 and WS_2 were successfully isolated (Novoselov et al., 2005; Heine, 2015). The years that followed witnessed a proliferation of diverse 2D materials. For instance, Pacile et al. reported the synthesis of 2D hBN (Pacile et al., 2008). Furthermore, black phosphorus, often referred to as phosphorene, emerged in 2014 (Liu et al., 2014; Li et al., 2014; Koenig et al., 2014), and was closely followed by the discovery of a range of materials such as antimonene (Ji et al., 2016), $PdSe_2$ (Oyedele et al., 2017), SnSe (Zhao et al., 2016), TaS_2 (Navarro-Moratalla et al., 2016), PdS_2 (Ghorbani-Asl et al., 2016; Zhang et al., 2021), TiS_3 (Island et al., 2016), MoS_3 (Fu et al., 2019), $MoSe_2$ (Duan et al., 2023), and WSe_3 (Kim et al., 2019), each adding to the expansion of the 2D materials family. These materials presented distinctive properties, from thermoelectric behavior to highly anisotropic characteristics, broadening the landscape of 2D materials’ potential applications.

1.2 Properties of 2D Materials

2D materials exhibit a diverse range of remarkable and tunable properties. Their inherent tunability tailored for specific applications renders them well-suited for a multitude of uses, spanning across electronics, optoelectronics, and composite materials, among

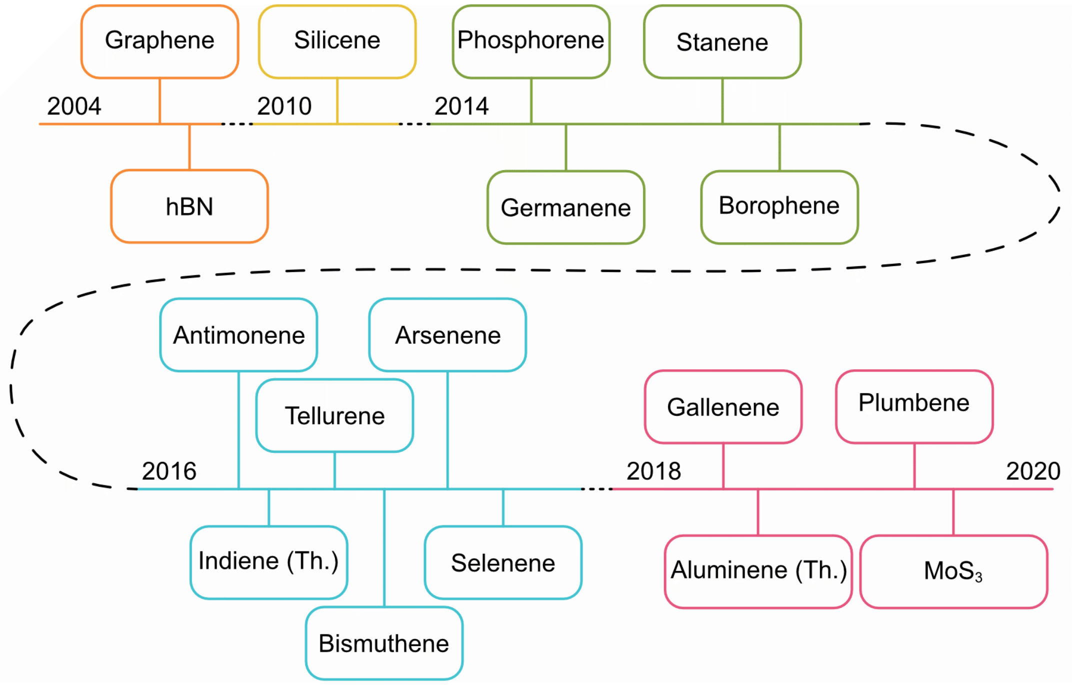
Graphene
Silicene
Phosphorene
Stanene
2004
2010
2014
hBN
Germanene
Borophene
Antimonene
Arsenene
Tellurene
Gallenene
Plumbene
2016
2018
2020
Indiene (Th.)
Selenene
Aluminene (Th.)
MoS3
Bismuthene

Figure 1.2: A timeline of experimental realization of several recent elemental 2D materials after the isolation of graphene where “Th.” means theoretical. (Glavin et al., 2020)

other potential applications. Highlighting this pivotal aspect, the subsequent discussion delves into a number of their key properties and their respective applications.

Electrical Conductivity

Due to their distinctive structural properties, many 2D materials inherently possess high electrical conductivity. This is due to the atomic structure of a single layer, forming a 2D lattice structure, as observed in various references (Xiao et al., 2019; Orts Mercadillo et al., 2022). For instance, graphene, composed of a single layer of carbon atoms in a hexagonal lattice, stands as an excellent example of a highly electrically conductive 2D material. Its structure minimizes defects and impurities, enabling electrons to move with minimal scattering, thus facilitating efficient electrical conduction (Hassan et al., 2023; Orts Mercadillo et al., 2022). Consequently, graphene’s high electrical conductivity positions it as a promising candidate for a wide array of applications, including sensing devices, energy conversion, electronic circuits, and beyond (Hassan et al., 2023; Kumbhakar et al., 2023).

Another notable category of 2D materials that exhibit semiconducting properties and have shown promise for applications in optoelectronics, photodetectors, light-emitting diodes (LEDs), and energy storage devices is TMDs (Heine, 2015; Choi et al., 2017). Their remarkable band structures and excellent electrical transport properties render them particularly suitable for these applications. Unlike metals that conduct electricity freely and insulators that block it entirely, semiconductors possess a bandgap, an energy range where electron conduction is forbidden unless enough energy is supplied to overcome it (Simon, 2013). As semiconducting materials, TMDs may show moderate to high electrical conductivity, which varies based on factors like the number of layers and presence of defects. For instance, TMDs such as monolayer MoS_2 and WS_2 behave as semiconductors, with bandgaps of approximately 1-2 eV, allowing them to conduct electricity when carriers are excited across the bandgap (Liu and Zhang, 2018; Kang et al., 2017). Moreover, multilayer TMDs may demonstrate higher conductivity than monolayers. An example is the increased conductivity of MoS_2 observed as the layer number increases, reaching its peak around 7 layers (Singh et al., 2022).

Certainly, the utilization of the semiconductivity and high electrical conductivity properties within 2D materials serves as a fundamental cornerstone in the ongoing revolution aimed at advancing the development of next-generation electronic devices. This attribute offers the potential for smaller, faster, and more energy-efficient technologies. Moreover, it plays a crucial role in the evolution of next-generation electronics and optoelectronic devices.

Optical properties

The optical properties of 2D materials are a captivating area of study, characterized by their unique responses to light due to their atomically thin structure and quantum confinement effects (Kumbhakar et al., 2021). One of the most prominent optical properties of 2D materials is their strong interaction with light across a broad range of wavelengths (Jia, 2019). Graphene, for instance, exhibits exceptional optical transparency, allowing nearly 97% of visible light to pass through while absorbing only 2.3% of incident light (Falomir et al., 2018; Sheehy and Schmalian, 2009). This property makes graphene an ideal candidate for transparent conductive films used in applications like touchscreens and solar cells. Additionally, other 2D materials like MoS_2 and black phosphorus possess distinct bandgap energies that enable them to absorb and emit light in the visible and even infrared regions, making them suitable for optoelectronic devices such as photodetectors and LEDs (Ermolaev et al., 2020; Chen et al., 2020).

Moreover, 2D materials can exhibit strong photoluminescence and quantum confinement effects due to their thickness (Turunen et al., 2022; Stanford et al., 2018). These properties are particularly advantageous for applications in quantum optics, where single photons and quantum dots are manipulated for quantum information processing and secure communication. By exploiting the unique optical properties of 2D materials, researchers are exploring novel devices such as ultra-compact lasers, optical modulators, and quantum light sources. As our understanding of these optical properties deepens and fabrication techniques improve, the range of applications for 2D materials in photonics and optoelectronics is poised to expand, potentially revolutionizing the way we interact with and harness light for various technological advancements.

Mechanical strength and flexibility

The mechanical strength and flexibility of 2D materials are among their exceptional properties that have drawn significant interest in the realm of materials science and engineering. These characteristics stem from the nature of 2D materials, which consist of a single layer of atoms bonded together in a 2D lattice structure. This atomic arrangement allows them to exhibit remarkable mechanical strength, often exceeding that of traditional bulk materials, while also maintaining extraordinary flexibility (Jiang et al., 2020; Androulidakis et al., 2018; Akinwande et al., 2017).

Graphene is the foremost example of a 2D material renowned for its exceptional mechanical strength. Its tightly packed carbon atoms form strong covalent bonds within the hexagonal lattice, endowing it with remarkable tensile strength and stiffness (Papageorgiou et al., 2017; Shen and Oyadiji, 2020). Graphene's unique combination of strength and flexibility has paved the way for applications in advanced composites, such as reinforced polymers, which enhance the mechanical properties of materials in aerospace, automotive, and construction industries (Zhang et al., 2023; Mohan et al., 2018). Additionally, other 2D materials like MoS_2 and WSe_2 exhibit robust mechanical properties, making them suitable for applications in flexible electronics, wearables, and even as protective coatings (Cui et al., 2022).

The mechanical strength and flexibility of 2D materials hold tremendous promise for creating lightweight yet robust materials and devices. These properties are essential for manufacturing flexible and bendable electronics, lightweight structural components, and even advanced membranes for filtration and separation processes (Jiang et al., 2020;

Androulidakis et al., 2018). As researchers continue to explore and manipulate the properties of 2D materials, the range of applications is expected to expand, revolutionizing various industries that rely on strong yet flexible materials.

1.3 Environmental Applications of 2D Materials

The rapid industrial development in contemporary society has undoubtedly brought numerous advantages, such as technological advancements, economic growth, and improved living standards. However, this progress has come at a cost, leading to significant environmental pollution and energy crises that pose a threat to our planet. Among the most pressing concerns in this context is water pollution, which has far-reaching consequences for both human health and the health of aquatic ecosystems (Kumar et al., 2023a).

To address this critical issue, it is imperative to develop efficient water treatment processes that effectively remove contaminants and promote water recycling. This not only ensures the availability of clean water for human consumption and industrial use but also helps to mitigate the negative impacts of pollution on aquatic life. In this pursuit, the development of materials with high effective surface areas and chemical functionality is crucial (Kumar et al., 2023a).

Due to their unique properties, particularly; their high surface area and tunability of the active sites on their surfaces (Sun et al., 2020), 2D materials can play a pivotal role in many environmental applications, including adsorption and catalytic degradation of pollutants. By harnessing their remarkable properties, we can design innovative water treatment systems that are more effective in removing contaminants and reducing the overall burden of pollution. (Orasugh et al., 2023; Shams et al., 2023) Furthermore, these materials can also contribute to the development of sustainable technologies that minimize waste and promote resource conservation.

1.4 Project Objective

The present research endeavors to shed light on key properties of selected 2D materials, specifically graphene, graphene oxide (GO), and antimonene, with the overarching goal of exploring their applicability in environmentally relevant contexts. A contentious subject within the literature surrounds the diffusion behavior of water confined between bi-layer graphene oxide. Divergent findings exist, with some studies indicating a deceleration in the diffusion of water confined within GO layers, while others contend that the diffusion mirrors that of bulk water. This thesis systematically addresses and investigates this issue, culminating in the proposal of a comprehensive mechanism governing the 2D self-diffusion of water between GO layers. This contributes to our comprehension of the influence of GO and confinement on water diffusion, thereby facilitating the design of more efficient 2D materials-based membranes.

Additionally, the research delves into the interaction between nanoplastics (NPs) and graphene in solution, offering insights into the potential of graphene, as a representative model for 2D materials-based membranes, in capturing NPs from aqueous environments. Lastly, employing DFT calculations, the study explores the potential of antimonene, a recently discovered 2D material, for capturing toxic organic pollutants, specifically dioxins. Through these diverse case studies, the research reveals multifaceted aspects of 2D materials, underscoring their substantial promise as eco-friendly solutions to address a myriad of environmental challenges.

The work involves single point calculations as well as MD simulations using various levels of theory (from quantum mechanics-based approaches such as density functional theory to classical mechanics-based force field methods). The choice of the computational technique and the level of theory to be applied for each piece of work was made based on the system size as well as the target scientific questions. Even though the study is solely computational, comparisons with the available experimental results were done when possible.

1.5 Thesis Structure

The thesis includes five chapters structured as the following; first, the current chapter provides a brief introduction and literature survey about the recent advances in 2D materials and their applications. Afterwards, chapter 2 gives a general overview about the theoretical foundations of the computational methods employed to conduct this project. Finally, the last three chapters (chapters 3 - 5) present the main part of the thesis where the novel work done during this PhD project has been discussed.

2 Theoretical Foundations and Computational Methods

Computational methods have revolutionized materials science, with Density Functional Theory (DFT) Tight Binding (TB) methods, and Molecular Dynamics (MD) simulations playing pivotal roles in advancing our understanding of atomic and molecular-scale material properties. For instance, DFT is a quantum mechanical method that calculates the electronic structure of a material thus providing accurate insights into its energy levels, electronic properties, and reactivity. DFT has proved crucial in the design of semiconductors, insulators, and conducting materials for electronics, as well as the investigation of chemical reactions and catalysis.

Simulating relatively large systems, often comprising thousands of atoms, using quantum mechanics-based methods like DFT can be challenging. In such cases, TB methods offer an efficient compromise between accuracy and computational cost. These methods describe the electronic structure by focusing on the interactions between neighboring atoms and their electron orbitals. By considering only a subset of orbitals, TB methods can efficiently model large systems and extended timescales, making them well-suited for simulating the electronic and transport properties of materials. Examples of the success of TB methods in materials science simulations are their contributions to understanding electronic transport in nanoscale devices, carbon nanotubes, and graphene.

An important aspect of materials' simulations is to study the dynamics of a system. In this context, molecular dynamics (MD) simulations hold a pivotal role employing classical mechanics principles to simulate the motion of atoms and molecules over time. MD simulations provide valuable insights into the dynamic behavior of materials, shedding light on phenomena like phase transitions, diffusion, and mechanical properties. In addition, MD simulations have been pivotal in understanding materials' response to stress, thermal conductivity, and the behavior of biomolecules. They also facilitate the exploration of structural transitions in materials, such as phase changes in solids and liquids.

Combining these methods has led to significant breakthroughs. For example, the coupling of DFT calculations with MD simulations, known as ab initio molecular dynamics (AIMD), enables the study of chemical reactions and structural changes on their natural time scale. DFT calculations can predict the stable configurations and electronic properties of these materials, while MD simulations can explore their thermodynamics and mechanical behavior under varying conditions. Moreover, the importance of these methods lies in their ability to bridge the gap between theoretical predictions and experimental observations, providing a comprehensive understanding of material properties. DFT calculations and TB methods offer insights into the electronic structure that can be compared with spectroscopic measurements, while MD simulations provide information on dynamic properties that can be corroborated by techniques like neutron scattering and NMR spectroscopy.

In the following sections of this chapter, the focus will be solely on the methods employed in the current project: DFT, extended tight binding (xTB), classical force field, and MD simulations. An in-depth derivation of these methods is beyond the scope of this thesis. Therefore, the descriptions provided will be as concise as possible, offering the core concepts of each method. The concluding section of this chapter will discuss the software packages and tools used for simulations and analysis. Notably, most of the information provided draws heavily from foundational textbooks in the field. A brief compilation of these key references is outlined below:

1. Frank Jensen (2016), “Introduction to Computational Chemistry”, John Wiley & Sons.

2. Christopher J. Cramer (2005), “Essentials of Computational Chemistry: Theories and Models”, Wiley.

3. Errol G. Lewars (2016), “Computational Chemistry: Introduction to the Theory and Applications of Molecular and Quantum Mechanics”, Springer.

4. Andrew Leach (2001), “Molecular Modelling: Principles and Applications”, Prentice Hall.

5. David Young (2004), “Computational Chemistry: A Practical Guide for Applying Techniques to Real World Problems”, John Wiley & Sons.

2.1 Density Functional Theory (DFT)

Density Functional Theory (DFT) is a quantum mechanics-based approach widely used in electronic structure calculations in chemistry, materials science, and condensed matter physics. It provides an efficient way to predict the electronic structure and properties of molecules and materials with reasonable accuracy compared to the more expensive wavefunction-based methods. At its core, DFT is based on the idea that the total energy of a many-electron system can be determined from the electron density $\rho(\mathbf{r})$ rather than the complex-valued high-dimensional wavefunction. This simplification drastically reduces the computational complexity of the many-body problem as $\rho(\mathbf{r})$ depends on only three spatial coordinates. In other words, the many-body problem of N electrons with $3N$ spatial coordinates is reduced to three spatial coordinates by expressing relevant quantities such as the energy as functionals of the electron density.

Interestingly, E. B. Wilson argued that the density $\rho(\mathbf{r})$ completely defines the system based on the following ”intuitive” proof:

- The number of electrons is defined by the integral of $\rho(\mathbf{r})$.
- The position of nuclei is defined by the cusps in $\rho(\mathbf{r})$.
- The corresponding nuclear charges are defined by the heights of the cusps.

In DFT, the electronic Hamiltonian ($\hat{H}_{\text{el}}$) for a given system of N electrons and M nuclei consists of electronic kinetic energy ($\hat{T}$), electron-electron repulsion ($\hat{V}_{\text{ee}}$), and an external potential ($\hat{V}_{\text{ext}}$) due to M nuclei:

$$\hat{H}_{el} = \hat{T} + \hat{V}_{\text{ee}} + \hat{V}_{\text{ext}} \tag{2.1}$$

The kinetic energy of the electron system is described by the kinetic energy operator:

$$\hat{T} = -\sum_i \frac{\hbar^2}{2m_e}\nabla_i^2 \tag{2.2}$$

where i indexes the electrons, $\hbar$ is the reduced Planck constant, m_e is the electron mass, and ∇_i^2 is the Laplacian operator. The electron-electron repulsion term accounts for the Coulomb repulsion between electrons and is given by:

$$\hat{V}_{\text{ee}} = \frac{1}{2}\sum_{i \neq j} \frac{e^2}{|\mathbf{r}_i - \mathbf{r}_j|} \tag{2.3}$$

The external potential term ($\hat{V}_{\text{ext}}$) accounts for the interaction of electrons with the nuclei and any external fields. It includes the nuclear attraction term and the interaction with external potentials:

$$\hat{V}_{\text{ext}} = -\sum_{I,i} \frac{Z_I e^2}{|\mathbf{r}_i - \mathbf{R}_I|} + \sum_i v_{\text{ext}}(\mathbf{r}_i) \tag{2.4}$$

where Z_I is the nuclear charge of atom I and $\mathbf{R}_I$ is the position of nucleus I, and $v_{\text{ext}}(\mathbf{r}_i)$ is the external potential acting on electron i.

Modern DFT relies on two principles introduced by Hohenberg and Kohn:

1. The ground-state energy E is a unique functional of the corresponding ground-state electron density $\rho(\mathbf{r})$:
$$E = E[\rho(\mathbf{r})] \tag{2.5}$$
2. The electron density that minimizes the energy of the overall functional is the true ground state electron density:
$$E[\rho(\mathbf{r})] > E_0[\rho_0(\mathbf{r})] \tag{2.6}$$

While DFT is considered an exact approach within the framework of the Hohenberg-Kohn theorems, it relies on an essential but elusive term known as the exchange-correlation (XC) functional, which captures the interactions between electrons and incorporates the exchange-correlation energy (E_{XC}). If the exact form of E_{XC} was known, the total energy $E[\rho(\mathbf{r})]$ could be minimized with respect to the electron density $\rho(\mathbf{r})$, yielding the Kohn-Sham equations that are solved self-consistently:

$$\left[T_{el} + V_{el-nuc} + e^2 \int d^3\mathbf{x}' \frac{\rho(\mathbf{x}')}{|\mathbf{x} - \mathbf{x}'|} + V_{\text{XC}}(\mathbf{x})\right] \phi_a^{ks}(\mathbf{x}) = \epsilon_a^{ks} \phi_a^{ks}(\mathbf{x}) \tag{2.7}$$

where

$$V_{\text{XC}}(\mathbf{x}) = \frac{\delta E_{\text{XC}}[\rho]}{\delta \rho(\mathbf{x})} \tag{2.8}$$

and

$$\rho(\mathbf{x}) = \sum_a |\ \phi_a^{ks}(\mathbf{x})\ |^2 \tag{2.9}$$

The challenge arises from the fact that the precise functional form of E_{XC} is not known, leading to the issue of developing approximations to overcome this obstacle. The pragmatic solution involves constructing approximate XC functionals, which are then integrated into the framework to solve the Kohn-Sham equations iteratively.

Various strategies have been followed to construct DFT functionals. Here, only two of them are briefly mentioned:

1. Local density approximation (LDA): depends solely on the electron density at a given point in space. While LDA can provide reasonable results for certain systems (namely, free electron gas where the density is uniform, e.g. perfect metals), it may fall short in accurately describing systems with varying electron densities and strong electron-electron interactions.

2. Generalized Gradient Approximation (GGA): represents a significant advancement over LDA by incorporating both the electron density and its gradient. By considering the density gradient, GGA accounts for spatial variations in the electron distribution, leading to improved accuracy in predicting molecular properties, chemical reactions, and solid-state phenomena.

In chapter 5, the Perdew-Burke-Ernzerhof (PBE) functional, a member of the GGA class of functionals, has been employed for the DFT calculations. The PBE functional stands out as a non-empirical approach renowned for its favorable performance across diverse systems. Its selection stems from its demonstrated accuracy in capturing the intricate electronic structure and energetics of various materials. Moreover, PBE has exhibited reliable predictions in a wide range of scenarios, making it a well-established choice for addressing the complexities inherent in the systems under investigation in this work. Utilizing the PBE functional ensures robust and insightful insights into the properties and behavior of the antimonene structures explored in this study (Csonka et al., 2009).

2.1.1 Gaussian Plane Wave (GPW) Method

In DFT calculations, the representation of electron density commonly employs two primary approaches: atomic centered basis sets and plane waves basis sets. Atomic centered basis sets, comprising localized functions centered on each atomic nucleus, describe electronic structure in real space. Conversely, plane waves offer a convenient representation of the wavefunction in reciprocal space, providing an efficient basis for periodic systems. Each method exhibits distinct advantages and limitations.

Within the basis set approach, the electronic wavefunction expands in terms of a set of basis functions, expressed mathematically as:

$$\Psi(\mathbf{r}) = \sum_i c_i \phi_i(\mathbf{r}), \tag{2.10}$$

where $\Psi(\mathbf{r})$ is the wavefunction, c_i are expansion coefficients, and $\phi_i(\mathbf{r})$ are basis functions.

Conversely, the plane wave approach represents the wavefunction as a superposition of plane waves:

$$\Psi(\mathbf{r}) = \sum_{\mathbf{G}} c_{\mathbf{G}} e^{i\mathbf{G}\cdot\mathbf{r}}, \tag{2.11}$$

where $\mathbf{G}$ denotes reciprocal lattice vectors, and $c_{\mathbf{G}}$ are coefficients.

The GPW method is an efficient approach to solve the Kohn-Sham equations of DFT. It employs Gaussian functions as the basis set and plane waves as an auxiliary basis. In the GPW method, the entire electron density is represented in the Gaussian basis set, and the density is also taken on a uniform grid in the form of plane waves. The electron density in the Gaussian basis is given by:

$$n(\mathbf{r}) = \sum_{ij} P_{ij}\phi_i(\mathbf{r})\phi_j(\mathbf{r}), \tag{2.12}$$

where P_{ij} are the elements of the density matrix, and $\phi_i(\mathbf{r})$ are the Gaussian basis functions. The plane wave representation of the density, denoted as $\tilde{n}$, is used to calculate the Hartree potential V_{H} and the exchange-correlation potential V_{XC} using a Fast Fourier Transform (FFT) based Poisson solver. These potentials are then transferred back to the Gaussian basis set by integrating them with the product of Gaussian basis functions $\phi_i(\mathbf{r})\phi_j(\mathbf{r})$.

The GPW method uses pseudopotentials, which means that the core electrons are not explicitly treated, and the focus is on the valence electrons. This allows for a more efficient calculation since the core electrons do not contribute significantly to the chemical properties of the system. The pseudopotentials used in the GPW method are typically of the Goedecker-Teter-Hutter (GTH) type, which are optimized for use with CP2K and include all scalar relativistic corrections.

2.2 Extended Tight Binding (xTB) method

GFN1-xTB is, probably, the most common member among the xTB family of methods that have been developed recently by Grimme and co-workers (Grimme et al., 2017). It is described as a semiempirical robust tight-binding approach that is supposed to yield reasonable Geometries, vibrational Frequencies, and Noncovalent interactions (GFN). The ‘x’ stands for extensions in the atomic orbital (AO) basis set. It is based on the Density Functional Tight Binding (DFTB) approximation, which describes the electronic energy E_{el} of a molecule as a functional of its valence electron density $\rho(\mathbf{r})$ (Bannwarth et al., 2021).

The GFN1-xTB Hamiltonian consists of four independent terms: electronic (E_{el}), repulsion (E_{rep}), dispersion (E_{disp}), and halogen-bonding (E_{xb}) interactions. The total energy can be written as:

$$E = E_{\mathrm{el}} + E_{\mathrm{rep}} + E_{\mathrm{disp}} + E_{\mathrm{xb}} \tag{2.13}$$

Each term has its specific functional forms with adjustable parameters (Vicent-Luna et al., 2021). Here, we elaborate on each term of the Hamiltonian:

1. Electronic energy (E_{el}): This term represents the electronic energy of the system, which is a functional of $\rho(\mathbf{r})$. The electronic energy is described within the DFTB approximation, which expands the Kohn–Sham equation in terms of density fluctuations.

2. Repulsion energy (E_{rep}): This term accounts for the pairwise repulsion between atoms in the system.

3. Dispersion energy (E_{disp}): This term represents the long-range dispersion interactions between atoms in the system.

4. Halogen-bonding energy (E_{xb}): This term accounts for the specific halogen-bonding interactions in the system.

The E_{rep}, E_{disp} and E_{xb} terms are modeled using an empirical pairwise potential function, which depends on the interatomic distances and element-specific parameters. In total, GFN-xTB has only 16 global and roughly 1000 element-specific parameters; atom pair related parameters are avoided (Nurhuda et al., 2022).

The method is particularly useful for studying molecular and periodic systems of larger sizes, which are unattainable for standard DFT (Vicent-Luna et al., 2021). For a more detailed description of the GFN1-xTB Hamiltonian, its terms, and their functional forms, one can refer to the original GFN1-xTB article (Grimme et al., 2017).

2.3 Classical Force Field Methods

Among the widely used methods in computational chemistry, computational biology and materials science is the classical force field approximation. Since the energy landscape within a molecular system results from a complex interplay of various interactions, classical force fields rely on using simple mathematical functions that capture these interactions, enabling the study of large systems over relatively long timescales. In this approach, the total potential energy (V_{total}) can be easily calculated as a sum of contributions from bonded and non-bonded interactions, in addition to other terms depending on the level of detail required by the simulation. The potential energy associated with bonded interactions, such as covalent bonds and angles, is often modeled using harmonic potentials. For example, the harmonic bond potential between atoms i and j is given by:

$$V_{\text{bond}}(r_{ij}) = \frac{k_b}{2}(r_{ij} - r_{\text{eq}})^2 \tag{2.14}$$

where k_b is the bond force constant, r_{ij} is the distance between atoms i and j, and r_{eq} is the equilibrium bond length. Similarly, the harmonic angle potential between atoms i, j, and k can be expressed as:

$$V_{\text{angle}}(\theta_{ijk}) = \frac{k_\theta}{2}(\theta_{ijk} - \theta_{\text{eq}})^2 \tag{2.15}$$

where k_θ is the angle force constant, θ_{ijk} is the angle between atoms i, j, and k, and θ_{eq} is the equilibrium angle.

On the other hand, non-bonded interactions, typically van der Waals (VDW) interactions and electrostatic interactions, can be modelled as Lennard-Jones potentials (Eq. 2.16) and Coulomb interactions (Eq. 2.17).

$$V_{\text{VDW}}(r_{ij}) = 4\epsilon_{ij}\left[\left(\frac{\sigma_{ij}}{r_{ij}}\right)^{12} - \left(\frac{\sigma_{ij}}{r_{ij}}\right)^{6}\right] \tag{2.16}$$

where ϵ_{ij} is the VDW energy parameter, σ_{ij} is the VDW radius, and r_{ij} is the distance between atoms i and j.

$$V_{\text{elec}}(r_{ij}) = \frac{q_i q_j}{4\pi\varepsilon_0 r_{ij}} \tag{2.17}$$

where q_i and q_j are the charges of atoms i and j, ε_0 is the vacuum permittivity, and r_{ij} is the distance between the charges.

A simple form of the total potential energy of a system can be written as the sum of the above mentioned bonded and non-bonded interaction terms as the following:

$$V_{\text{total}} = \sum_{\text{bondded}} (V_{\text{bond}} + V_{\text{angle}}) + \sum_{\text{non-bonded}} (V_{\text{VDW}} + V_{\text{elec}}) \tag{2.18}$$

There are several force fields that are widely used such as CHARMM, AMBER, OPLS and many more. In this work CHARMM has been employed to model the dynamics of nanopolymers at the graphene/water interface (see chapter 4). In addition to the above-mentioned interaction terms (Eq. 2.14 - 2.17), CHARMM force field also considers dihedral angles (Eq. 2.19) and improper torsions (Eq. 2.20), which contribute to the torsional energy:

$$V_{\text{dihedral}} = \frac{V_n}{2}\left[1 + \cos(n\phi - \gamma)\right] \tag{2.19}$$

where V_n is the torsional barrier height, n is the periodicity, ϕ is the dihedral angle, and γ is the phase angle.

$$V_{\text{improper}} = k_w(w - w_{\text{eq}})^2 \tag{2.20}$$

where k_w is the force constant and w is the out of plane angle.

The total potential energy in the CHARMM force field MacKerell Jr et al. (1998) can be written as the sum of these contributions:

$$\begin{aligned} V_{\text{total}} = &\sum_{\text{bonds}} V_{\text{bond}} + \sum_{\text{angles}} V_{\text{angle}} \\ &+ \sum_{\text{dihedrals}} V_{\text{dihedral}} + \sum_{\text{impropers}} V_{\text{improper}} \\ &+ \sum_{\text{non-bonded}} (V_{\text{VDW}} + V_{\text{elec}}) + \ldots \end{aligned} \tag{2.21}$$

where additional terms may include contributions from hydrogen bonds, solvation, and other interactions.

2.4 Molecular Dynamics (MD) simulations

Central to MD simulations is the idea that the behavior of a molecular system can be understood by tracking the positions and velocities of its constituent atoms, i.e., propagating the positions and velocities of the atoms (based on classical mechanics) forward in time. In MD simulations, the dynamics of N atoms (nuclei) can be simulated by numerically integrating their classical (Newton's) equations of motion:

$$\frac{d\mathrm{v}_i(t)}{dt} = \frac{\mathrm{f}_i(t)}{m_i} \quad \text{and} \quad \mathrm{f}_i(t) = -\frac{\partial}{\partial \mathbf{r}_i}\mathrm{V}(\mathbf{r}_1, \mathbf{r}_2, \mathbf{r}_3, \cdots, \mathbf{r}_{\mathrm{N}}) \tag{2.22}$$

The system's potential energy is determined by the interactions between these atoms, which can be represented using force fields or more sophisticated quantum mechanical methods. The forces acting on each atom arise from the gradients of the potential energy surface with respect to atomic positions. Regardless of the level of theory employed to calculate the energy and forces, the essence of MD remains rooted in the concept of simulating the motion of particles governed by Newton's laws of motion as mentioned above. Integrating this equation over time enables updating the positions and velocities of the atoms in discrete time steps, hence, revealing the system's dynamic behavior. The numerical algorithms used for this integration, such as the Verlet algorithm, ensures the conservation of energy and accurately represents how the positions and velocities of the atoms evolve over time.

2.5 Software Packages and Tools Used in The Study

For the xTB and DFT calculations (work in chapter 3 and 5, respectively), the CP2K software package (Hutter et al., 2014; Kühne et al., 2020) has been employed, whereas the GROMACS program (Van Der Spoel et al., 2005; Abraham et al., 2015) was used to perform the classical force field MD simulations (work of chapter 4). All the simulations were performed on either the local HPC cluster of our research group (AG: the quantum molecular dynamics group) or on the HPC clusters of the University of Rostock (TITAN and HAUMEA). Programs such as Vesta, VMD and Avogadro were utilized to visualize the 3D chemical structures. The vast majority of pre- and post-processing of the simulations has been done using home-made bash and/or Python scripts.

3 Graphene Oxide Membranes and Diffusion of Confined Water

3.1 Motivation

Considering the extensive body of theoretical and experimental studies investigating its properties and potential applications, graphene oxide (GO) emerges as a particularly prominent member of the family of carbon-based 2D materials. Its unique qualities and capabilities shine brightly, captivating the attention of researchers and innovators alike. A pivotal aspect enhancing GO's fascination lies in the possibility to modify its structure, encompassing variables such as functional groups types, ratio, and spatial arrangement, offering an avenue for precise tailoring. This deliberate structural manipulation opens vistas of opportunity, facilitating the design of a wide spectrum of applications. These applications span a remarkable array of domains, including but not limited to water purification.

The increasing volume of research centered on the GO/water interface structure and processes underscores the necessity of comprehending the nature of the dominant interactions at the interface between GO and water. In contrast to unoxidized carbon-based materials, GO exhibits solubility in water and certain organic solvents, adding to its distinct attributes. However, a comprehensive grasp of the primary interactions governing GO solutions and their alignment with the 2D nature of GO flakes remains unclear.

Notably, the inherent 2D structure of GO presents a challenge in unequivocally understanding the GO solutions from the point of fundamental sciences. According to Dimiev and colleagues (Khannanov et al., 2019; V. Neklyudov et al., 2017), associating the GO solutions' nature and stability with the formal macroscopic parameters is not sufficient for explaining the properties of such solutions. Instead, they advocate for treating GO solutions as genuine solutions, wherein the solution's character is exclusively dictated by the chemical interaction between solute functional groups and solvent molecules. In essence, a profound understanding of the physicochemical properties can be achieved by directing focus toward the GO/liquid interface (Khannanov et al., 2019; V. Neklyudov et al., 2017). This emphasizes the significance of the atomistic modeling of aqueous GO solutions, as evidenced by various studies (Williams and Lísal, 2020; Subasinghege Don et al., 2019; Wei et al., 2014; Hou and Yang, 2018; Chen et al., 2017a).

Particularly, the water transport properties in GO membranes are of great interest, but the results of the relevant studies, as well as their interpretations, are controversial. In this context an important parameter is the inter-layer spacing. Using neutron scattering, Buchsteiner et al. (2006) have reported that the inter-layer spacing in multi-layer GO ranges between 7 and 11 Å depending on the humidity level. Moreover, using X-ray diffraction, Talyzin et al. (2014) have observed that immersion of GO in liquid water increases the inter-layer distance from 8 to 12 Å as a consequence of changing the temperature.

Nair et al. (2012) and Joshi et al. (2014) have reported an extraordinarily swift permeation of water through thick GO membranes, attributing it to the capillary pressure effect resultant from the relatively short inter-layer spacing in their experimental setup (ranging from 6 to 10 Å). These findings found support through MD simulations. In the broader scope, multiple MD studies have probed water transport in GO (Goharshadi et al., 2015; Chen et al., 2017b; Gogoi et al., 2018).

Devanathan et al. (2016) have utilized force field-based MD simulations to compute the diffusion coefficient of water intercalated between GO layers, revealing that the 2D channels between GO sheets (with an inter-layer spacing of approximately 15 Å) reduce water diffusion by an order of magnitude. This phenomenon is ascribed to the presence of plenty hydrogen bonds (HBs) formed between water molecules and the OH groups of GO. In contrast, Mouhat et al. (2020), employing DFT-based MD simulations, have investigated hydrated GO (exhibiting an inter-layer distance around 16 Å) and found that the diffusion of water on the GO surface is similar to that in bulk water.

Interestingly, both Devanathan et al. (2016) and Mouhat et al. (2020) attributed their findings to the role of HBs in controlling the diffusion. According to early NMR studies, a key factor in maintaining the stacked structure of GO could be HBs network (i.e., HBs bridges, cf. Figure 3.1) formed between oxygen functionality on GO and water (Dreyer et al., 2010). Therefore, taking into account the importance of investigating the role of such motif on the diffusion of water confined between GO layers, six GO/water molecular models, differing in the ordering of epoxide and OH groups as well as in the thickness

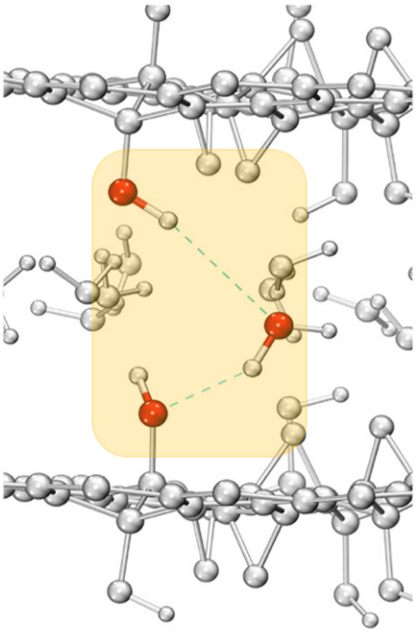

Figure 3.1: HB bridge: where one water molecule forms HBs with both GO sheets simultaneously.

of the water layer, have been constructed and studied. Additionally, results of MD simulations heavily depend on the used forces. DFT and empirical force fields are on opposite when it comes to accuracy and numerical costs. As a compromise, in the present study, MD simulations have been performed using a DFT-based tight binding (TB) method (namely, extended-TB) to investigate the diffusion of water confined between GO sheets.

3.2 Computational Models and Methods

3.2.1 Molecular Models

Although there are plenty of experimental and theoretical studies on the structural properties of GO (Luo et al., 2017; Gómez-Navarro et al., 2010; He et al., 1996; Lerf et al., 1998; Wang et al., 2010; Paci et al., 2007), the issue is still controversial, with many GO models being used currently. For more details about this point one may refer to Sheka and Popova (2013). The state of affairs can be summarized as follows:

1. Various oxygen-containing groups are distributed across the graphene surface, with

a relatively small number of these groups potentially attached to the edges.

2. There appears to be no discernible correlation between the oxygen content and the types of these functional groups.

3. On the basal plane of the graphene sheet, the prevalent oxidants are primarily epoxide (C-O-C) and hydroxyl (OH) groups, while other functional groups like COOH and C=O are predominantly located at the sheet's edges.

4. To date, there is no agreement regarding a specific spatial arrangement of functional groups on the surface of the graphene sheet.

In the present study, the construction of model systems adhered to the general features of the Lerf-Klinowski model (He et al., 1998), which satisfies the aforementioned criteria and is, thus, the most widely accepted model to date. Moreover, the GO models considered here are presumed to encapsulate typical scenarios relevant to the context of the current study.

3.2.1.1 GO Models

Two GO models with identical chemical composition but differences in the spatial arrangement of the functional groups are considered. Starting point is an orthorhombic periodic 6 x 6 supercell of graphene (with initial a and b cell parameters $\approx$ 26.11 Å and 25.12 Å, respectively) consisting of 72 carbon atoms, and, for each, 12 hydroxyl and 6 epoxide groups were grafted on the basal plane of graphene. Hence, the functionalization rate (i.e., O/C ratio) is 25% which is a typical value for GO (Mouhat et al., 2020; Yang et al., 2017; Zhou et al., 2018a). This means that there are 24, out of 72, sp^3 C atoms (i.e., bonded to oxygen-containing functional groups). The OH groups have been systematically placed in a way that two adjacent C atoms bear a pair of OH groups coming out of the opposite sides of the graphene sheet. All the above-mentioned features of the models considered here align with the GO models of Mouhat et al. (2020).

Furthermore, the different spatial arrangement of the functional groups between the two GO configurations presented in the current study (cf. Figure 3.2) captures also the effect of varying the degree of oxidation in certain regions on graphene surface. In other words, the first GO model, labeled OGO and refers to "ordered" GO, features a fully oxidized domain of order arrangement of oxygen functional groups surrounded by a graphene-like region. This choice of GO model is similar to the chain-like structure

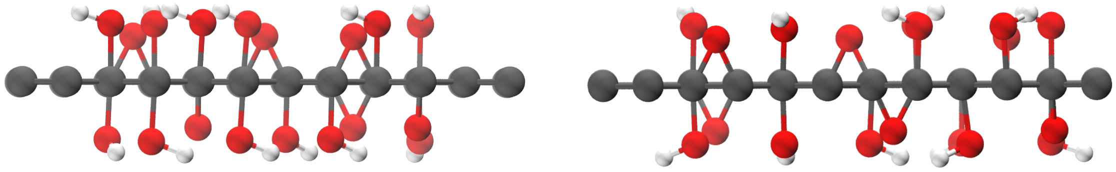

OGO - side view RGO - side view

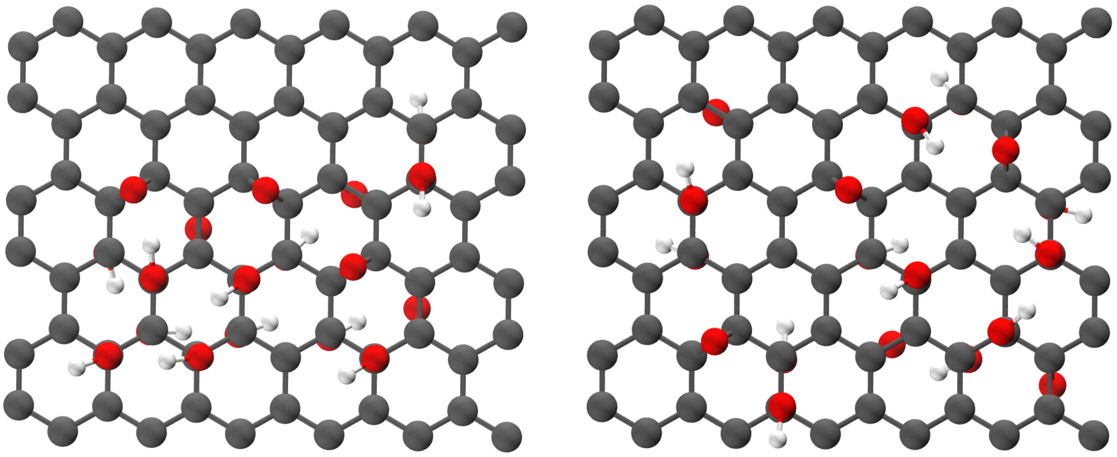

OGO - top view RGO - top view

Figure 3.2: GO Models with different arrangement of functional groups. OGO denotes the GO with an ordered distribution of functional groups on the graphene surface, whereas RGO refers to the GO with randomly distributed functional groups.

described by Yan and Chou (2010). In the second GO model, labeled RGO and refers to "random" GO, the functional groups have been randomly distributed on the graphene surface allowing the oxidized and graphene-like regions intersect each other. Note that these two models present limiting situations and, in principle, a more elaborate model could include averaging with respect to variations in the specific arrangement of the functional groups (Mouhat et al., 2020) or simultaneously occurring random and ordered regions.

3.2.1.2 GO/Water Models

Previous studies modeled the hydrated layered GO using only one GO sheet surrounded by water, assuming that applying PBC would be sufficient to capture the role of confinement on the diffusion of the confined water. However, aiming for a better understanding of the dynamics of water confined between GO layers might require an explicit representation of at least two layers. Therefore, based on each of the aforementioned GO structures (i.e., OGO and RGO), utilizing the PACKMOL software (Martínez et al., 2009), three hydrated models that vary in the number of water layers, from one to three, hence, the inter-layer distances were constructed. A water layer contains 20 molecules, a number chosen based on geometrical consideration to cover the GO surface area. The shortest possible distance between the water molecules and the GO surfaces has been imposed to be at least 2 Å to avoid steric overload because of the functional groups on the surface of GO. The distance between the two GO sheets has been determined based on the number of water layers. It is assumed that the thickness of the water layer in its initial structure $\approx$ 3 Å. Therefore, the inter-layer distance (i.e., the distance between the centers of mass of the two GO sheets in the z direction) in the models with 1-3 water layers has been set to be 8-14 Å.

For technical considerations, namely; applying PBC in all directions (see section 3.2.2 for more details), water was also added above and below the bilayer GO to ensure that the amount of confined water is always the same, taking into account the images of the cell. Having that said, when the number of layers is mentioned in the discussion, it refers to the number of water layers that is confined between the two GO sheets, while the actual amount of water in the simulation cell equals twice that number. From now on, the GO/water models will be refered to as OGOn and RGOn, where n is number of layers of confined water, i.e., $n = 1, 2, 3$ (cf. Figure 3.3).

3.2.2 Computational details

Before delving into technical details, the general workflow of conducting such simulations can be summarized as follows:

1. Geometry optimization and cell relaxation: This step involves optimizing the system's geometry and relaxing the cell parameters in with applying PBC.

2. Equilibration MD simulation: A relatively short MD simulation is carried out for the purpose of equilibration.

3. Production MD simulation: This is the primary phase of the MD simulation. It is important to note that, unless otherwise specified, all subsequent analyses are typically based on the trajectories generated in this step.

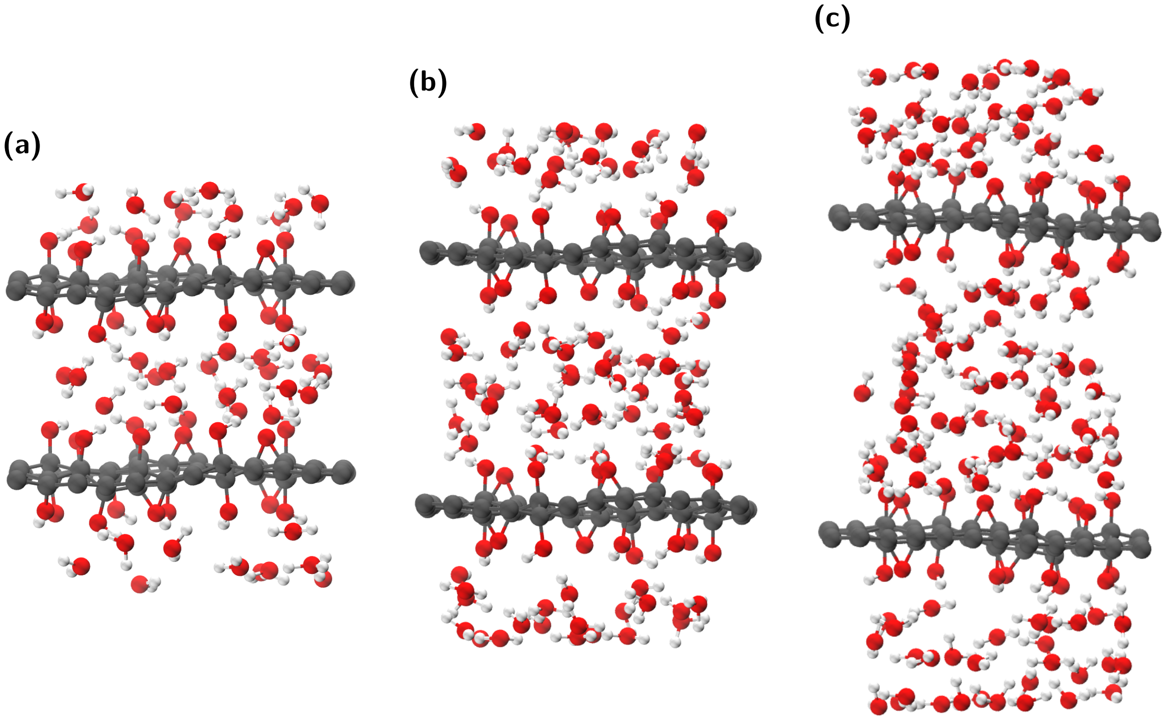

Figure 3.3: Hydrated GO Models: (a) GO with 1 layer of confined water, (b) GO with 2 layers of confined water, and (c) GO with 3 layers of confined water.

In the case of anhydrous GO, only geometry optimization and a cell relaxation are suffecient to adjust the lattice parameters a and b before the production MD run. Adjusting the cell parameters is important since they are expected to vary from those of graphene due to adding the oxygen functional groups that induce a mechanical strain on the graphene surface. Once the GO structures were fully relaxed, 30 ps MD production trajectories have been produced at $T = 300$ K. The simulations were performed with 0.5 fs time step in the NVT ensemble with canonical sampling through a velocity rescaling (CSVR) thermostat (Bussi et al., 2007) with a time constant of 100 fs.

For the hydrated GO systems, the above-mentioned procedure has been followed. The first step, i.e. geometry and cell relaxation simulations, were performed to relax the water molecules and to ensure their proper chemical configuration relative to the GO functional groups. To keep the GO structures preserved in the 2D plane during the hydrated GO cell relaxation, constraints were applied on the a and b cell vectors and only the c vector was allowed to change. A two-stages equilibration routine was carried out. Namely, a 1 ps trajectory was generated using "massive" equilibration (with a time constant of 10 fs) followed by a 5 ps trajectory using “global” equilibration (with a time constant of 100 fs). Finally, a 30 ps production trajectory has been obtained for each hydrated GO system using the same conditions/parameters that described above for the anhydrous systems.

All the main simulations were carried out using the extended tight binding (xTB) method (Grimme et al., 2017) implemented in the CP2K package (Hutter et al., 2014; Kühne et al., 2020). To assess the performance of the chosen method (i.e., xTB), additional simulations were performed using DFT (see, for instance, section A.2 in appendix A). The dispersion correction D3 has been utilized (Grimme et al., 2011). PBC in all directions have been applied in all calculations. The molecular structures and MD trajectories were visualized using the Visual Molecular Dynamics (VMD) software (Humphrey et al., 1996). Furthermore, home-made python scripts utilized in HBs analysis are also given in appendix A. Finally, all the results discussed below belong to the 30 ps production trajectories generated for each of the anhydrous and hydrated GO models.

3.3 Results and Discussion

3.3.1 Structural Analysis

Prior to analysing the dynamics of water and its interaction with GO, this section provides insights into the structure of GO in the presence and absence of water to see whether the presence of water affects the structural stability of GO. This will be done based on four selected geometrical parameters that are supposed to capture most of the structural features of GO. These geometrical criteria are the C-C bond lengths (d_{CC}), C-C-C angles (θ_{CCC}), C-O-C (epoxide) angles (θ_{COC}) and C-O-H (hydroxide) angles (θ_{COH}), cf. Figure 3.4. The distributions of d_{CC} and θ_{CCC} allows us to see how the pristine graphene surface is perturbed due to functionalization with the epoxide and OH groups, while θ_{COC} and θ_{COH} should reveal the behavior of the functional groups themselves and whether water solvation of GO has any role in changing the nature and/or the structure of these moieties.

The results of the distributions of these characteristic structural parameters showed that the surrounding medium does not have any significant effect on the distances and angles of GO in vacuum versus in water, no matter how many water layers are included. Therefore, for the sake of simplicity, only the results for the ordered and random GO

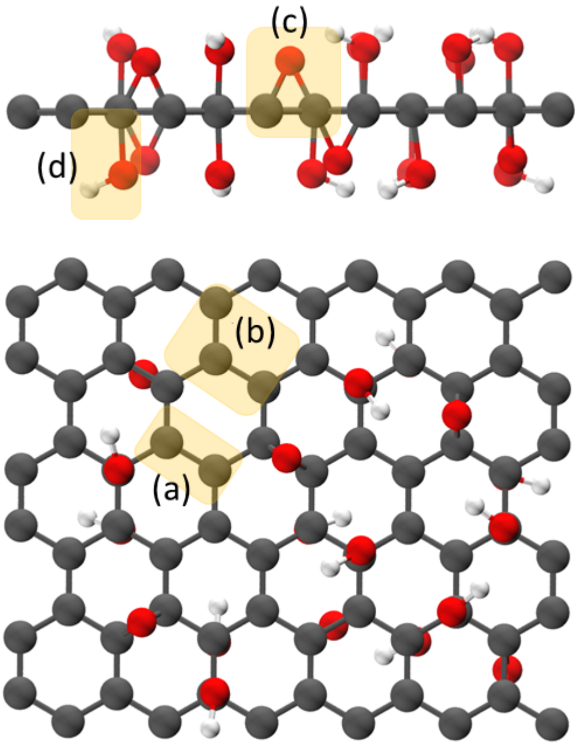

Figure 3.4: Visual represntation of the geometrical criteria utilized in the structural analysis presented in this section: (a) d_{CC}, (b) θ_{CCC}, (c) θ_{COC}, and (d) θ_{COH}.

models in vacuum and for one water layer case for each are presented in Figure 3.5.

One can see how the presence of the functional groups affects the internal structure of the graphene skeleton (i.e., elongating the d_{CC} bond) as shown in Figure 3.5a. In addition, the data of the same Figure reveal the strong dependence of the d_{CC} distribution on the spatial arrangement of the functional groups, at least for the given degree of functionalization. The pronounced peak in the OGO models around the reference value is attributed to the graphene-like domain that is completely distinct from the oxidized part (small shoulder around 1.5 Å). In contrast, in the RGO models the main peak is located around 1.5 Å which is typical for the distance between sp^3 C atoms. Mouhat et al. (2020) reported more diffuse distribution of d_{CC} in random GO models which, to some extent, contradicts to our findings here. The reason behind this discrepancy could be in the difference between the random GO configurations. Specifically, in the present random models, adding functional groups to the edges has been avoided to eliminate the

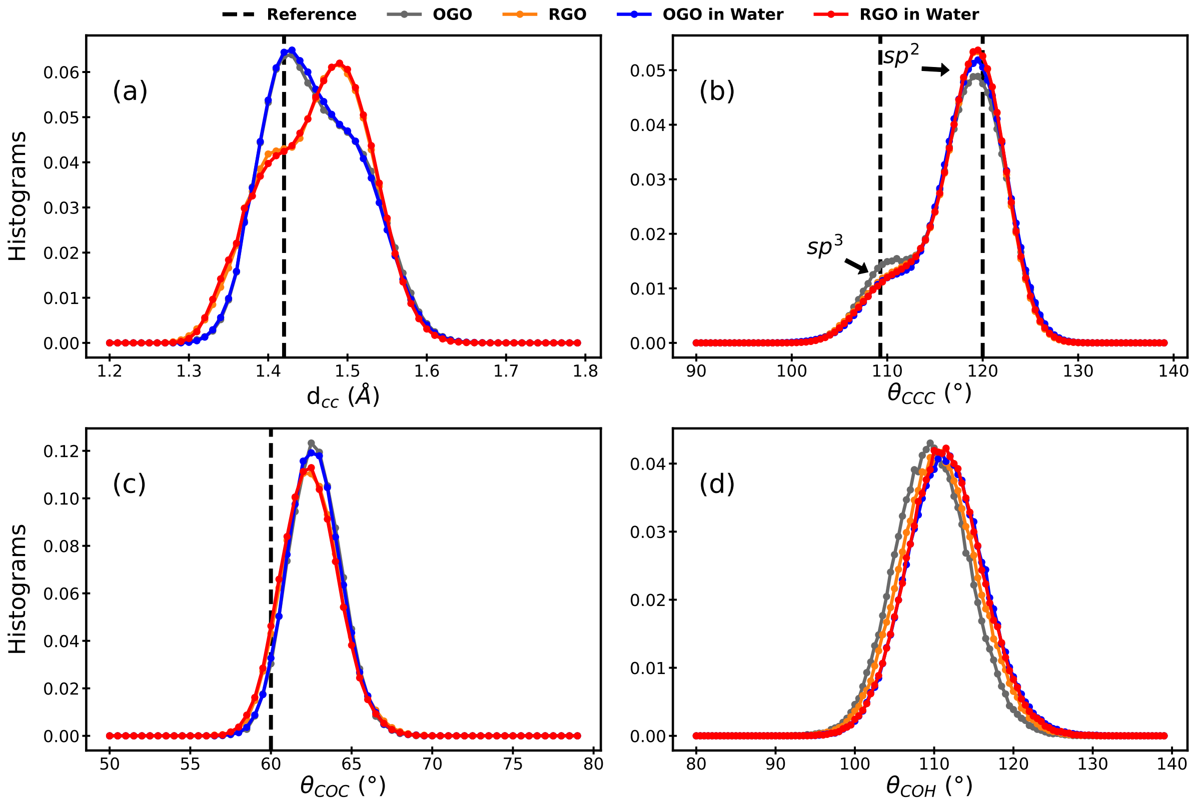

Figure 3.5: Histograms of structural parameters: (a) C-C bonds lengths (d_{CC}), the reference line corresponds to the case of pristine graphene (Khoei and Khorrami, 2016; Delhaes, 2000), (b) C-C-C angles (θ_{CCC}), (c) C-O-C angles (θ_{COC}), (d) C-O-H angles (θ_{COH}).

effect of artificial edges. On the other hand the models studied by Mouhat et al. (2020) did not have such a limitation. That is why the random models of the present study might have relatively large graphene-like region of sp^2 C atoms (cf. Figure 3.2).

Differing from d_{CC}, the histograms of θ_{CCC}, θ_{COC} and θ_{COH} (displayed in panels b, c and d of Figure 3.5, respectively) coincide for the ordered and random GO irrespective of the medium (vacuum vs. water), showing that neither the arrangement of the functional groups nor the surrounding environment affect these geometrical parameters. It is worth noting that the remarkable alignment between the results presented here for θ_{CCC} and, to a significant extent, for θ_{COC} when compared with the results of DFT-based MD simulations conducted by Mouhat et al. (2020) emphasizes the reliability of the xTB method in simulating such systems.

Interestingly, unlike what has been reported by Mouhat et al. (2020), here no peaks were observed at large values for θ_{COC}. The absence of these peaks in the present simulations is attributed to the chemical stability of the epoxide groups in the GO/water models of the current study. In other words, the epoxide groups in models did not exhibit any kind of ring opening through breaking neither the C-C bond nor one of the C-O bonds. One more slight difference between the findings of the present work and those of the aforementioned study (i.e., (Mouhat et al., 2020)) is that the values of the angle θ_{COH} are distributed within a narrower range (100-120°) irrespective of both the order of the functional groups (ordered vs. random) and the medium (vacuum vs. water).

Finally, while most of the θ_{COH} angles in both gas and aqueous phases in the aforementioned study lie in the same range (i.e., 100-120°), Mouhat et al. (2020) also observed a few θ_{COH} angles with slightly higher values in the presence of water. The absence of the higher values of the θ_{COH} angles in the present hydrated GO models is attributed to the ultra-confinement which does not leave enough space for the θ_{COH} to be larger upon forming a HB with water.

3.3.2 H-Bonds (HBs) Analysis

Due to the presence of plenty of oxygen-containing functional groups on its surface, GO has the ability to form HBs with the surrounding water molecules. Based on that fact, various studies (Mouhat et al., 2020; V. Neklyudov et al., 2017; Devanathan et al., 2016) have shown that the chemical and physical properties of the GO/water interface as well as the dynamical behavior of the confined water can be understood, to large extent, in terms of the nature of these HBs. With that in mind, a thorough analysis of HBs through out the MD trajectories of our GO/water models have been carried out .

A HB can be identified based on geometrical criteria (Jeffrey and Jeffrey, 1997). Namely, the donor-acceptor (i.e. O-O) distance (it will be referred to as $d_{\text{don-acc}}$) and the acceptor-donor-H (i.e. ∠O-O-H) angle (will be referred to as $\theta_{\text{acc-don-H}}$). Here, $d_{\text{don-acc}}$ and $\theta_{\text{acc-don-H}}$ were chosen to be ≤ 4 Å and $\leq 30°$, respectively. These criteria serve the purpose of taking into account a wide range of strong to weak HBs (Giese et al., 2006). To facilitate the analysis, the HBs were categorized into three types as depicted in Figure 3.6. This classification is based on the different donors and acceptors. Obviously, the epoxide groups can only accept HBs ($\mathrm{O_{ep}}$), whereas the OH can both accept ($\mathrm{HO_{acc}}$) and donate ($\mathrm{HO_{don}}$) HBs.

The maximum number of HBs of type $\mathrm{O_{ep}}$ per epoxide group is two, while each OH can form up to three HBs, i.e. two $\mathrm{HO_{acc}}$ and one $\mathrm{HO_{don}}$. Additionally, both the intra-molecular HBs (i.e., HBs among functional groups of the same GO sheet) and the inter-molecular HBs (i.e., HBs between functional groups of GO and the surrounding water) were considered. In principle, inter-molecular HBs can also be formed between functional groups of one GO layer and those of the other GO layer, especially in the case of very short inter-layer distance. Nevertheless, only the inter-molecular GO-water HBs have been considered as the dominant kind of interactions at the GO/water interface, in particular, when it comes to water diffusion, due to the tight confinement of water in-between the GO layers. Therefore, the following analysis will focus solely on the inter-molecular GO-water HBs.

Figure 3.6 summarizes the HBs analysis. Given in panels (a-c) are the numbers of the different HBs types (i.e., O_{ep}, HO_{acc} and HO_{don}) as the percentage of their maximum possible counts. Close examination of these data unveils that:

1. Random GO models have greater ability to form more HBs with the H_2O molecules than the ordered models do. The reason behind this is the closer locations of the functional groups of the ordered GO to each other that allow them to form more intra-molecular HBs. Consequently, these intra-molecular HBs compete with the possible inter-molecular HBs that these functional groups could form with water.

2. Irrespective of whether the functional groups are randomly or orderly distributed on the graphene surface, the count of HBs is notably lower in cases of a single layer of confined water compared to those with two or three water layers. This outcome emerges due to the interaction dynamics, where competition exists between the formation of GO-water HBs, on one side, and the HBs that can be formed among water molecules themselves, on the other side.

3. Going from two to three layers of water yields no considerable impact on the count of HBs, unlike the distinction observed between systems of one and two water layers. Based on this observation, it can be inferred that the GO layer forms the maximum number of HBs when beginning with two water layers, while subsequent water layers predominantly engage in forming HBs among water molecules.

4. Particularly in the instance of the random models, the count of HO_{don} exceeds those of HO_{acc} and O_{ep}.

Histograms of the obtained values of the geometric parameters $d_{\text{don-acc}}$ and $\theta_{\text{acc-don-H}}$ are presented in Figures 3.6(d-f) and (g-i), respectively. Similarity between O_{ep} and

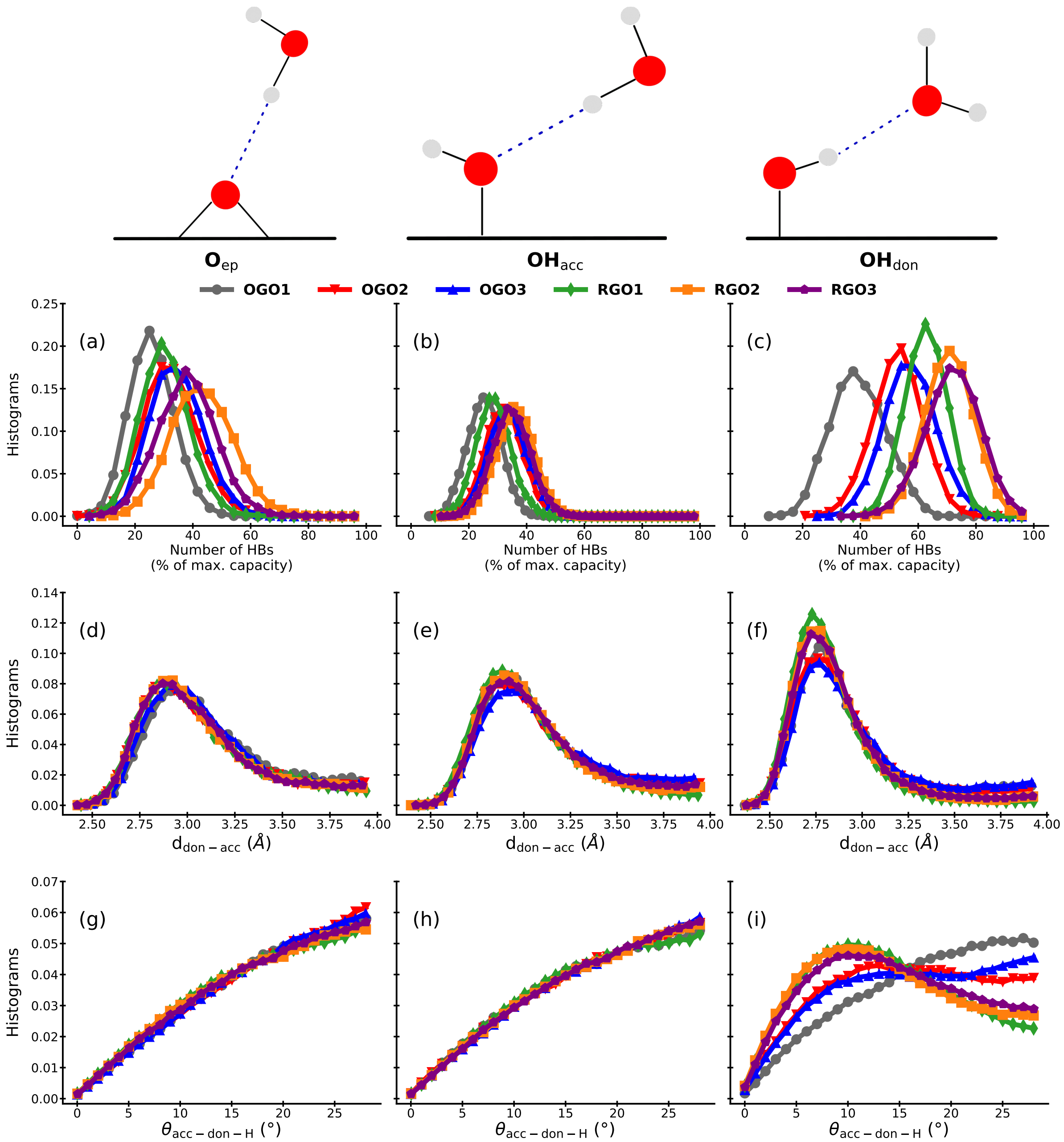

Figure 3.6: (Top row) Three types of HBs, O_{ep}, HO_{acc}, and OH_{don}, whose characterization in terms of histograms is given in the lower panels of the respective columns: (a–c) number of HBs; (d–f) donor–acceptor distances $d_{\text{don-acc}}$; (g–i) HB angle $\theta_{\text{acc-don-H}}$

OH_{acc} has been found. Across all systems, both of these HB types exhibit broad $d_{\text{don-acc}}$ distributions, centered around $2.85 - 2.95$ Å, while $\theta_{\text{acc-don-H}}$ tend to have relatively large values. In contrast, the $d_{\text{don-acc}}$ distributions of the OH_{don} type are notably narrower peaking around 2.75 Å (cf. Figure 3.6f). Furthermore, the distributions of $\theta_{\text{acc-don-H}}$ values of OH_{don} exhibit prominent peaks, particularly in random systems, at approximately 10°. For ordered models the distributions are slightly more diffuse and, particularly in the case of OGO1, resemble the behaviour of the other types of HBs. On the whole, these geometric parameters indicate that the HBs fall within the medium to weak strength range. The linearity of HBs of type OH_{don} suggests a directional binding in case of the RGOn models for the most significant OH_{don} type.

3.3.3 Water Diffusion

The lateral diffusion coefficient, denoted as D_{W}, requires the 2D mean square displacement (MSD) to be computed. Namely, the MSD in the xy plane for the water in between the two GO layers. This has been done as follows:

$$\text{MSD} = \langle |\mathbf{r}(t) - \mathbf{r}(0)|^2 \rangle_{xy} = \frac{1}{N} \sum_{i=1}^{N} (r_i(t) - r_i(0))^2, \tag{3.1}$$

where N and $\mathbf{r}_i$ are the number of MD steps and the atomic coordinates, respectively. Following that, the D_{W} can be estimated from the slope of the linear fit of MSD with respect to time (see Figure 3.7) according to:

$$\text{MSD} = 4D_{\text{W}}t\,. \tag{3.2}$$

The error in the slope has been obtained from the sum of squared residuals of the regression SSR and the time points t_i according to

$$\text{error} = \sqrt{\frac{N}{N-1} \frac{\text{SSR}}{N(\sum t_i^2) - (\sum t_i)^2}} \tag{3.3}$$

Following this procedure, D_{W} of the confined water was calculated for all GO/water models, as well as for bulk water for comparison, (cf. Figure 3.7 and Table 3.1). A value of 1.98×10^{-5} cm^2/s has been obtained for D_{W} of bulk water. This value is about 16% lower than the experimental value of 2.3×10^{-5} cm^2/s (Mills, 1973). Notably, Mouhat et al. (2020), utilizing DFT-based MD simulations, obtained a significantly smaller D_{W} value for bulk water, namely, 0.67×10^{-6} cm^2/s.

The disparity between DFT results and experimental data prompted Pham and coworkers (Pham et al., 2016) to conduct a thorough investigation. They discovered that achieving agreement requires DFT simulations to be conducted at notably higher temperatures (around 400 K) compared to room temperature experiments. In light of this situation, direct quantitative comparison with experimental values is avoided in the present study. Instead, the focus lies on analyzing relative changes in confined water within the established computational framework. The study indicates that the 2D diffusion of confined water slows down significantly, with values ranging from 0.63×10^{-5} to 0.87×10^{-5} cm^2/s for the considered models (refer to Figure 3.8).

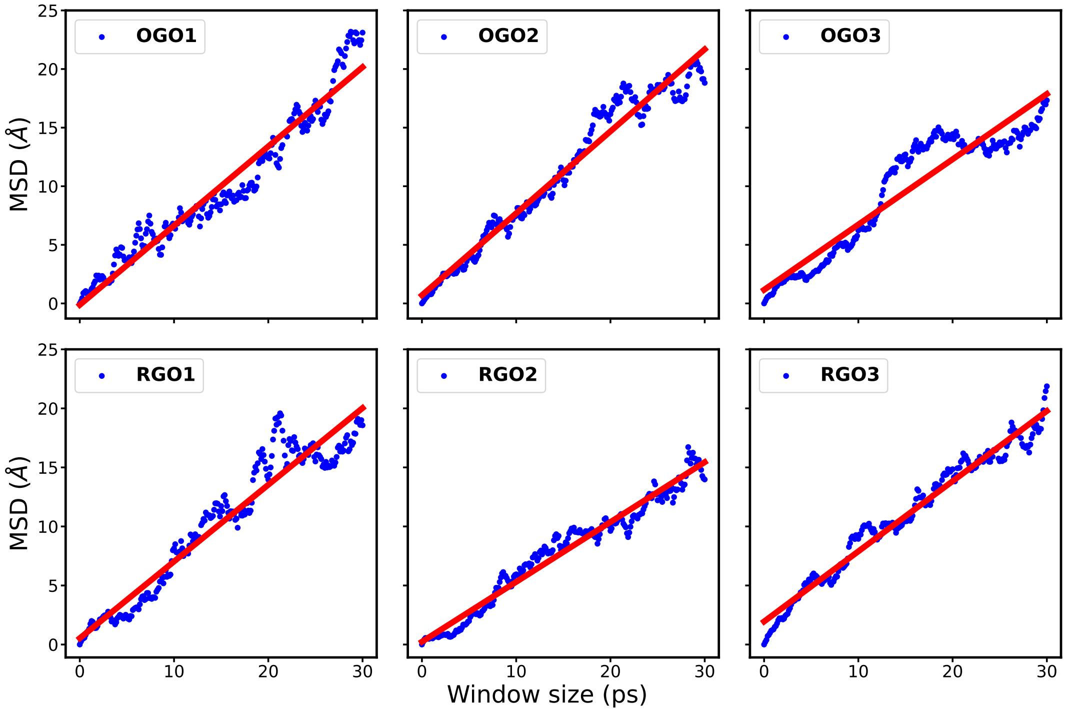

Figure 3.7: Mean square distances (MSD) [blue points] and their linear fits [red lines].

These findings (i.e., diffusion of water confined between GO layers is slower than that of bulk water) align with the results of an earlier study by Devanathan et al. (2016). The authors of that study performed force field MD simulations for hydrated GO and they found that water diffusion in GO is an order of magnitude slower than in bulk water. They attributed this observation to the formation of plenty HBs between the H_2O molecules and the OH groups of GO. On contrary, Mouhat et al. (2020) reported that, based on DFT MD simulations, they did not observe much difference between bulk and confined water. They explained this surprising results in the light of the very dynamic nature of the HBs between the H_2O molecules and the GO functional groups.

In an attempt to shed some light into the issue, in the next section (3.3.4), a thorough

Table 3.1: Values of the lateral diffusion coefficients, D_W ($\times 10^{-5}$ cm^2/s) for bulk water and confined water in the six GO/water models. The table presents results obtained from linear fits of the MSD (cf. Figure 3.7 and Figure 3.8).

Models	D_W
Bulk water	1.98 ± 0.01
OGO1	0.85 ± 0.01
RGO1	0.81 ± 0.01
OGO2	0.87 ± 0.01
RGO2	0.63 ± 0.01
OGO3	0.70 ± 0.02
RGO3	0.74 ± 0.01

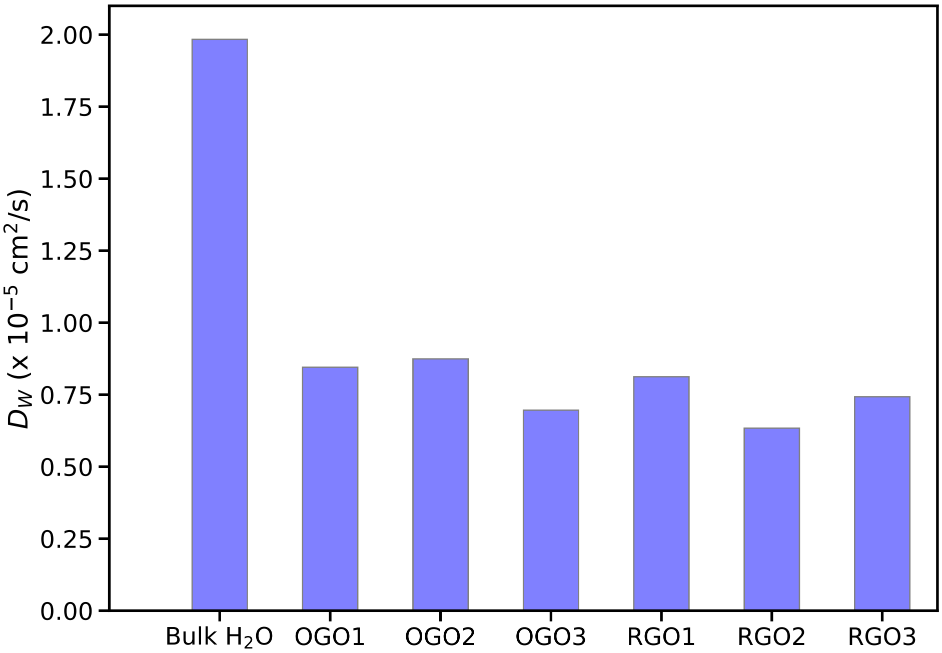

Figure 3.8: Two-dimensional diffusion coefficient of the confined water in our models versus bulk water. Numerical values are given in Table 3.1.

HBs analysis has been done to unravel their role in determining the transport properties of water in the 2D channels between the GO layers. This analysis revealed that while the inter-molecular HBs at the GO/water interface are very dynamic (i.e., the life time of the individual HB is quite short), they can form bridges between the two parallel GO layers. These HB bridges seem to play a crucial role in slowing down the diffusion of the confined water. In the next section, these HB bridges and their role in detail will be discussed.

3.3.4 HBs Bridges and Water Diffusion Mechanism

A HB bridge is defined as a chain of GO-water (and, in some cases, water-water) intermolecular HBs that co-exist and extend from one GO sheet to the other. These bridges will be classified into different types based on the number of involved H_2O molecules. Thereby, an n-th order bridge exists if there are n water molecules bridging the two GO layers. Although longer H-bonded chains may, in principle, exist, the current discussion concentrates on the shortest possible bridge, which is of order n for OGOn and RGOn.

First, the HBs bridges were identified using the geometric criteria given above and counted their occurrence in the corresponding trajectories. Figure 3.9 displays histograms for the investigated bridges in relation to the number of possible donor-acceptor groups (pairs of functional groups on different GO layers close enough to be connected by an n-th order bridge). As can be seen in Figure 3.9a, for the shortest inter-layer distance there is a clear difference between the OGO1 and RGO1 models. The weighted average (given in table 3.2) of the number of bridges/pair of functional groups in the random system RGO1 is 0.93, whereas it is 0.62 for OGO1. Increasing the amount of confined water (hence, the inter-layer distance) from one to two layers increases the probability of forming more HB bridges involving more water molecules. The number of 2nd order bridges in OGO2 increases by about 0.2 as compared to OGO1 (cf. the blue lines in Figure 3.9a vs. 3.9b). In contrast, the number of 2nd order bridges in RGO2 increases only by about 0.01. In general both distributions are broader than in case of a single water layer. Figure 3.9c shows that for 3rd order bridges the difference between the ordered and random systems essentially vanishes in both cases (difference is 0.01). Thus, one can conclude that:

1. the spatial arrangement of the GO functional groups has an insignificant effect on the number of the HBs bridges upon as increasing the distance between GO layers (≥ 12 Å).
2. to have the maximum number of HB bridges, the optimum number of water layers is 1-2 for the random GO, and 2-3 for the ordered GO.

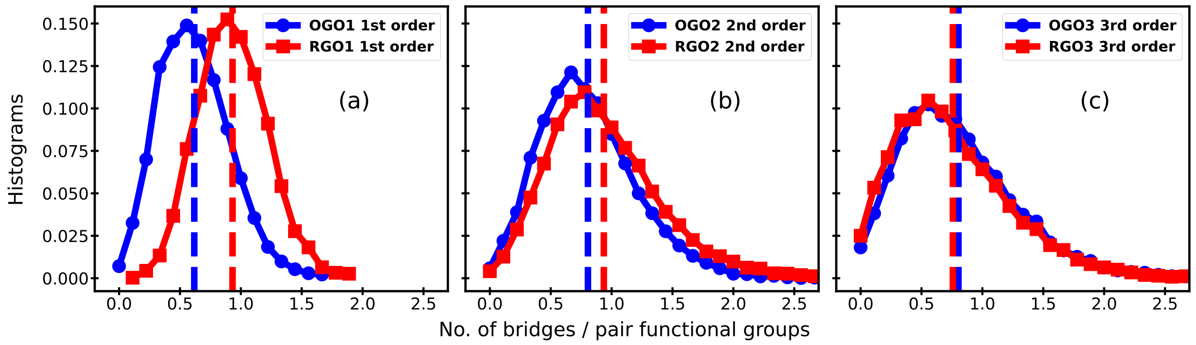

Figure 3.9: Histograms of the numbers of HB Bridges (bridge/pair of functional groups). Panels (a-c) show the number on nth order bridges in OGOn and RGOn as indicated.

To have a better understanding of the dependence of the H-bonded bridges on the different functional groups, they have been categorized into six patterns based on the types of the two terminal HBs (donor and acceptor type according to Figure 3.6). Figure 3.10 displays snapshots of examples of these bridge patterns. The counts of these patterns in each system are given in Table 3.2. From the table one notices that, in all studied models, the OH_{don} - OH_{acc} bridge pattern (cf. Figure 3.10b) has by far the highest occurrence probability (cf. the highlighted row in Table 3.2).

Table 3.2: Weighted averages of the numbers of HBs bridges (HB bridge/pair of functional groups). The first row contains the sum of all brides patters, whereas the numbers of each pattern are represented in the following rows.

Bridge Pattern	OGO1	RGO1	OGO2	RGO2	OGO3	RGO3
All	0.62	0.93	0.81	0.94	0.80	0.76
OH_{don} - OH_{don}	0.04	0.01	0.09	0.06	0.09	0.09
OH_{don} - OH_{acc}	0.23	0.47	0.27	0.28	0.23	0.24
OH_{don} - O_{ep}	0.11	0.26	0.15	0.21	0.13	0.15
OH_{acc} - OH_{acc}	0.10	0.08	0.13	0.10	0.14	0.11
OH_{acc} - O_{ep}	0.11	0.10	0.13	0.15	0.15	0.13
O_{ep} - O_{ep}	0.03	0.00	0.04	0.02	0.06	0.03

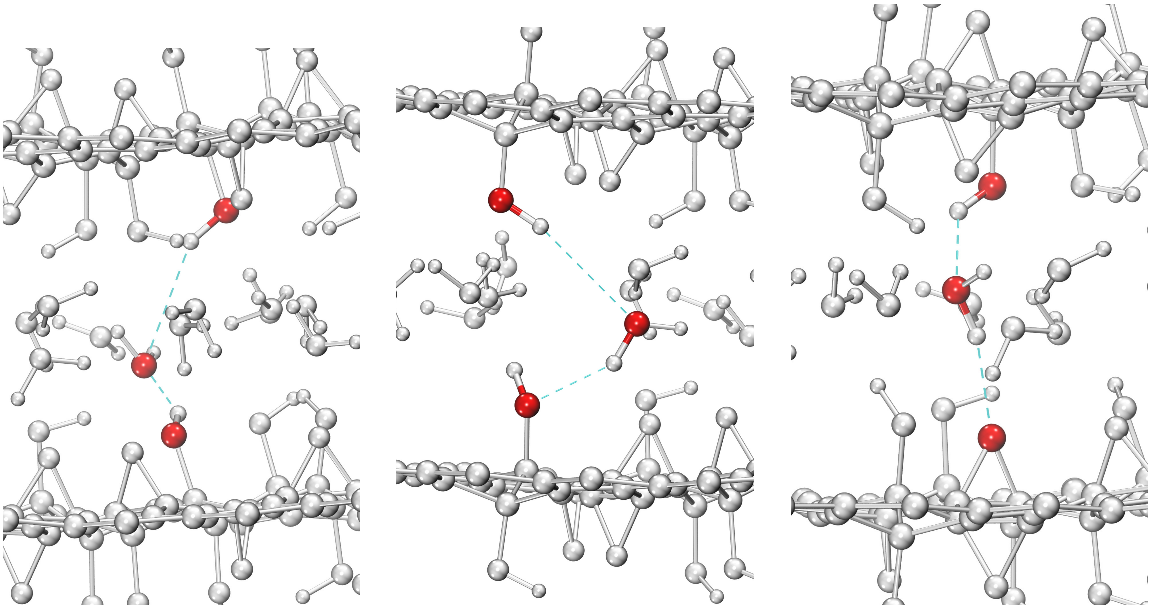

(a) $\mathrm{OH_{don}} - \mathrm{OH_{don}}$ **(b)** $\mathrm{OH_{don}} - \mathrm{OH_{acc}}$ **(c)** $\mathrm{OH_{don}} - \mathrm{O_{ep}}$

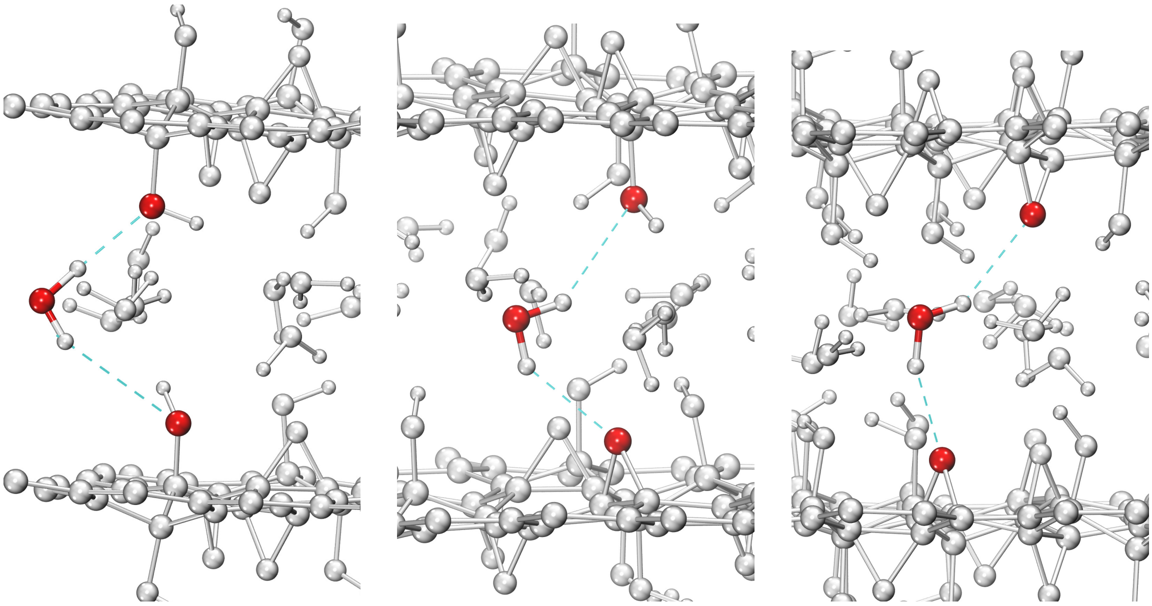

(d) $\mathrm{OH_{acc}} - \mathrm{OH_{acc}}$ **(e)** $\mathrm{OH_{acc}} - \mathrm{O_{ep}}$ **(f)** $\mathrm{O_{ep}} - \mathrm{O_{ep}}$

Figure 3.10: Snapshots of the H-Bonded bridges illustrate the patterns used for classification of the type of HBs that form the bridge. For instance, the pattern $\mathrm{OH_{don}}$ - $\mathrm{OH_{don}}$ (panel (a)) means that the water molecule forms two HBs of type $\mathrm{OH_{don}}$ with the two GO layers simultaneously.

The HBs bridges are very dynamic, i.e., they form and break up many times during the trajectory. Therefore, the focus here is not to quantify their average lifetime. Instead, in order to better understand their effect on water diffusion, the distribution of HB donor-acceptor distances along the trajectory has been investigated. Figure 3.11 shows the result for the dominant OH_{don} - OH_{acc} bridge and the case of a single water layer. Here, R_1 and R_2 is the distance between the oxygen of the bridging water and the oxygen atom in OH_{don} and OH_{acc}, respectively.

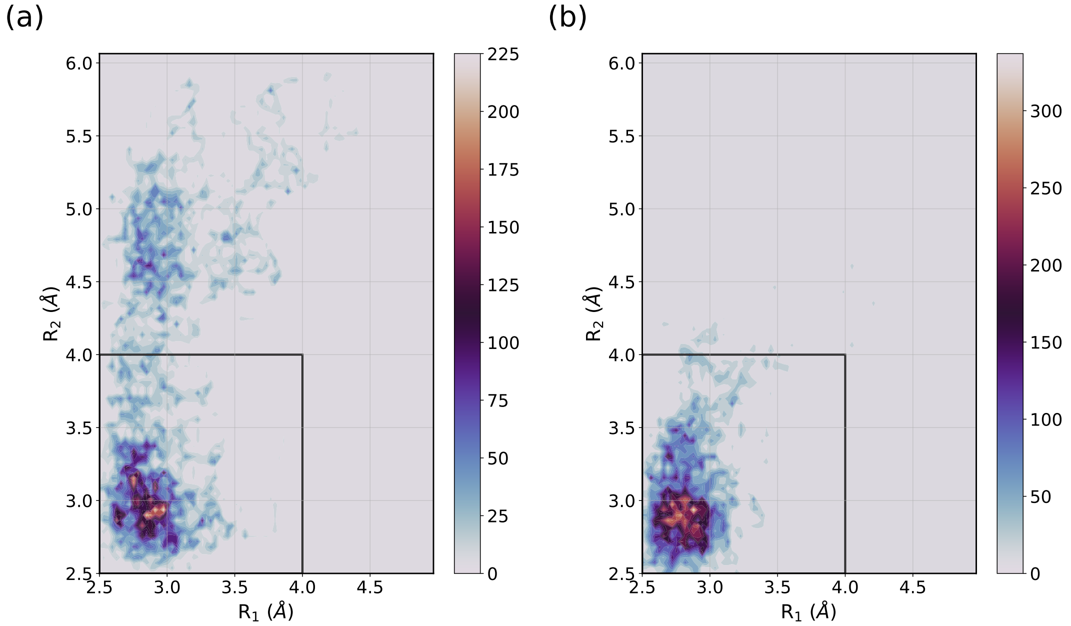

Figure 3.11: Distributions of R_1 and R_2 values in OH_{don} - OH_{acc} HB bridges of (a) OGO1, (b) RGO1. R_1 is the donor-acceptor distance in the GO-water HB OH_{don}, while R_2 is the donor-acceptor distance in the GO-water HB OH_{acc}.

From Figure 3.11 one can conclude that the HB bridge of the random GO (panel (b)) is more stable than its analogue in the ordered GO (panel (a)). Specifically, the OH_{acc} acceptor in the case of OGO1 is weaker than its counterpart in RGO1 (tendency for larger R_2 values). This difference can be traced to the spatial arrangement of the GO functional groups in OGO1, which are closer to each other compared to RGO1. As a result neighboring functional groups on the same GO layer compete with functional groups from the other GO layer to form a HB with the water layer. In both cases the distribution of R_1 values indicates that a H_2O molecule is trapped, either in a HB bridge or at a single GO layer.

The picture emerging from these simulations can be summarized as follows. The ultra-confinement of water between the GO sheets forces the H_2O molecules to come close to the GO functional groups such as to become trapped by forming moderately strong HBs. These HBs form either between functional groups on a single GO layer or as bridges between the confining layers. In the present models the number of the H_2O molecules exceeds the number of available HBs sites on the GO layers. Therefore, a network of inter-molecular HBs between the H_2O molecules is formed. At the same time, this network connects to the bridges formed between the GO layers. This provides a "liberating force" on the trapped H_2O molecules. The competition between the liberating forces and the trapping ones causes the aforementioned dynamic nature of the H-bonded bridges. As a net effect water diffusion in between the confining GO layers is slowed down.

3.4 Summary

The study delved into investigating the properties of two-dimensional water confined between two layers of GO through the application of xTB-based MD simulations. The primary objective was to understand the influence of confinement on water's self-diffusion, an area where previous research had presented conflicting conclusions. Instead of directly comparing different methods and structural models, the study designed six distinct models representing various layer distances and GO functional group orderings. These models, encompassing inter-layer distances within the range of experimentally reported values, employed xTB, which offers an intermediate accuracy level between DFT and force fields.

The analysis revealed that the HBs bridges linking the GO layers had a significant impact on impeding water diffusion. These findings not only elucidate the role of GO layers in affecting water diffusion but also propose implications for membrane technology. Understanding the conditions that promote these HBs bridges and their influence on liquid diffusion at solid-liquid interfaces present opportunities for developing innovative applications, particularly in controlling species movement and separation processes within membranes. The study opens doors for future exploration to comprehend the intricate dynamics at the solid-liquid interface, crucial for various potential applications.

4 Nanoplastics-Graphene Interaction in Solution

4.1 Motivation

Plastics, which are synthetic or semi-synthetic materials primarily composed of polymers, offer numerous advantages such as being lightweight, durable, and cost-effective. These properties make them suitable for a wide array of applications. However, the persistence of plastic waste and its impact on the environment pose significant challenges. In marine ecosystems, plastic waste not only detracts from the aesthetic appeal but can also be ingested by organisms that mistake it for food (Gregory, 2009; Ribeiro-Brasil et al., 2022). It is estimated that around 80% of marine plastic waste originates from land sources (Andrady, 2011; Wang et al., 2019). In terrestrial ecosystems, agroecosystems serve as a primary entry point for tiny plastic particles, which can be linked to the widespread use of plastic mulch and sewage sludge (Baho et al., 2021; Surendran et al., 2023).

Plastic debris can break down into smaller particles, even under ambient conditions (Fotopoulou and Karapanagioti, 2019; Brewer et al., 2020). For instance, nanoplastics (NPs), particles smaller than 1000 nm (Gigault et al., 2016), are prevalent in various environments, including oceans (Ramasamy and Palanisamy, 2021) and freshwater systems across Europe (Sadri and Thompson, 2014), North America (Zbyszewski et al., 2014), and Asia (Free et al., 2014). NPs can originate from various sources, such as the breakdown of larger plastic debris, and the degradation of polymer-based materials (Lai et al., 2022). These tiny plastic particles (i.e., NPs) pose a unique threat to aquatic ecosystems compared to larger plastics. Their high surface area-to-volume ratio makes them prone to adsorb a wide range of contaminants from the surrounding environment (Trevisan et al., 2022). As they disperse throughout aquatic systems, they can act as carriers of harmful pollutants, potentially amplifying their ecological impact.

Furthermore, NPs can be ingested by various aquatic organisms, leading to bioaccumulation in the food web and potentially causing adverse effects on the health of aquatic organisms and humans (Zaki and Aris, 2022).

The persistence of NPs in aquatic environments exacerbates their ecological threat. Unlike larger forms of plastic, which are relatively easier to be removed from water bodies, NPs are difficult to remove due to their size and buoyancy (Kokilathasan and Dittrich, 2022). As a result, they can persist in aquatic ecosystems, continually releasing chemicals and interacting with biota over time. This persistence, combined with their potential to carry pollutants and be ingested by aquatic organisms, highlights the need for further research and effective mitigation strategies to address the growing issue of nanoplastic pollution through understanding their behavior and interactions in aquatic systems.

Experimental studies (Wang et al., 2021a; Mattsson et al., 2018) have provided valuable insights regarding the physical, chemical, and biological behaviors of NPs in aquatic environments, but they are often limited by practical constraints, such as difficulties in tracking NPs at the nanoscale in complex environments (Barbosa et al., 2020). In this regard, MD simulations can be utilized as a powerful tool for complementing the experimental endeavors, hence, improving our understanding of NPs interactions at the atomic and molecular levels (Rama et al., 2023; Shang et al., 2022).

The exploration of advanced materials for the removal and capture of NPs from aqueous environments has become a focal point of research due to the escalating concerns regarding nanomaterial pollution. Among the diverse array of materials investigated for this purpose, graphene emerges as a particularly promising candidate. Graphene's remarkable properties, including its high surface area, exceptional mechanical strength, and unique electronic characteristics, position it as an excellent candidate for various applications, including water purification (Kumar et al., 2023b; Memisoglu et al., 2023). In the context of capturing particles in the nano-scale, graphene holds the promise not only as a material of interest in its own right but also as a representative model for 2D carbon-based membranes. The simplicity and structural integrity of graphene make it an ideal platform for understanding the fundamental interactions between NPs and 2D materials, paving the way for the development of effective nanomaterial capture strategies.

The present study delves into the dynamic behavior of NPs in aqueous solutions, specifically examining the influence of graphene on the dynamics of NPs at the atomic level. Atomistic force field-based MD simulations were conducted for representative NPs models in diverse aqueous environments. The investigation covered scenarios: (1) NPs in bulk water, (2) NPs near a single layer of graphene, and (3) NPs confined between two graphene layers, with varying inter-layer distances. This simple, but adequate, molecular setup allows for a detailed exploration of the intricate interactions between hydrophobic and hydrophilic NPs and graphene in distinct environmental contexts. Analysis parameters, including radius of gyration, solvent-accessible surface area, polymer-graphene interaction energies, and partial densities, offer valuable insights into NPs behavior under these conditions. Additionally, the discussion has considered a comparative analysis with a recent study exploring NPs interactions with carbon nanotubes (Dettmann et al., 2021) to enhance our understanding of the dynamic behaviors exhibited by the investigated NPs in the vicinity of such nanomaterials. This comprehensive exploration aims to contribute to a broader understanding of NPs-nanomaterials interactions.

4.2 Computational Models and Methods

4.2.1 Molecular Models

Several studies have reported that polyethylene (PE) and polystyrene (PS) are among the most abundant pollutants in marine and soil ecosystems (Bläsing and Amelung, 2018; Geyer et al., 2017). Therefore, in the present study, they have been considered as representative models of NPs. In addition, polyethylene oxide (PEO) as a polymer with hydrophilic character has also been included to take into account the hydrophobicity/hydrophilicity effect (Dettmann et al., 2021). Unbranched polymer chains (each consisting of 20 monomers) were considered to model each of the NPs (cf. Figure 4.1).

The subsequent sections will elucidate the construction of three distinct sets of models considered in the present study, namely: NPs in water (referred to as NPs-w), NPs on a mono-layer graphene (referred to as NPs-1L), and NPs between two graphene layers (referred to as NPs-2L-d, where d denotes the inter-layer distance and may assume values of 10 Å, 15 Å, or 20 Å). When mentioning a particular system within any set of models, the same notation will be used with the substitution of NPs by the specific polymer (e.g., PE-w for polyethylene in water).

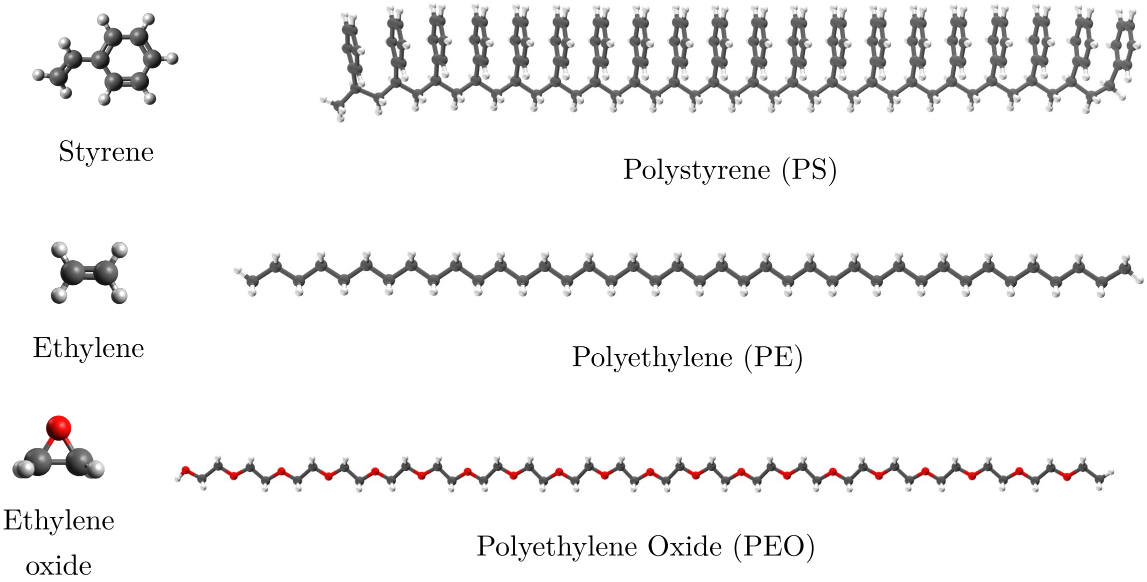

Figure 4.1: Left: the monomers (i.e., building units) from which the NPs were built. Right: initial structures of the corresponding NPs.

4.2.1.1 NPs in water

Prior to investigating the interactions of NPs with graphene, MD simulations for NPs in bulk water have been carried out. This serves as a reference for comparison with models where graphene is included, providing a better understanding of the role of graphene and its impact on the behavior of NPs in aqueous solutions. To prepare the molecular models, using the Packmol program (Martínez et al., 2009), polymers were placed at the center of cubic boxes with a length of 100 Å, each containing a single polymer chain. Lastly, using the GROMACS solvation tool, water of density of 1 g cm^{-3} was added to fill the boxes (cf. Figure 4.2).

4.2.1.2 NPs on a mono-layer graphene

To investigate the interactions between NPs and graphene, first, a single graphene sheet in a simulation box was considered . The simulation boxes (displayed in Figure 4.3) were set up as follows:

- A periodic graphene sheet was created as a supercell of a and b lattice parameters 103.614 Å and 102.552 Å, respectively. Similar to the polymer chains, the graphene sheet was also constructed using the CHARMM-GUI website (Jo et al., 2008).

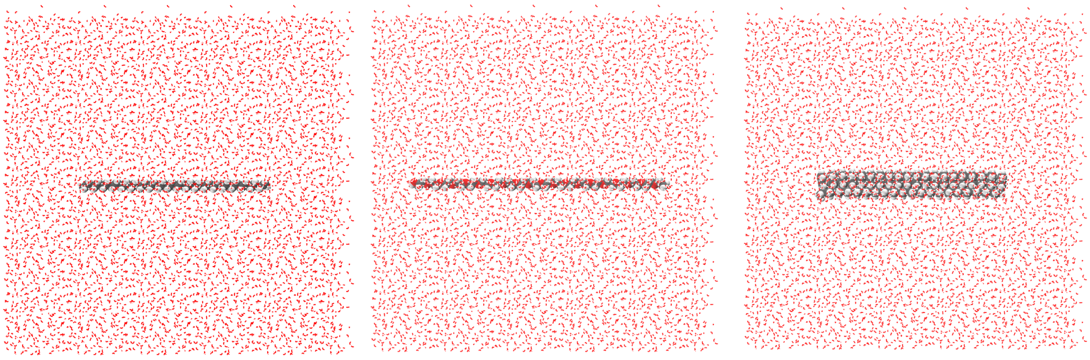

PE-w PEO-w PS-w

Figure 4.2: Initial NPs-w models.

- For each NP type, one polymer chain was positioned at distance ≈ 5 Å above the graphene sheet using the Packmol software package.
- Both the graphene sheet and the polymer were placed in a box with x and y edges that are the same as for a and b of the graphene sheet, and a height (i.e., z edge) of 100 Å. To prevent the graphene sheet from crossing the boundary in z direction, it was raised 5 Å away from the bottom of the box.
- Finally, the box was filled with water of density 1 g cm^{-3} using the GROMACS solvation tool.

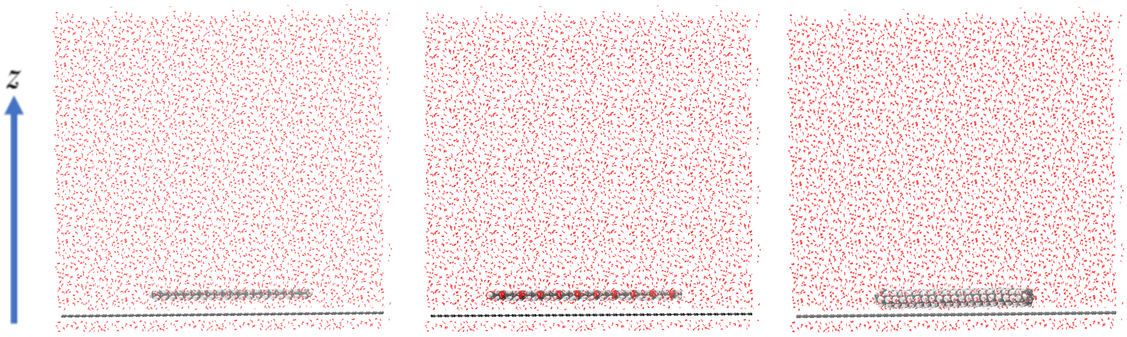

PE-1L PEO-1L PS-1L

Figure 4.3: Simulations boxes of the initial NPs-1L models.

4.2.1.3 NPs between two graphene layers

To further investigate the impact of confinement of NPs between graphene layers, simulation boxes were built with a polymer chain placed between two graphene layers (specifically, the polymer chain was positioned equidistantly between two graphene sheets). Since the inter-layer distance is expected to influence the dynamics of both the confined water and the NPs, various inter-layer spacings (namely, 10 Å, 15 Å, and 20 Å) were considered (cf. Figure 4.4).

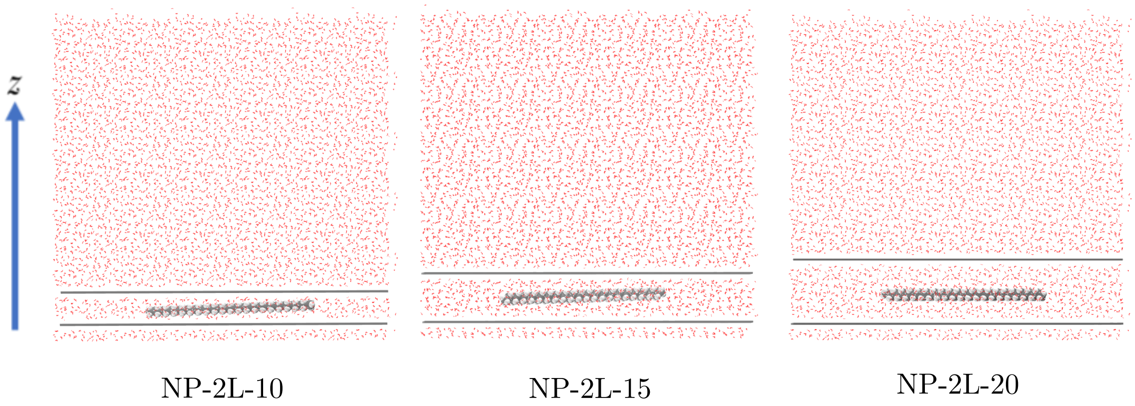

Figure 4.4: Initial NPs-2L-*d*. The representative snapshots displayed here are for PE.

4.2.2 Computational Details

Force field-based MD simulations were performed utilizing the GROMACS software package (Van Der Spoel et al., 2005; Abraham et al., 2015) and using the CHARMM force field (Lee et al., 2016). The CHARMM-GUI (Jo et al., 2008) was utilized to prepare the topology files and obtain CHARMM force field parameters for the NPs and graphene. As mentioned above, the initial simulation boxes were prepared using the Packmol program (Martínez et al., 2009), then, solvated by the TIP3 water model using the GROMACS solvation tool.

Energy minimization was performed for each molecular model, followed by an initial equilibration step consisting of a 500 ps NPT simulation to adjust the box dimensions and reaching the proper densities. Subsequently, a 20 ns NVT simulation was carried out using a timestep of 1 fs. The cutoff distance for intermolecular interactions was set to 12 Å. The velocity rescale thermostat (Bussi et al., 2007) was used to control the temperature, with a coupling constant of 1 ps. To control the pressure in the NPT simulations, the Berendsen barostat with a coupling constant of 1 ps was applied. Furthermore, the compressibility of the system was set to 1 bar. In addition, a temperature of 300 K was used for the simulations in the NPT and NVT ensembles. The Verlet neighbor list scheme was employed in combination with a straight cutoff with a cutoff distance of 12 Å. Three-dimensional periodic boundary conditions (3D PBC) were consistently applied.

It is important to note that each investigated model underwent two equilibration phases: 500 ps of NPT MD simulation followed by 5 ns of NVT MD simulation. Consequently, the production trajectory, forming the basis for all subsequent analyses, was extracted from the last 15 ns of the 20 ns NVT MD simulation for each molecular model. In certain cases, the production run was extended by an additional 50 ns to assess the sufficiency of the initial 15 ns, as will be elucidated later.

4.2.2.1 MD Analysis

GROMACS post-processing tools were utilized to perform the majority of the analysis. Herein, a concise overview for the calculated quantities is presented.

Radius of gyration

The radius of gyration (R_g) describes the compactness of a molecular structure, hence, provides information about the overall size and shape of the polymer. R_g of a polymer is defined as the mean-squared distance of the polymer atoms to their center of mass (COM), $\mathbf{r}_\mathrm{COM}$, i.e.

$$R_\mathrm{g}^2 = \frac{1}{M} \sum_{i=0}^{N} m_i \left\langle (\mathbf{r}_i - \mathbf{r}_\mathrm{COM})^2 \right\rangle \tag{4.1}$$

where m_i and $\mathbf{r}_i$ are the mass and position of the polymer atom i, respectively, N is the number of atoms, and M is the total mass of the polymer.

Solvent Accessible Surface Area

Solvent accessible surface area (SASA) is a measure of the surface area of a molecule (i.e., its exposed surface) that is accessible to solvent molecules. SASA is calculated by imagining a probe sphere (representing a solvent molecule) rolling over the molecular surface. The surface area that is accessible to this probe is then calculated. It is important to note that this approach to calculate the SASA does not distinguish between the surface area accessible to the solvent and that accessible to any other surrounding group (e.g., graphene in the current study). Essentially, it assumes the presence of only the solvent surrounding the polymer.

Interaction Energies

To characterize the strength of interaction/binding of NPs to graphene, interaction energies E_{int} were calculated as the sum of the Lennard–Jones interactions:

$$E_{\text{int}} = \sum_{i<j} 4\varepsilon_{ij} \left[\left(\frac{\sigma_{ij}}{|\mathrm{r}_{ij}|} \right)^{12} - (\left(\frac{\sigma_{ij}}{|\mathrm{r}_{ij}|} \right)^{6} \right] \tag{4.2}$$

where r is the distance between two interacting particles (i.e., i and j), ε_{ij} is the Lennard–Jones parameter (the depth of the potential well), and σ_{ij} is the distance at which the particle-particle potential energy is zero. These energies were calculated via energy groups using GROMACS tools and the cutoff for the Lennard–Jones interaction was set to 12 Å.

Partial Densities

The partial density profiles of the NP particles along the separate axis (i.e., x, y and z) have been calculated. For instance, given the full density $\rho(\mathbf{r})$, the density profile along z-dimension $\rho(z)$ of the box (i.e., norm of graphene xy plan) is defined as:

$$\rho(z) = \iint \rho(\mathbf{r}) dx dy \tag{4.3}$$

For a better comparison between the different polymer types, the resulting partial density distribution was normalized by its numerically calculated integral along the box:

$$\rho(z) = \frac{\rho(z)}{\int \rho(z) dz} \tag{4.4}$$

4.3 Results and Discussion

The results and discussions presented in this study are primarily based on 15 ns NVT MD simulations conducted after two equilibration phases, as detailed earlier. However, for models involving the presence of a polymer chain in the proximity of a single graphene layer (i.e., NPs-1L models), extended 50 ns NVT MD simulations were performed to validate the adequacy of the 15 ns trajectories otherwise used. A comparative analysis between the results of both short and long runs revealed that 15 ns trajectories are sufficient for the current investigation. Consequently, the discussion related to these models (in section 4.3.2) predominantly relies on the results extracted from the 15 ns trajectories to ensure consistency with the other model sets. The results of the extended trajectories are provided in the appendices for reference (see section B.1).

4.3.1 NPs in water

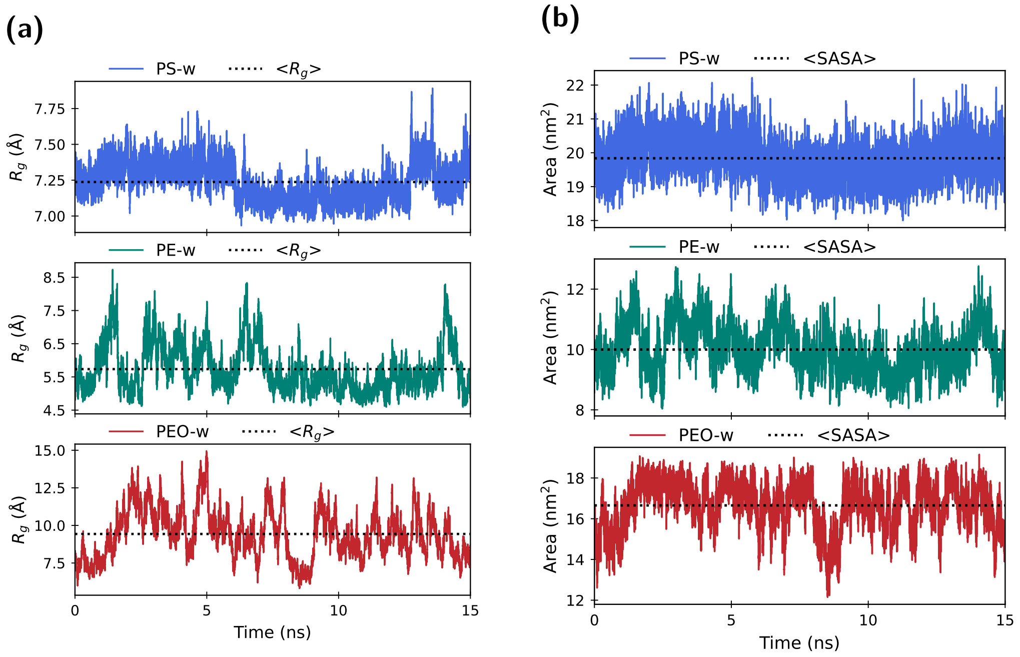

Figure 4.5: (a) The radius of gyration and (b) the corresponding SASA of the NPs-w models.

Figure 4.5 illustrates the fluctuation of R_g and SASA for the three polymer types in water boxes over the course of the simulations. Snapshots capturing the folded polymer chains in the NPs-w models at the end of the MD simulations are depicted in Figure 4.6. In principle, the hydrophilicity/hydrophobicity of a folded molecular structure correlates with its R_g (Hong and Lei, 2009). Hydrophilic polymers tend to adopt relatively unfolded structures in water, promoting interaction with the surrounding solvent, while hydrophobic polymers favor folded conformations to maximize self-interaction while minimizing contact with water. A preliminary analysis of Figure 4.5 reveals some key insights. Particularly, the relatively larger average R_g value for PEO (9.4 Å), compared to PS and PE (7.2 Å and 5.7 Å, respectively), indicates a less folded molecular structure, a characteristic consistent with its hydrophilic nature. Conversely, the smaller average R_g values for PS and PE are indicative of their hydrophobic character, driving them to adopt more folded conformations, hence, minimizing their interactions with water.

In a related study, Dettmann et al. employed coarse-grained MD simulations to explore the interaction of NPs with carbon nanotube in water (Dettmann et al., 2021). Investigating polymer chains similar to those studied here (i.e, comprising 20 units each) in bulk water, they reported R_g values for PEO, PE and PS of 9.3 Å, 6.3 Å and 7.3 Å. This demonstrates a noteworthy agreement with the findings of the current study.

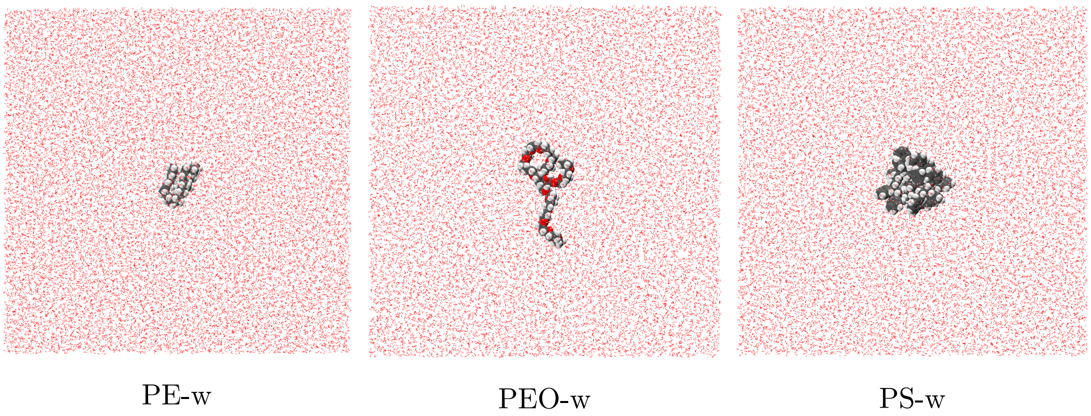

Figure 4.6: Snapshots of folded NPs in NPs-w models.

Moreover, the range of R_g for PEO (with RMSD value of 1.6 Å) is considerably wider than those of PE and PS (with RMSD values of 0.7 Å and 0.1 Å, respectively). This can be attributed to the hydrophilic nature of PEO and the hydrophobic nature of PE and PS. Another significant factor to consider is the volume occupied by each polymer type. The phenyl groups in PS increase the volume of its folded structure, thereby raising the average value of its R_g compared to PE. Moreover, the bulky nature of these phenyl groups results in steric constraint that limits the ability of PS to fold and unfold, resulting in a smaller range of R_g fluctuation than that of PE.

Furthermore, the plot of R_g for PS reveals distinguishable phases that last relatively longer than their counterparts in the case of both PE and PEO. This is also attributed to the larger volume occupied by the folded structure of PS due to its phenyl groups. Moreover, the SASA plots align with their corresponding R_g plots. However, it can be observed that, in contrast to R_g, the SASA values for PS are larger than that of PEO. This is also a result of its bulky nature due to its phenyl groups that have a larger surface area.

4.3.2 NPs on a mono-layer graphene

Understanding the dynamics of NPs in close proximity to graphene is crucial for developing graphene-based membranes for capturing NPs from aqueous environments. Here, the MD simulations of the NPs-1L models will be analyzed and discussed. The R_g of NPs in the NPs-1L models (displayed in Figure 4.7(a)) reveal that the hydrophobic polymers are relatively unfolded compared with their analogues in the absence of graphene. Namely, the average R_g value for each of PS and PE in the vicinity of graphene ($\approx$ 9.1 Å and 7.6 Å, respectively) is larger than its counterpart in the absence of graphene by about 1.9 Å. The reason is that the non-polar polymers prefer to interact with graphene. Therefore, they slightly unfold (compared to their peers in water) to maximize their contact with the surface of graphene.

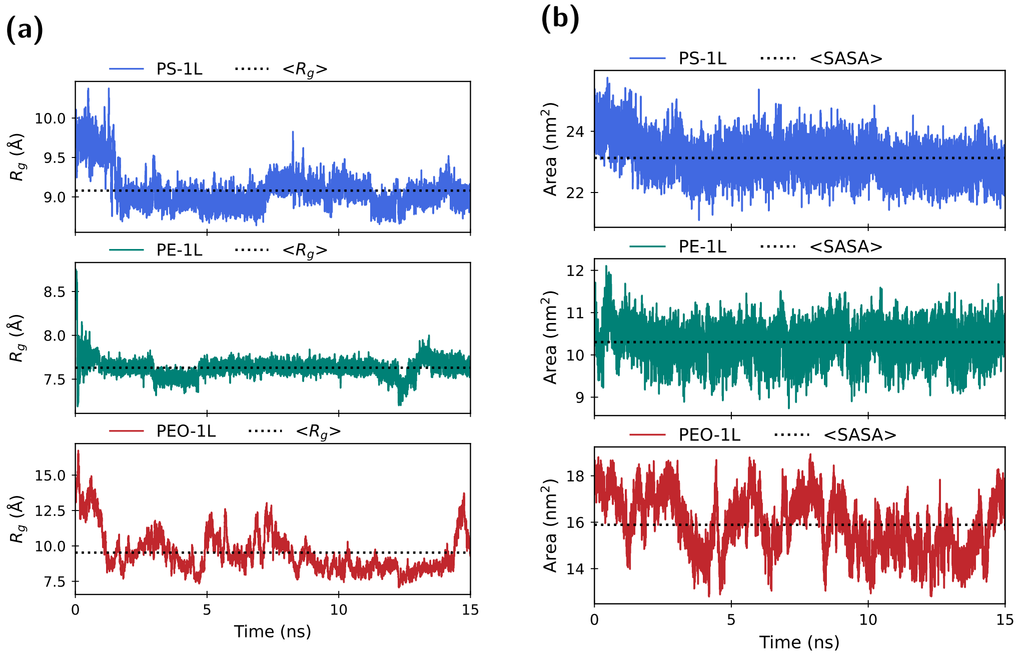

Figure 4.7: (a) The radius of gyration and (b) their corresponding SASA of the NPs-1L models.

Furthermore, from the R_g fluctuations of PS (as shown in the top panel of Figure 4.7(a)), one can notice a shift (of $\approx$ 1 Å) in the beginning of the trajectory. This indicates that, due to its bulky structure, PS needed longer time to fold compared to PE and PEO. For better understanding of the R_g fluctuations of PS in the vicinity of graphene, Figure 4.8 depicts snapshots that illustrate the dynamics of PS a long the MD simulation. On the other hand, comparing the R_g for PE-1L (given in Figure 4.7(a)) and PE-w (given in Figure 4.5(a)) with each other reveals that the presence of graphene not only affects the average value of R_g for PE but also significantly impacts the extent of its fluctuation. The narrower range of R_g fluctuation suggests that the polymer has attained a stable configuration, optimizing its self-interaction and enhancing its interaction with the graphene surface while minimizing its interaction with the surrounding water molecules (cf. Figure 4.9).

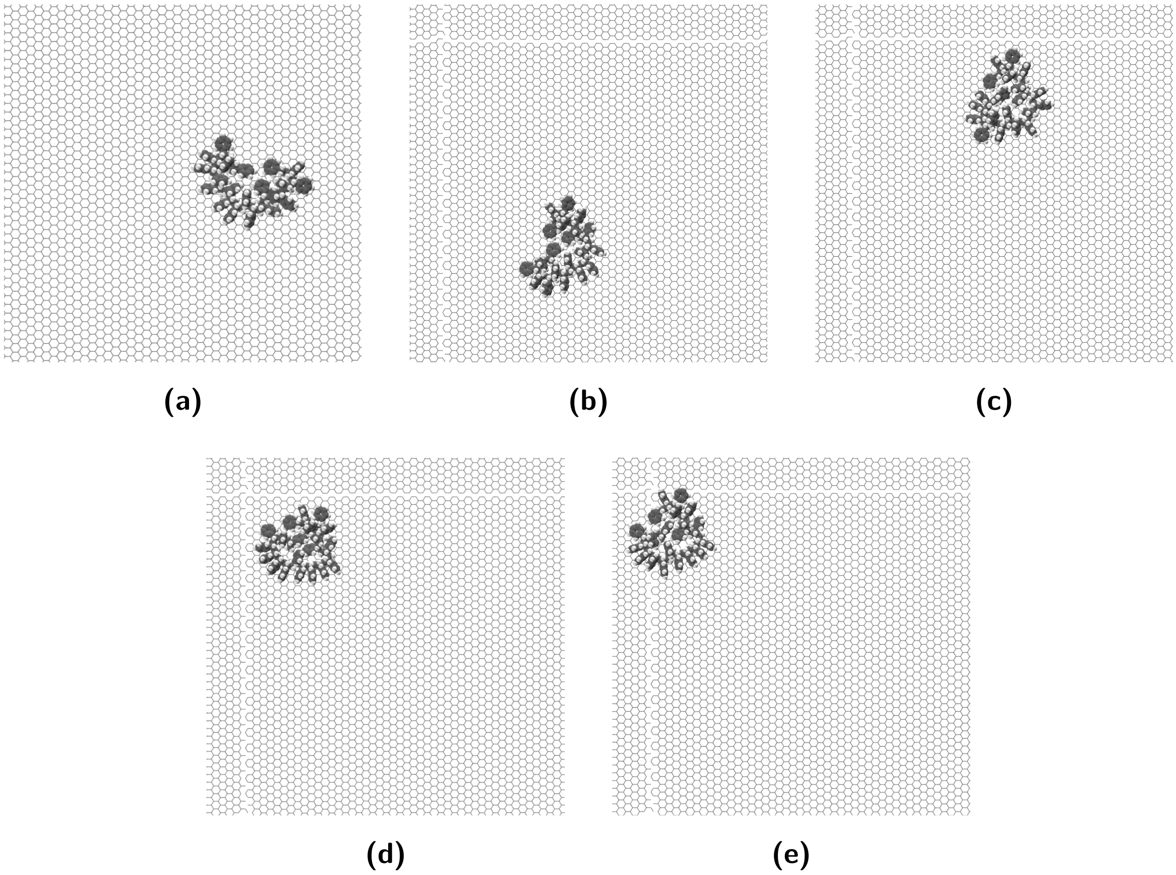

Figure 4.8: Snapshots from the the MD trajectory of PS-1L; (a) depicts the initial configuration post-equilibration, (e) captures the state at the end of simulation, while (b)-(d) showcase intermediate configurations. The water molecules are hidden for clearer visualization of the molecular structure of PS.

In contrast to the behavior observed in hydrophobic polymers, the analysis for PEO (as depicted in Figure 4.7(a)) reveals an interesting distinction. Compared to the case of PEO in bulk water, the presence of graphene does not impact neither the average value of R_g for PEO nor the range of its variability. This suggests that PEO, in the proximity of

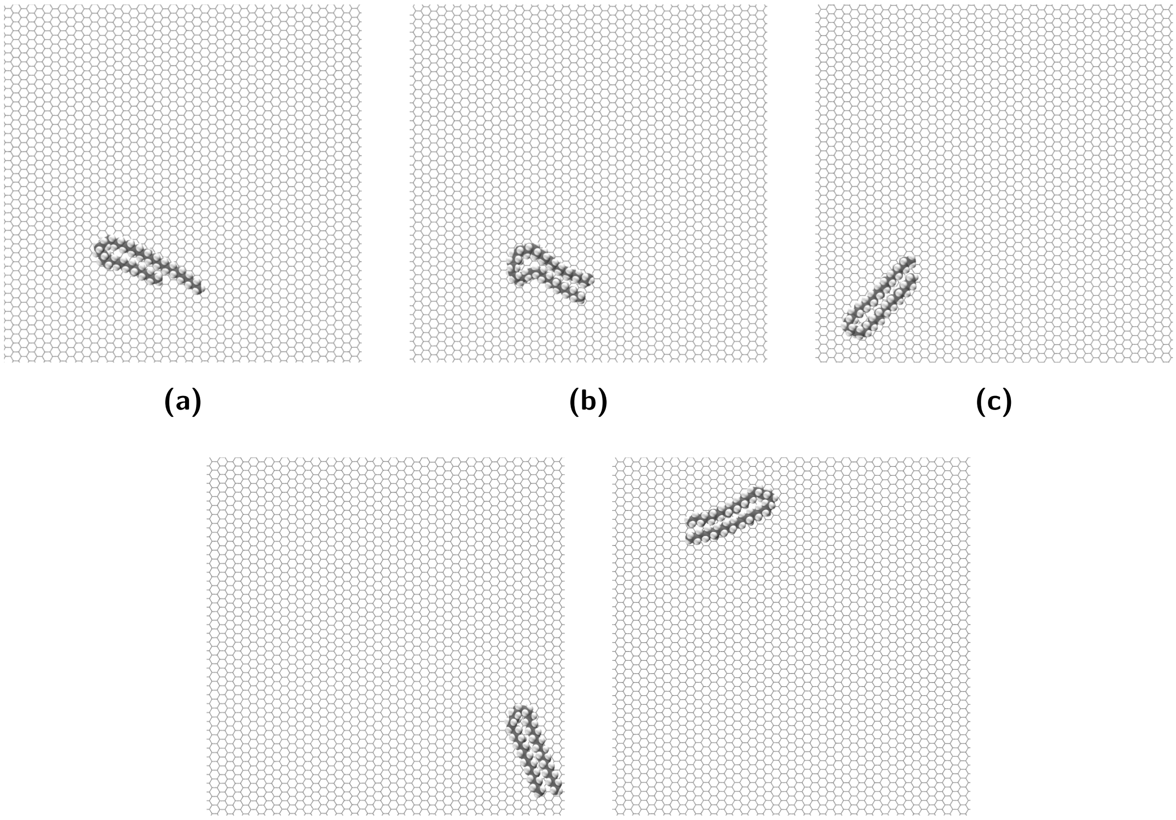

Figure 4.9: Snapshots from the the MD trajectory of PE-1L; (a) depicts the initial configuration post-equilibration, (e) captures the state at the end of simulation, while (b)-(d) showcase intermediate configurations. The water molecules are hidden for clearer visualization of the molecular structure of PE.

graphene, retains the ability to fold and unfold within a comparable range of R_g values, similar to its behavior in bulk water. However, it is clear that the rate or frequency of R_g fluctuations has undergone significant alteration. Figure 4.10 displays snapshots from the MD trajectory of PEO-1L showing the folding and unfolding behavior of PEO throughout the simulation.

Transitioning from the analysis of R_g, the SASA depicted in the companion subfigure (b) within Figure 4.7 is going to be discussed. The comparison of SASA results for the three NPs in bulk water (Figure 4.5) and their proximity to graphene (Figure 4.7) highlights interesting observation. Specifically, for PE and PEO, the range of SASA values exhibits a slightly narrower variation in the presence of graphene (8.7 nm^2 – 12.1 nm^2 for PE and 12.8 nm^2 – 18.9 nm^2 for PEO) compared to bulk water (8.0 nm^2 –

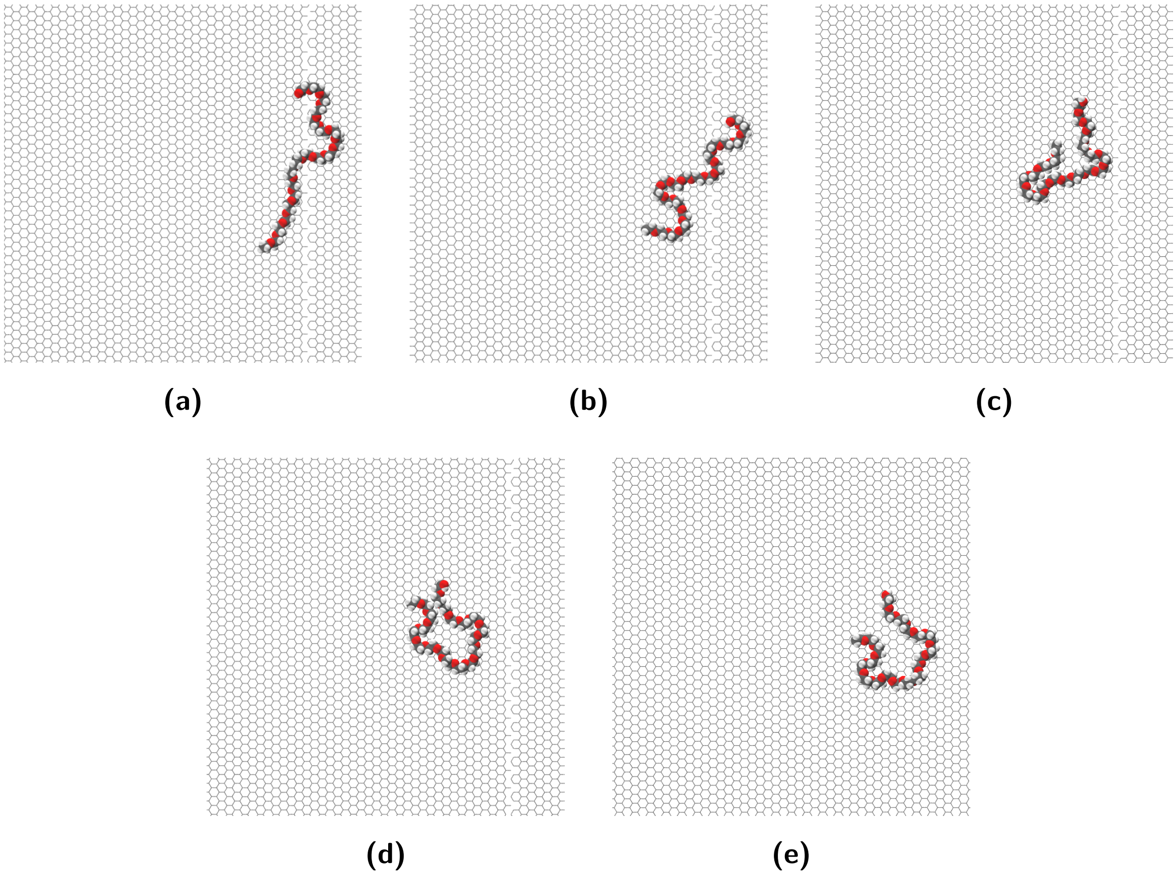

Figure 4.10: Snapshots from the the MD trajectory of PEO-1L; (a) depicts the initial configuration post-equilibration, (e) captures the state at the end of simulation, while (b)-(d) showcase intermediate configurations. The water molecules are hidden for clearer visualization of the molecular structure of PEO.

12.7 nm^2 for PE and 12.1 nm$^2 - 19.2$ nm^2 for PEO). Conversely, in the case of PS, the range of SASA fluctuation widens from 18.0 nm$^2 - 22.2$ nm^2 in bulk water to 21.1 nm$^2 -$ 25.8 nm^2 in the presence of graphene. These findings suggest that graphene enlarges the surface area exposed to the surroundings in PS, while marginally reducing it for PE and PEO.

Now shifting the focus from the influence of graphene on the R_g and SASA of the three polymer types, the analysis approaches the interaction between the NPs and graphene from a different perspective. Specifically, this will be explored through an examination of the partial densities of the polymers along individual axes, particularly along the z-axis (i.e., the axis perpendicular to the surface of graphene). This analysis unveils the vertical

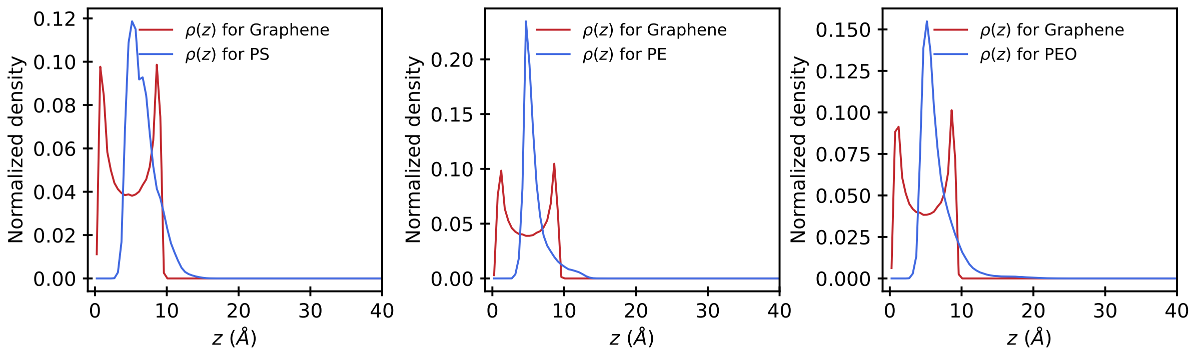

Figure 4.11: Partial mass densities along z-axis for NPs and graphene in the NPs-1L models. For better comparison, all partial densities were normalized according to Eq. 4.4.

distribution of the polymers and sheds light on their interaction with the graphene surface. Additionally, the discussion encompasses the partial density of graphene along the z-axis, contributing to a comprehensive understanding of the dynamics of both the NPs and graphene. The results of this analysis are displayed in Figure 4.11.

Remarkably, despite the NPs-1L models comprising only a single layer of graphene, the plots of the partial density of graphene along the z-axis exhibit, in all the cases, two distinct peaks. This occurrence reveals an interesting behavior wherein the planar surface of the graphene layer is deformed, fluctuating like a wave, with the plotted peaks indicating its crests and troughs. Notably, the presence of the polymer's peak in between the two peaks of the graphene partial density indicates a preference for the polymers to align within the valleys formed by the undulating graphene surface. This configuration is depicted in Figure 4.12.

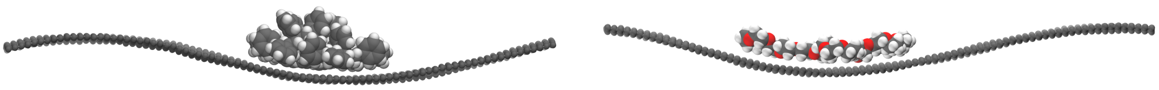

PS-1L

PEO-1L

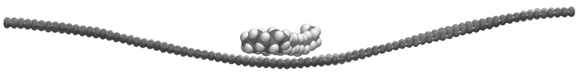

PE-1L

Figure 4.12: Snapshots of the NPs-1L models depicting the curved configuration of the graphene surface. Water molecules are omitted for better visualization.

A comprehensive analysis tracking the evolution of this configuration throughout the simulations is crucial to fully grasp the dynamics of the investigated polymers near graphene. This analysis can provide insights into the binding of the NPs to the graphene surface, preventing dispersion into the bulk water, and potentially influencing their diffusion mechanism in the xy plane (cf. Figure 4.13).

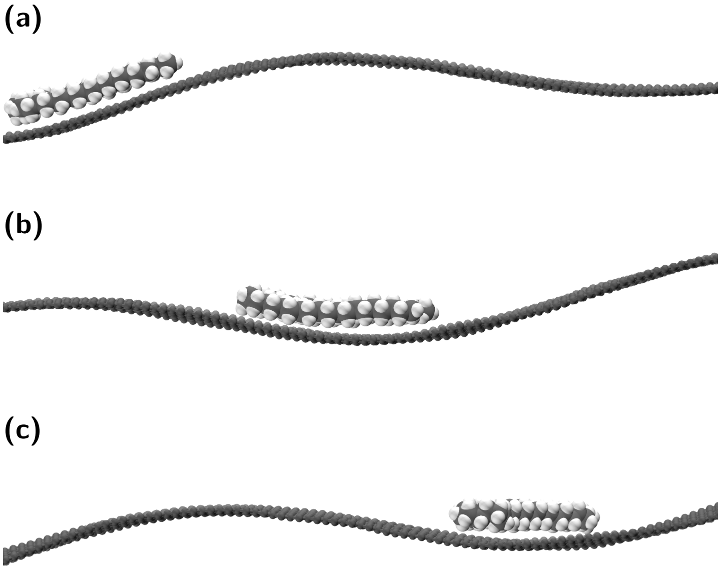

Figure 4.13: Snapshots of the NPs-1L models showcasing the diffusion of PE in the xy plane on the graphene surface, with configurations: (a) within the first 5 ns, (b) within the second 5 ns, and (c) within the last 5 ns. The water molecules are hidden for clearer visualization.

4.3.3 NPs confined between two graphene layers

While many of the computational studies that focus on the applications of graphene target mostly its perfect monolayer form (Cohen-Tanugi et al., 2016; Qin et al., 2010; Lim et al., 2011), the experimental production of such large-scale monolayers remains a significant challenge. On the other hand, the synthesis of multi-layer graphene-based membranes is considered more economically feasible than their single-layer counterparts. Nevertheless, modelling the multi-layer graphene-based membranes raises a question regarding the choice of the adequate number of layers. In this context, Cohen-Tanugi et al. (2016) suggest that transitioning from a single layer to two layers is deemed sufficient for comprehending most effects, with subsequent layers expected to have a qualitatively similar impact.

To this end, this section delves into an additional aspect of the topic, namely; examining the effects of confinement on the NPs in close proximity to graphene. To address this, molecular models were developed, involving NPs confined between two graphene layers with varying inter-layer spacings of 10 Å, 15 Å, and 20 Å (detailed in section 4.2.1.3). This exploration aims to investigate how such spatial constraints influence the dynamic behavior of the NPs in this particular arrangement. Noteworthy that the focus here is solely on the dynamics of NPs in these specific configurations, while the question about how NPs could be in such confined situations (which requires further simulations, e.g. free energy simulations) is beyond the scope of the current discussion. Moreover, the subsequent results will be discussed in comparison with the models containing only one graphene layer (as presented in section 4.3.2). Therefore, it is important to note that whenever the term "unconfined" is mentioned below, it pertains to the models including only one graphene layer (cf. section 4.3.2).

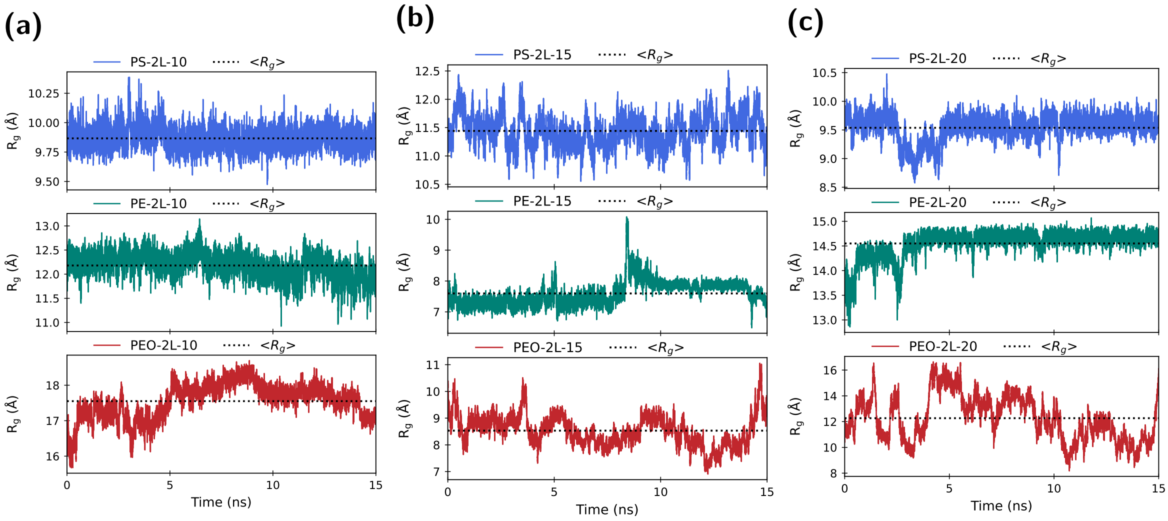

Figure 4.14: The R_g of NPs for (a) NPs-2L-10 models, (b) NPs-2L-15 models and (c) NPs-2L-20 models.

Figure 4.14 illustrates the calculated R_g of NPs confined between two graphene layers. Initial assessment of the plots in Figure 4.14 highlights distinct differences in the effect of confinement for each polymer type. For instance, the ultra-confinement (inter-layer distance of 10 Å) significantly unfolds PE and PEO structures, resulting in average R_g values of 12.2 Å and 17.6 Å, respectively, compared to 7.6 Å and 9.5 Å in their

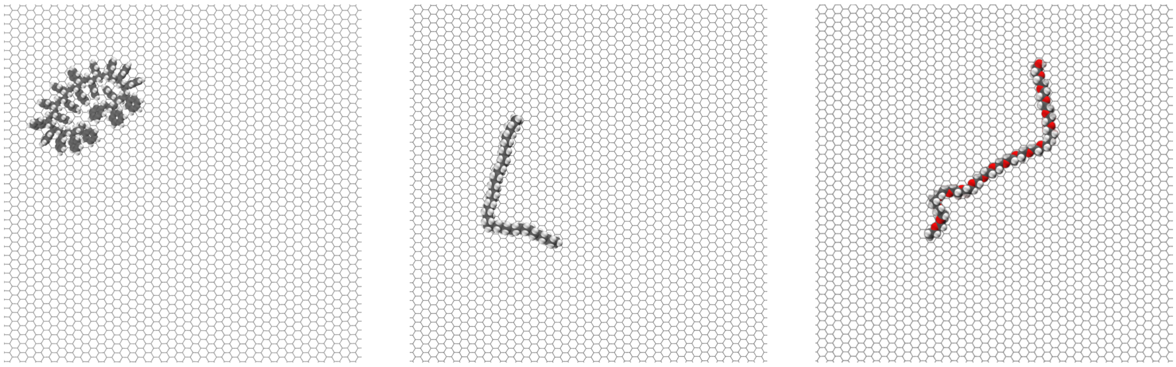

(a) PS-2L-10 **(b)** PE-2L-10 **(c)** PEO-2L-10

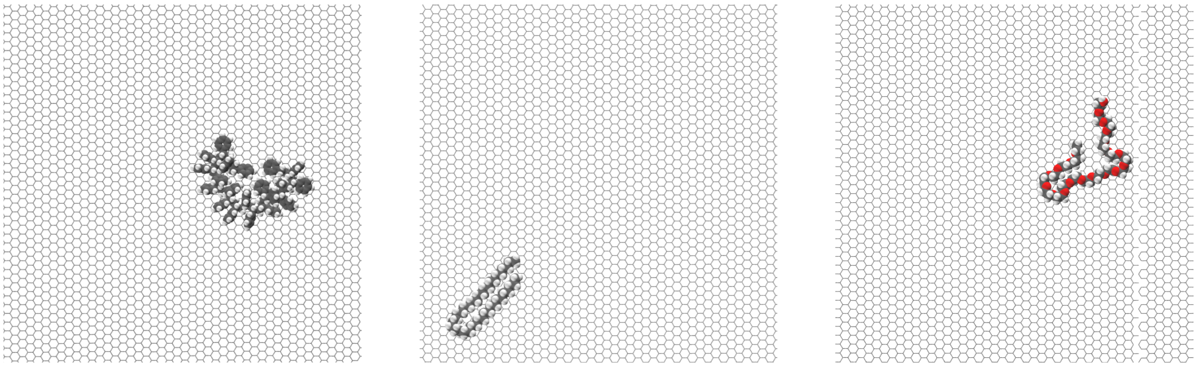

(d) PS-1L **(e)** PE-1L **(f)** PEO-1L

Figure 4.15: Snapshots depicting the NPs in the ultra-confined case (top) versus their folded unconfined analogues (bottom). In the case of NPs-2L-10 models, only one graphene sheet is shown (i.e., the upper graphene layer is hidden) for better visualization of the polymer chains.

unconfined analogues. Figure 4.15 depicts snapshots visualizing the relatively unfolded PE and PEO in the ultra-confined case (sub-figures (b) and (c), respectively) versus their folded unconfined analogues (sub-figures (e) and (f), respectively). In contrast, the impact of ultra-confinement on PS is relatively insignificant (cf. Figure 4.15), resulting in an average R_g value of 9.9 Å, only 0.8 Å larger than its unconfined counterpart.

The bulky molecular structure of PS plays a crucial role in its folding and unfolding dynamics. Despite being non-polar (i.e., would be expected to maximize its interaction with graphene), PS maintains a folded structure (cf. Figure 4.15, sub-figure (a) versus (d)) to increase self-interaction, creating spaces between the graphene layers at the spots where PS contact the graphene layer. In other words, as depicted in Figure 4.16, PS, occupying significant space, increases the distance between the graphene layers where it lies. Moreover, the short inter-layer distance (10 Å) allows graphene layers to approach each other, hence, interact strongly with each other. This configuration induces a wavy motion in the graphene layers, perturbed by the bulky folded PS structure. This structural arrangement challenges PS to unfold, necessitating it to overcome both self-interaction and inter-graphene interaction concurrently.

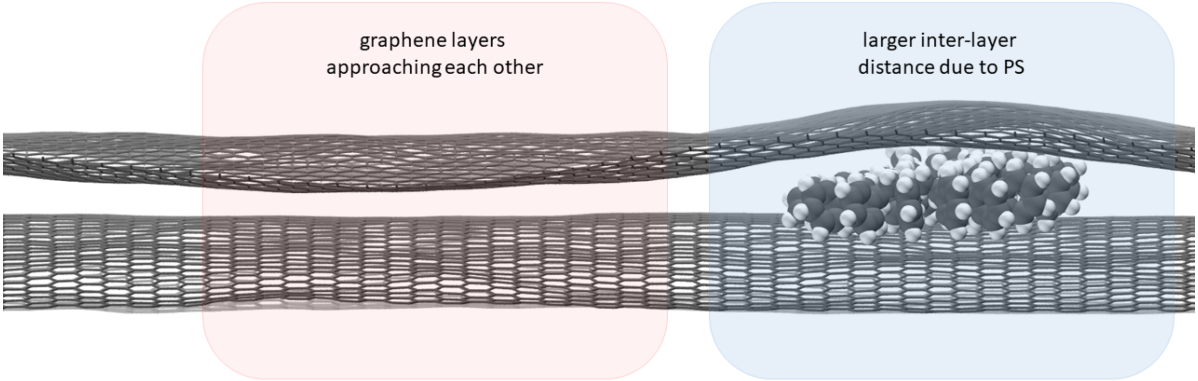

Figure 4.16: The perturbation of the graphene layers (at inter-layer distance of 10 Å) due to PS.

As the inter-layer spacing between the graphene layers increases, distinctive trends in R_g values for all polymer types emerge. Notably, at a 15 Å graphene inter-layer distance, PS demonstrates the largest average R_g value of 11.4 Å compared to its counterparts in all other investigated conditions. Conversely, PE and PEO exhibit less folded structures compared to their analogues in the 10 Å graphene inter-layer distance scenario. Specifically, the average R_g value for PE at a 15 Å graphene inter-layer distance is nearly identical to that in the vicinity of a single graphene layer. Intriguingly, PEO portrays its most folded structure among all the PEO molecular models, presenting an average R_g value of 8.5 Å.

Furthermore, at a 20 Å inter-layer distance between graphene layers, PS demonstrates behavior distinct from that of PE and PEO. In this scenario, the average R_g value for PS is remarkably similar to its counterpart in the 10 Å inter-layer distance case, albeit with a slightly wider range of fluctuation. This suggests that a 15 Å inter-layer distance could be the optimal value to achieve the most unfolded PS structure within an aqueous medium, offering a relatively higher degree of freedom for fluctuations. In contrast, the greater inter-layer spacing (20 Å) significantly unfolds the PE structure, resulting in the highest average R_g value for PE (14.6 Å). This expansion indicates PE's tendency to unfold and maximize its contact area and subsequent interaction with graphene, possibly favoring graphene interaction over self-interaction.

Table 4.1: Summary of R_g (Å) and their RMSD values for the three polymer chains in different environments. $<R_g>$ refers to the average R_g.

system	PS		PE		PEO	
	$<R_g>$	RMSD	$<R_g>$	RMSD	$<R_g>$	RMSD
in water	7.2	0.1	5.7	0.7	9.4	1.6
1L	9.1	0.2	7.6	0.1	9.5	1.5
2L-10	9.9	0.1	12.2	0.3	17.6	0.5
2L-15	11.4	0.3	7.6	0.4	8.5	0.6
2L-20	9.5	0.2	14.6	0.3	12.3	1.8

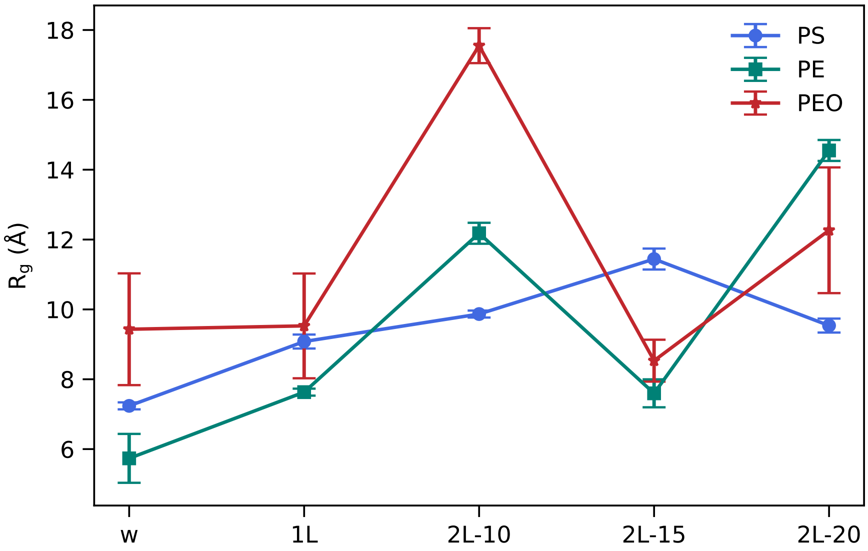

Figure 4.17: Summary of the average R_g value for the three polymer chains in different environments. The error bars represent the corresponding RMSD values given in Table 4.1

At a 20 Å inter-layer distance, PEO shows a relatively unfolded structure (average R_g = 12.3 Å) compared to the 15 Å distance case (average R_g = 8.5 Å). However, it does not exhibit as much unfolding as seen in the 10 Å inter-layer distance case.

For a comprehensive overview of the impact of different environmental conditions and spatial arrangements on the NPs, Table 4.1 presents the numerical values of average R_g and the corresponding RMSD values, showcasing the range of fluctuation in each scenario. Additionally, Figure 4.17 illustrates plots depicting the data given in Table 4.1, showcasing the folding and unfolding dynamics of each polymer type in response to various conditions.

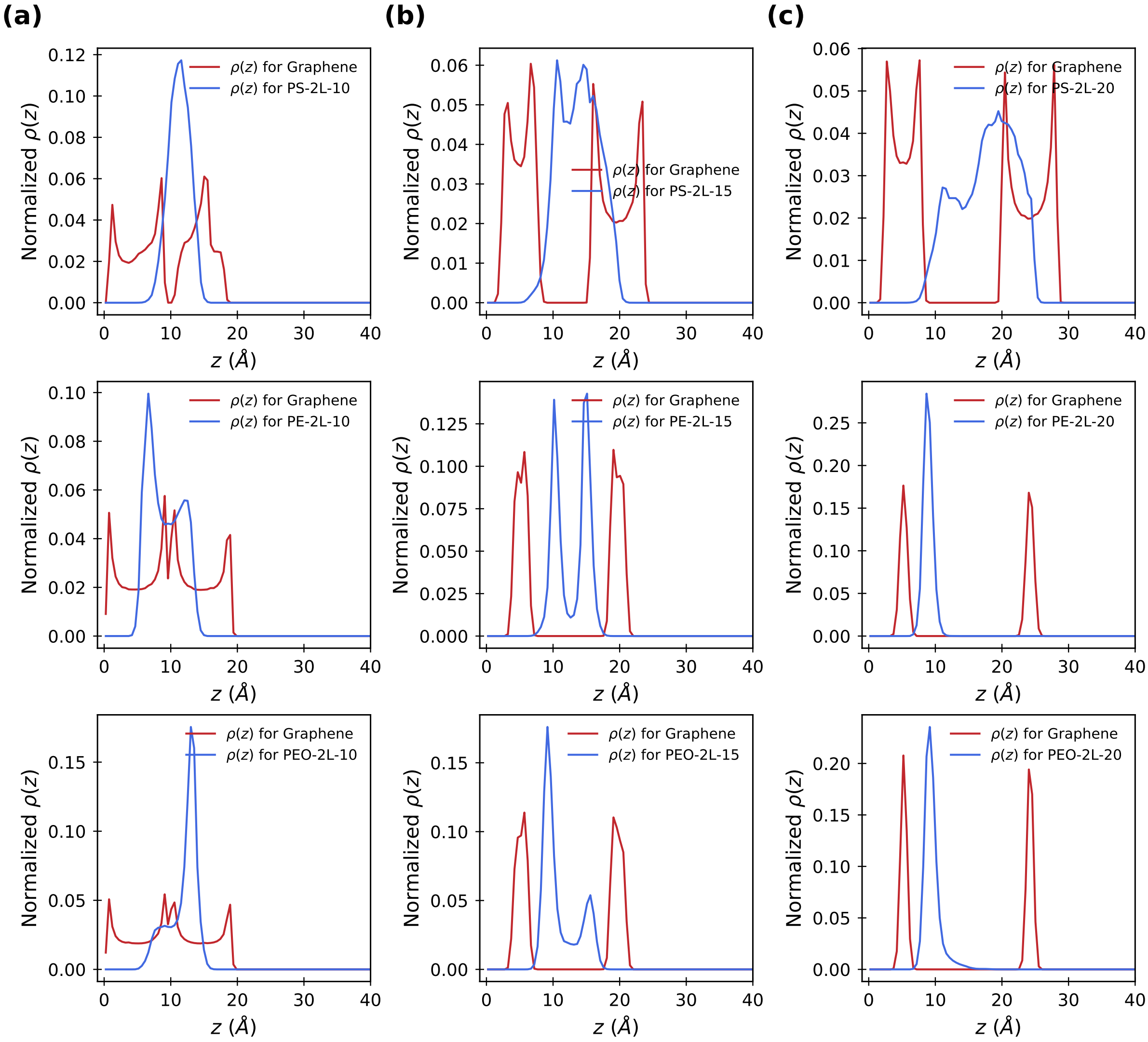

Figure 4.18: The partial densities along z-axis ($\rho(z)$) for the polymers and graphene in (a) NPs-2L-10 models, (b) NPs-2L-15 models and (c) NPs-2L-20 models.

Upon analyzing the results of the partial densities for the NPs-2L-d models along the z-axis ($\rho(z)$) presented in Figure 4.18, interesting observations emerge. Namely,

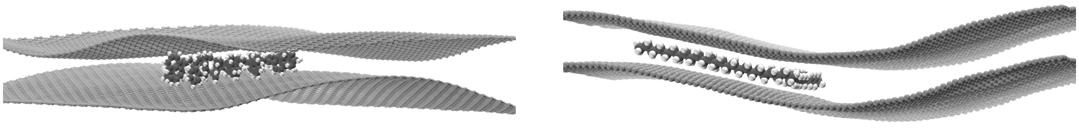

(a) PS-2L-10 **(b)** PE-2L-10

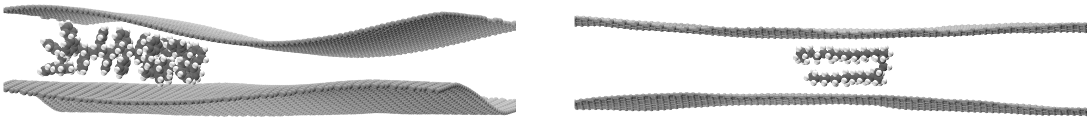

(c) PS-2L-15 **(d)** PE-2L-15

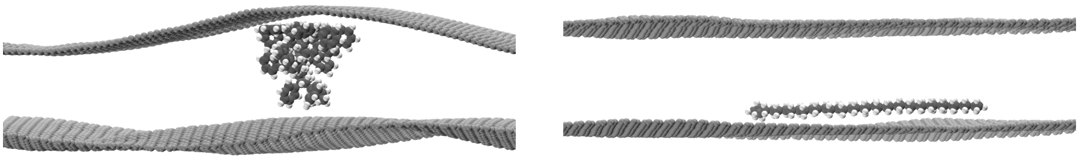

(e) PS-2L-20 **(f)** PE-2L-20

Figure 4.19: Snapshots depicting the dynamical behavior of the graphene layers in the NPs-2L-d models.

the $\rho(z)$ plots revealed that the variation in inter-layer spacing between the graphene layers not only influences the dynamics of the polymers but also significantly impacts the dynamical behavior of the graphene layers themselves (cf. Figure 4.19). The $\rho(z)$ plots provide a visual representation of this distinct behavior, shedding light on how the altered spatial arrangement affects the distribution and interaction patterns within the system.

Overall, these results indicate that within the models involving PS, regardless of the various inter-layer distances, each graphene layer displays a reminiscent undulating motion akin to what was observed in the single graphene layer case, as previously discussed. This distinctive behavior is evident in the top row of plots in Figure 4.18, indicating the presence of two peaks for each graphene layer. On the other hand, within the PE and PEO models, the distinct undulating movement of the graphene layers was specifically noted in the models featuring the shortest inter-layer distance (10 Å). In contrast, as the inter-layer distance is expanded to 15 Å and 20 Å (for models involving PE or PEO), a remarkable reduction in the dynamic behavior of the graphene layers is evident. Instead of the previous distinctive undulating motions, the graphene layers portray a more vibrational movement. This transition is observed through the presence of relatively narrow peaks for each layer.

Exploring the influence of adjusting the inter-layer distance on polymer behavior reveals distinctive patterns. For example, in the PS-2L-10 model, a peak for $\rho(z)$ of PS appears positioned midway between the peaks of the graphene layers. Increasing the inter-layer distance to 15 Å results in the emergence of two peaks for $\rho(z)$ of PS. Further extension to 20 Å broadens these two peaks. In contrast, PE and PEO exhibit different responses to changes in the inter-layer spacing, notably at the largest inter-layer distance (20 Å). Each polymer type shows a single peak for $\rho(z)$ situated near the peak of a single graphene layer. These observations suggest that the relatively unfolded structures of PE and PEO tend to maximize contact with only one graphene layer under such extensive inter-layer distances, resembling the behavior seen in a single graphene layer.

4.3.4 NPs-graphene interaction energies

In the subsequent analysis, polymer-graphene interaction energies (E_{int}) are calculated and examined. Figure 4.20 displays the E_{int} plots for models featuring polymers confined between two graphene layers. For comparison, E_{int} plots involving a single graphene layer are also presented in Figure 4.20. It is important to note that direct numerical comparison of E_{int} values between different polymers is not feasible. However, these plots offer a qualitative comparison, providing insights into the diverse impacts of similar confinement conditions on different polymer types.

Upon examining all the E_{int} plots, it is apparent that the strongest interaction between all polymer types and graphene occurs at the shortest inter-layer distance (i.e., 10 Å, as depicted in Figure 4.20(b)). This proximity between the polymers and both graphene layers naturally leads to intensified interactions. A comparison between subfigures (a) and (b) in Figure 4.20 emphasizes this point. The polymer-graphene E_{int} values for all polymer types with a 10 Å inter-layer distance are approximately twice their single graphene layer counterparts.

On contrary, the results displayed in Figure 4.20(c) indicate that at a 15 Å inter-layer distance, the polymer-graphene interaction is notably weaker for all polymer types. This may be attributed to a competitive effect between the two graphene layers (i.e., the two layers compete for adsorbing the polymer), resulting in an overall reduced polymer-graphene interaction. Notably, at a 20 Å inter-layer distance, the average E_{int} values closely resemble those observed in the single graphene layer models to a considerable extent.

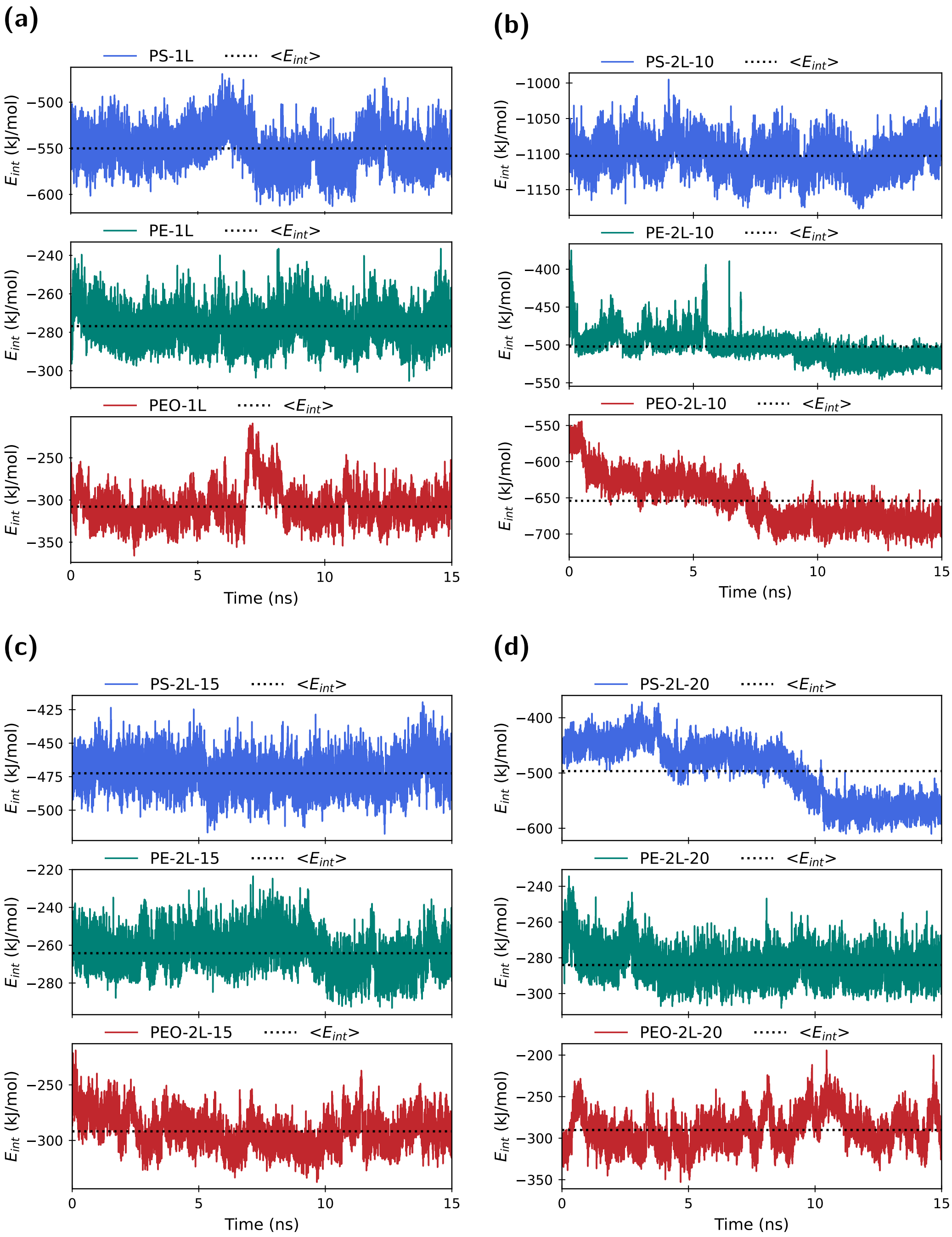

Figure 4.20: The NPs-graphene interaction energies (E_{int}) for (a) NPs-1L models, (b) NPs-2L-10 models, (c) NPs-2L-15 models and (d) NPs-2L-20 models during the production run (i.e., 15 ns of NVT simulations).

Furthermore, while the majority of the E_{int} plots demonstrating typical fluctuations, there are notable deviations in two particular cases, which exhibit a shift in the range of fluctuation:

1. PEO-2L-10: PEO between two graphene layers at a 15 Å inter-layer distance, illustrated in the middle panel of Figure 4.20(b).
2. PS-2L-20: PS between two graphene layers at a 20 Å inter-layer distance, depicted in the top panel of Figure 4.20(d).

The distinct changes in these cases reveal interesting dynamics. In the case of PEO-2L-10, the observed transition in polymer-graphene interaction aligns with a notable shift towards a more unfolded PEO structure, as evidenced in the corresponding R_g plot (Figure 4.14(a)). This structural change in PEO appears to drive an intensified interaction with graphene due to increased contact areas, resulting in a stronger binding. Conversely, for PS-2L-20, the significant change in the E_{int} plot (Figure 4.20(d)) does not correlate with the fluctuation behaviour observed in the R_g plot (Figure 4.14(c)). Examination of the MD trajectory provides insight into this observation. The alteration in PS-2L-20's polymer-graphene interaction results from its distinct orientations between the graphene layers (cf. Figure 4.21). Despite maintaining its folded structure, PS slightly reoriented to optimize contact with one graphene layer, probably albeit at the expense of reduced contact with the other. However, this change enhanced the overall PS-graphene contact area and, consequently, their interaction.

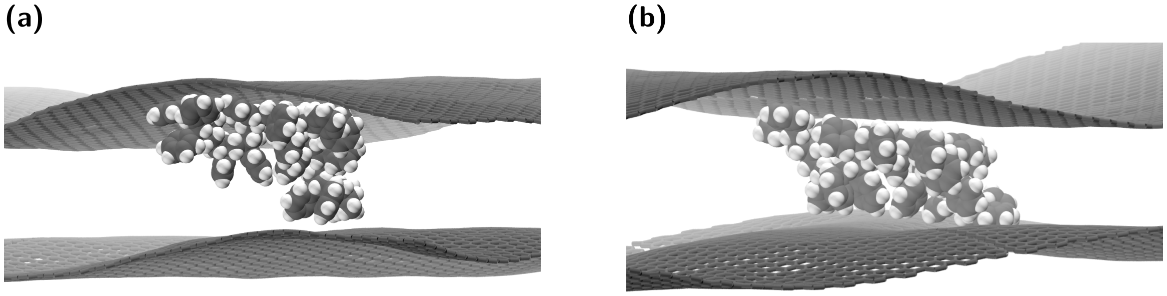

Figure 4.21: Snapshots of the the two distinct orientations of PS in the PS-2L-20 model.

To comprehensively understand the strength trends in NPs-graphene interactions, the E_{int} (cf. Figure 4.22) for the NPs in different scenarios were calculated using the formula:

$$E_{\text{int}} = 1 - \frac{E_{\text{graphene+sol}}}{E_{\text{sol}}} \tag{4.5}$$

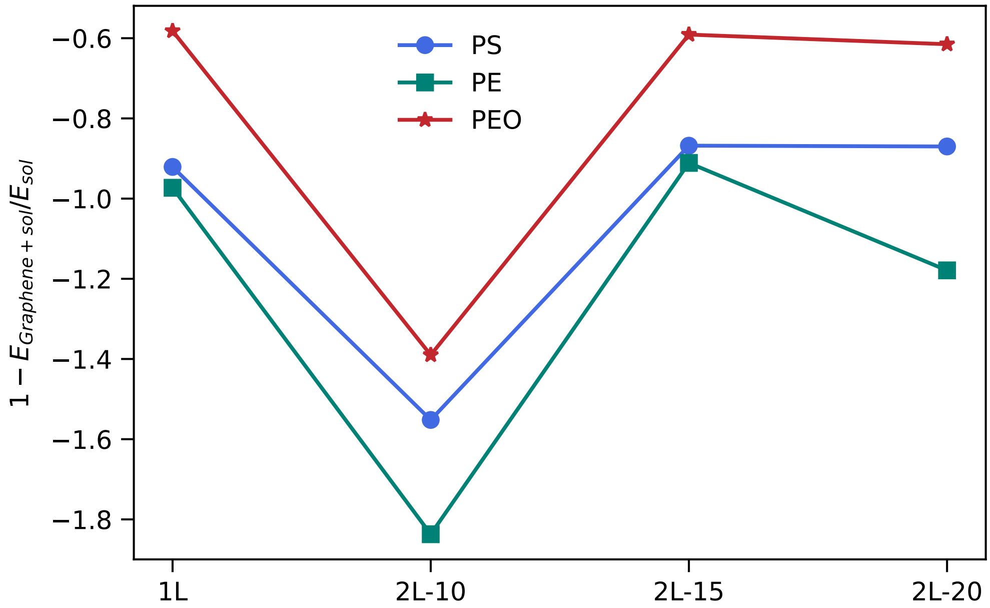

Figure 4.22: Summary of the NPs-graphene interaction energies (i.e., relative E_{int}).

Here, $E_{\text{graphene+sol}}$ represents the interaction energy between the polymer and the system near graphene, while E_{sol} is the interaction energy between the polymer and the system in bulk water. Hence, E_{int} represents the stability of NPs-1L and NPs-2L-n relative to each other. A more negative E_{int} value indicates a more stable configuration. Remarkably, all cases yielded negative relative E_{int} values, implying that graphene likely has the capacity to adsorb all the investigated NPs, regardless of polymer type. Nevertheless, PE consistently exhibits the strongest interaction with graphene, followed by PS and PEO. Despite the ultra-confinement in the case of two graphene layers with a 10 Å inter-layer distance, all polymers seem to prefer this configuration.

In contrast to these findings, Dettmann et al. (2021) reported that PEO could not be adsorbed inside or at the outer wall of a carbon nanotube. Additionally, comparing the relative E_{int} values for PS on graphene with those on a carbon nanotube in the above-mentioned study suggests that graphene may possess a stronger capability to adsorb PS than the carbon nanotube. It is crucial to note that the disparities in the performance of graphene, as investigated in the current study, and the carbon nanotube, as reported by Dettmann et al. (2021), regarding their interactions with PEO and PS, may be attributed to the differing levels of theoretical approaches employed in both studies (atomistic force field versus coarse-grained). Consequently, a comprehensive evaluation of these methods may be required to validate the comparison between graphene and carbon nanotube interactions as presented in this discussion.

4.3.5 Adsorption of NPs on rigid graphene

As mentioned earlier, in all the NPs-1L models, the graphene layer exhibits a curvature and all the NPs were adsorbed in the valley formed due to the wavy motion of graphene. To investigate the potential impact of graphene curvature on polymer trapping, a specific case, the PEO-1L model, underwent an additional MD simulation with constraints applied to graphene. These constraints aimed to maintain the complete rigidity of graphene by preventing any curvature throughout the simulation, and this specific simulation will be referred to as PEO-1L-fix. The selection of PEO was motivated by its unexpected behavior compared to typical hydrophilic polymers. Despite being hydrophilic, the PEO polymer, as indicated by its $\rho(z)$ results (see Figure 4.11), displayed behavior similar to hydrophobic polymers, remaining in close proximity to the graphene surface without dispersing into the surrounding water during the simulation.

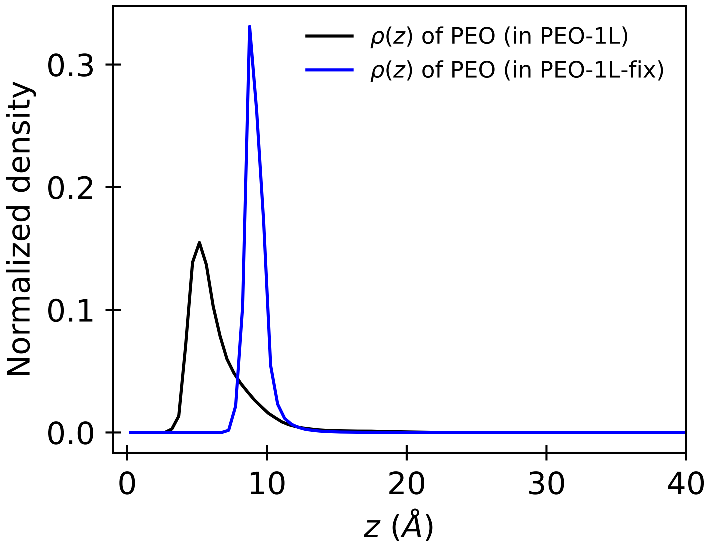

Figure 4.23: $\rho(z)$ for PEO in the PEO-1L-fix model. Its counterpart in the PEO-1L model is also displayed for comparsion.

Figure 4.23 presents the partial densities results for PEO-1L-fix. Interestingly, the $\rho(z)$ results of PEO-1L-fix indicate that, akin to the behavior observed in the PEO-1L model with no constraints applied to graphene, PEO adheres to the non-deformed graphene surface throughout the simulation, without dispersing into the surrounding water. This observation suggests that the curvature of graphene may not be the primary factor influencing NPs adsorption.

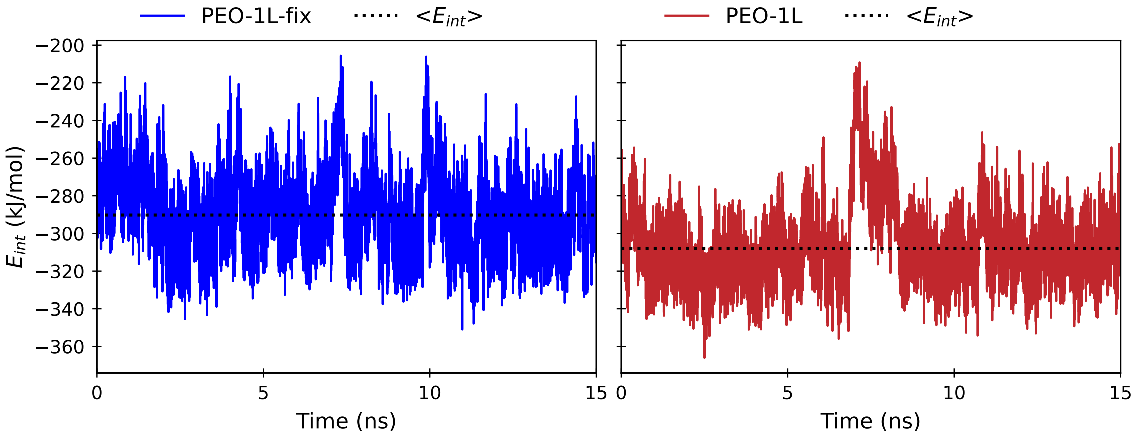

Figure 4.24: PEO-graphene interaction energies (E_{int}) under two conditions: (left) graphene held fixed during the simulation and (right) graphene without any constraints applied.

To assess the impact of graphene curvature on the binding between PEO and graphene in both cases, the Lennard–Jones PEO-graphene interaction energies (E_{int}) were calculated and are depicted in Figure 4.24. The average E_{int} value for PEO-1L of -307.9 kJ/mol compared with -290.2 kJ/mol for PEO-1L-fix reveal that the curvature of graphene slightly enhance its binding with PEO.

Finally, Figure 4.25 displays the R_g and SASA results for PEO-1L-fix compared with their analogues of PEO-1L. The average R_g and SASA values for PEO-1L-fix (11.4 Å and 16.5 nm^2, respectively) reveal that the deformed graphene yields a more folded PEO structure (with average R_g and SASA values of 9.5 Å and 15.9 nm^2, respectively). Additionally, the examination of R_g fluctuations in PEO-1L-fix compared to PEO-1L suggests that the graphene surface curvature contributes to a slower rate of folding and unfolding for PEO.

4.4 Summary

The present chapter explored monolayer and bilayer models of bare graphene as probably the most simple representations of graphene-based membranes. The objective is to gain

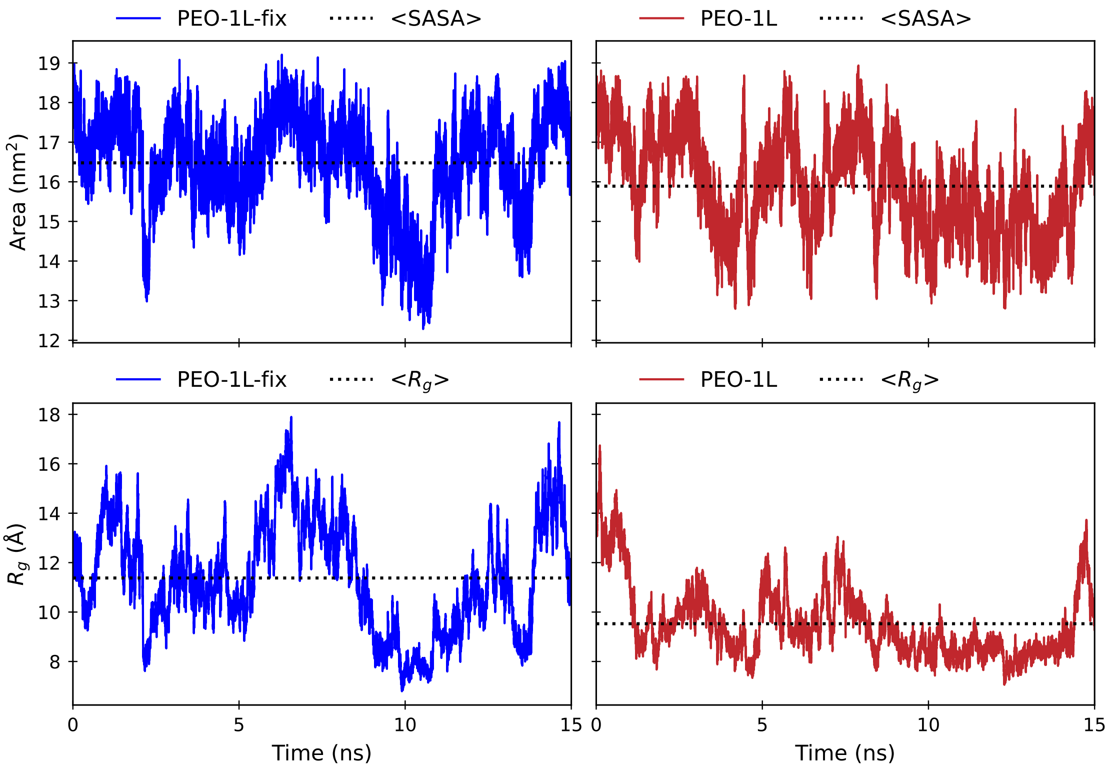

Figure 4.25: R_g and SASA results for PEO under two conditions: (left) graphene held fixed during the simulation and (right) graphene without any constraints applied.

insights into their interactions with hydrophobic and hydrophilic polymer chains, specifically polyethylene (PE), polyethylene oxide (PEO), and polystyrene (PS), which serve as representative models for nanoplastics (NPs). Atomistic force field-based molecular dynamics (MD) simulations were employed to investigate the dynamics of these NPs in distinct environmental contexts: bulk water, in proximity to a single layer of graphene, and confined between two graphene layers with varying inter-layer spacing.

The analysis of results focused on parameters such as radius of gyration (R_g), solvent-accessible surface area, polymer-graphene interaction energies, and partial densities of the polymers (and graphene) along the z-axis. This comprehensive analysis provided valuable insights into how each polymer type responds to different surroundings. Notably, PS exhibited a more compact structure in bulk water, contrasting with its most unfolded form when confined between two graphene layers at a 15 Å inter-layer distance. PEO, being a polar polymer, displayed the most compact structure at a 15 Å inter-layer distance, while adopting a more unfolded conformation at 10 Å inter-layer distance.

Hydrophobic PE showcased a compact structure in bulk water and an unfolded form between two graphene layers at a 10 Å inter-layer distance.

The analysis of partial densities along the z-axis and polymer-graphene interaction energies near a single graphene layer revealed graphene's potential to effectively capture all investigated polymers. Surprisingly, even PEO did not dissolve into water after extended MD simulations, indicating graphene's ability to retain both non-polar and polar polymers in a confined space. This observation holds promise for applications in the removal of NPs from aqueous environments. Comparisons with a recent study focusing on the interactions between NPs and carbon nanotubes, utilizing coarse-grained MD simulations, revealed consistent dynamical behaviors of the investigated NPs in bulk water. Additionally, in terms of the capability to adsorb NPs, graphene demonstrated superior performance over carbon nanotubes in adsorbing both PS and PEO, while both materials exhibited similar performances in the case of PE.

In conclusion, the findings of this study shed light on the intricate dynamics of NPs interactions with graphene in various environments. While the current work did not consider entropy, it is imperative to acknowledge its potential significance in future studies.The observed capability of graphene to effectively capture both hydrophobic and hydrophilic polymers, even under confined conditions, opens avenues for further exploration. Future investigations could delve into the diffusion of NPs in water and in close proximity to graphene, unraveling the impact of confinement on NP diffusion dynamics. Additionally, although the current results indicated that NPs could be adsorbed on graphene (based on molecular models with NPs positioned close to graphene), further free energy simulations would improve our understanding of how such process occur considering initial molecular models in which NPs are placed in bulk water (i.e., a way from graphene). The free energy simulations may also help in revealing how feasible it is to inject NPs between graphene layers considering initial molecular models where NPs are outside the bi-layer system. Furthermore, another interesting avenue lies in exploring the effect of graphene functionalization, such as graphene oxide, on its ability to adsorb NPs. Understanding whether functional groups induce trapping effects on specific spots of the graphene surface could provide valuable insights into tailoring graphene-based membranes for enhanced NPs capture and removal. These future directions should aim to refine our understanding of the complex interplay between graphene and NPs, advancing the development of efficient strategies for environmental remediation and sustainable water treatment technologies.

5 Adsorption of Dioxin on 2D Antimonene

5.1 Motivation

The toxicity of organic pollutants is a common environmental problem that received much attention and worries from the scientific community and the broader public. Among these toxic organic pollutants are dioxins (Ganji et al., 2015; Fernandez-Gonzalez et al., 2015), e.g., polychlorinated dibenzodioxins (PCDD) and polychlorinated dibenzofurans (PCDF). They can be easily produced from plenty of sources including waste incineration, cigarette smoke, car exhaust, and natural combustion processes (Yive and Tiroumalechetty, 2008; Kulkarni et al., 2008; Mizukami, 2005). Their chemical stability allows them to be easily absorbed by fatty tissues and stored for about 11 years, thus poisoning humans and animals.

Especially, 2,3,7,8-tetrachlorodibenzo-p-dioxin (TCDD, see Figure 5.1) is considered one of the most hazardous dioxins and it has been classified by the International Agency for Research on Cancer (IARC) as a carcinogen for humans (Yang et al., 1999). Many studies have aimed to contribute to the solution of this problem through the degradation of dioxins by various chemical and physical processes including photocatalysis (Choi et al., 2000; Samara et al., 2020; Choi et al., 2004), hydrothermal degradation (Jin et al., 2013), burning (Hung et al., 2013), catalytic degradation (Ukisu and Miyadera, 2002), radiolysis (Zhao et al., 2007; Hilarides et al., 1996), electrochemical oxidation (Vallejo et al., 2013; Palanisami et al., 2015), and biodegradation (Saibu et al., 2020).

Recently, the peculiar properties of two-dimensional (2D) materials, as well as the great potential that they have shown to contribute to the solution of several problems, including environmental ones (Qin et al., 2021; Di et al., 2018), have attracted the attention of researchers from several disciplines (e.g., condensed matter physics, material science, chemical engineering, and nanotechnology) (Tan et al., 2017; Yu et al., 2017).

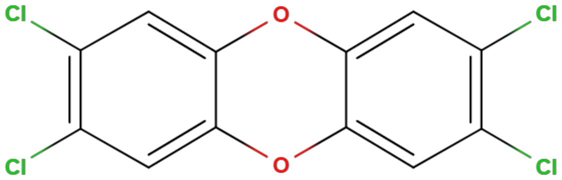

Figure 5.1: Schematic chemical structure of TCDD.

The successful preparation of one-atom-thick graphene sheets by (Novoselov et al., 2004) triggered the discovery and the investigation of other 2D materials with remarkable properties such as aluminene (Yeoh et al., 2018), silicene (Galashev and Vorob'ev, 2021; Le Lay et al., 2009), germanene (Bianco et al., 2013), phosphorene (Baghsiyahi and Yeganeh, 2020; Wu et al., 2020), and antimonene (Wang et al., 2021b).

Several studies investigated the ability of various 2D and other materials to capture and remove TCDD. For instance, (Ganji et al., 2015) studied the interaction of TCDD with carbon nanotubes (CNTs) and boron nitride nanotubes (BNNTs). They found that the adsorption energy of TCDD on the BNNTs is higher than CNTs and the adsorption capability of pristine BNNTs is better than that of defected ones. Moreover, Fagan et al. investigated the interaction between TCDD and CNTs and reported that it is enhanced by defects of CNTs. Pan et al. explored the absorption of TCDD using the 1-butyl-3-methylimidazolium dicyanamide ionic liquid. Their results showed that the interaction of TCDD with the anion of the ionic liquid is two times stronger than that of the cation. They also reported that inclusion complexes (i.e., TCDD with β-cyclodextrin (Pan et al., 2011)) can be formed in both gas and solution phases, suggesting that β-cyclodextrin might serve as a possible substrate-enhancing TCDD capture. Zhang et al. studied the interaction of metal-doped graphene with TCDD molecules and the results revealed that Ti-doped graphene enhances the capability for TCDD capture. Similarly, Kang examined the binding of TCDD with metal-doped graphene and CNTs and found that Fe-doped CNT strongly binds with TCDD. Additionally, pristine and doped phosphorene have been proposed as promising materials for adsorbing TCDD molecules by (Zhang et al., 2017). They reported that doping phosphorene by Ca improved the adsorption of TCDD on the phosphorene surface.

Recently, antimonene-based materials have shown unique physical properties that place them among the promising materials to be utilized in many applications such as energy storage (Tian et al., 2018; Liu et al., 2015; Li et al., 2015; Gu et al., 2017), gas sensors (V. Nagarajan, 2019; Srivastava et al., 2020), and spintronics (Yang et al., 2016). So far, however, the potential for the application of antimonene to capture organic pollutants such as TCDD has not been explored. Therefore, in this study, the interaction of pristine and (Ca-, Ti- and Ni-) doped 2D antimonene with TCDD has been investigated using the density functional theory (DFT) to explore the potential of these materials to bind and eventually remove this highly toxic compound.

5.2 Computational Models and Methods

5.2.1 Molecular Models

The TCDD molecule has an aromatic planar structure (cf. Figure 5.1), while antimonene has a buckled geometry. First, the isolated structure of TCDD has been optimized and analyzed based on selected structural parameters. Given in Table 5.1 are the values of these selected parameters calculated at the DFT level of theory (see detail below), together with the corresponding experimental values reported by Boer et al. (1972).

Table 5.1: DFT-calculated structural parameters (namely, C-O, C-C , and C-Cl bonds, and C-O-C angle) of TCDD versus their experimental counterparts.

Method	Structural parameters			
	C-O (Å)	C-C (Å)	C-Cl (Å)	C-O-C (°)
DFT	1.38	1.40	1.73	115.98
Experiment	1.37	1.36	1.73	115.70

To construct the antimonene crystal model, the lattice and geometrical criteria of the antimonene primitive unit cell calculated by Bafekry et al. (2019) has been utilized. In principle, the antimonene primitive unit cell consists of two Sb atoms in buckled form with two intersecting atomic planes. The values of the structural parameters that fully describe the mono-layer antimonene unit cell, i.e., lattice constant, Sb-Sb bond length, Sb-Sb-Sb angle, and the height of the two atomic planes of antimonene, are 4.12 Å, 2.95 Å, 88° and 1.75 Å, respectively. Using this primitive unit cell, a 5×5×1 supercell was built . Following, three doped-antimonene (namely, doped with Ni, Ca or Ti) supercells were created by replacing one Sb atom with the dopant atom.

Contaminating antimonene by inserting a dopant atom is expected to induce some distortion around the dopant atom. Therefore, prior to studying the adsorption of

TCDD on the surfaces of antimonene and doped-antimonene, cell relaxation calculations for all the created supercells were performed to insure that a minimum energy lattice structure for each case before adsorbing TCDD has been obtained. Figure 5.2 displays the optimized molecular structures of isolated TCDD and the antimonene supercells. In addition, the values of their lattice and geometrical parameters are given in Table 5.2. The computational details (e.g., level of theory and software used) are given below (section 5.2.2).

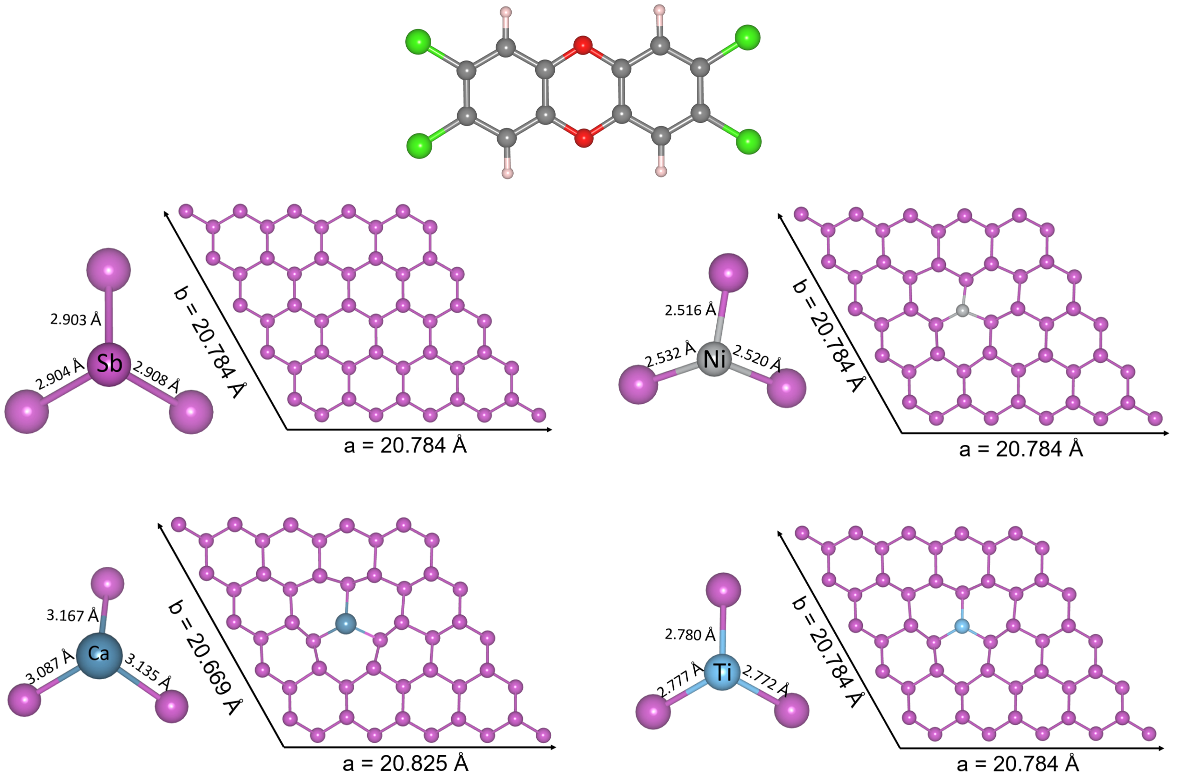
2.903 Å
2.904 Å
Sb
2.908 Å
b = 20.784 Å
a = 20.784 Å
2.516 Å
2.532 Å
Ni
2.520 Å
b = 20.784 Å
a = 20.784 Å
3.167 Å
3.087 Å
Ca
3.135 Å
b = 20.669 Å
a = 20.825 Å
2.780 Å
2.777 Å
Ti
2.772 Å
b = 20.784 Å
a = 20.784 Å

Figure 5.2: The optimized molecular structures of isolated TCDD, pristine and doped antimonene.

Noteworthy, during cell relaxation constraints were applied on the c vector to keep it fixed at the value of 50 Å to insure enough vacuum preventing any interaction with the image of the cell in z direction. In addition, the lattice angles were also kept fixed at values 90°, 90° and 120°. In other words, only a and b vectors, as well as the atomic position, were allowed to change during the relaxation.

Table 5.2: Lattice and geometrical parameters of the optimized supercells depicted in Figure 5.2. X = Sb, Ni, Ca, or Ti.

systems	a (Å)	b (Å)	Sb-X (Å)	Sb-X-Sb (°)	Torsion Angle (°)
Sb	20.784	20.784	2.905	91.4	53.6
Ni-doped-Sb	20.708	20.550	2.516 2.520 2.532	95.3 109.0 112.1	44.4
Ca-doped-Sb	20.825	20.669	3.167 3.135 3.087	97.7 103.1 105.1	46.8
Ti-doped-Sb	20.698	20.707	2.780 2.772 2.777	104.6 105.0 106.8	40.4

5.2.2 Computational Details

This study is based on DFT calculations performed using the PBE functional, which is a widely used generalized gradient approximation (GGA) functional for the exchange-correlation energy (Perdew et al., 1996). Using the CP2K software package (Hutter et al., 2014; Kühne et al., 2020), the Gaussian and plane waves (GPW) method (Lippert et al., 1997), which is efficiently implemented in the QuickStep module (VandeVondele et al., 2005), has been employed. This method requires the user to provide the program with both a molecular orbital basis set and a pseudopotential. For more details on the GPW method see section 2.1.1 in chapter 2.

As recommended by CP2K manual, the basis set DZVP-MOLOPT-SR-GTH (for Sb, Ca, Ni, and Ti) and DZVP-MOLOPT-GTH (for the all the other atoms) (VandeVondele and Hutter, 2007) and the GTH-PBE pseudopotential (Krack, 2005) were employed. To account for van der Waals (vdW) interactions, which are expected to play a crucial role in the adsorption of TCDD on the surface of a 2D antimonene, the D3 dispersion correction (Grimme et al., 2011) has been employed. Finally, periodic boundary conditions (PBC) were applied in all the computations.

Adsorption Energies

The adsorption energies of TCDD on antimonene and doped-antimonene were calculated as follows:

$$\Delta E = E_{\text{antimonene+TCDD}} - E_{\text{antimonene}} - E_{\text{TCDD}} \tag{5.1}$$

where $E_{\text{antimonene+TCDD}}$ is the total energy of the optimized structure of antimonene-TCDD complex, while E_{TCDD} and $E_{\text{antimonene}}$ are the energies of the optimized structures of the isolated dioxin molecule and the isolated antimonene surface, respectively.

BSSE-Corrected Interaction Energies

The basis set superposition error (BSSE) is a computational error in quantum chemistry that arises when finite basis sets are used. As atoms of interacting molecules/fragments approach each other, their basis functions overlapwhich may introduce an error when comparing energies (Van Mourik et al., 1998). Therefore, the BSSE method, as implemented in CP2K (Vilela Oliveira et al., 2019), has been employed to calculate the BSSE values for the investigated systems. Technical details about how to perform such calculations using CP2K are given in appendix C, section C.1.2.

The adsorption energies presented in this work were corrected according to the following:

$$\Delta E_{\text{corrected}} = \Delta E - \text{BSSE} \tag{5.2}$$

where ΔE is the energy calculated from Eq. 5.1.

Charge Density and Density of States

To gain insights into the adsorbate/adsorbent interaction, further calculations (namely; the charge density differences ($\Delta\rho(\mathbf{r})$) and partial density of states (PDOS)) were performed on the optimized structures of selected complexes at the same level of theory mentioned above. The charge density difference is given by the formula:

$$\Delta\rho(\mathbf{r}) = \rho_{\text{antimonene+TCDD}} - \rho_{\text{antimonene}} - \rho_{\text{TCDD}} \tag{5.3}$$

5.3 Results and Discussion

5.3.1 Adsorption of TCDD on pristine and doped antimonene

The orientation of a molecule relative to the surface is crucial for the interaction between the adsorbent and the adsorbate. In this study, three initial configurations of antimonene/TCDD complexes were considered: (1) TCDD parallel to the antimonene layer through hexagonal rings (denoted as Sb-TCDD), (2) TCDD standing perpendicular to antimonene through Cl atoms (denoted as Sb-TCDD-Cl), and (3) TCDD standing perpendicular to antimonene through two hydrogen atoms with a bridged oxygen atom (denoted as Sb-TCDD-O). These three configurations were also examined for the adsorption of TCDD on doped antimonene. In total, 12 complex structures were initially considered.

Before calculating the interaction strengths of the different configurations, i.e., in terms of their adsorption energies or the BSSE-corrected interaction energies, geometry optimization calculations were performed to insure that a minimum structure of each complex has been obtained. The calculations revealed that both Ca- and Ti-doped-antimonene were not able to adsorb TCCD through the orientation in which TCDD is standing perpendicular to the surface via the H and O atoms. As illustrated in Figure 5.3, in these particular cases, the initial configurations (i.e., X-TCDD-O where X is Ca or Ti) are consistently optimized to yield the parallel configurations (i.e., X-TCDD). This observation is partially consistent with a recent study by Zhang et al. (2017) on the adsoption of TCDD on the surface of phosphorene. “Partially” because the authors reported that neither Ca-doped-phosphorene nor Ti-doped-phosphorene could adsorb TCDD through standing orientations (regardless of being attached via Cl or O atoms). However, optimized structures of TCDD adsorbed on Ca- and Ti-doped-antimonene while standing via the Cl atoms, i.e. Ca-TCDD-Cl and Ti-TCDD-Cl, respectively, have been obtained (see Figure 5.4).

Except for the two cases mentioned above, the remaining 10 complexes were successfully optimized to achieve the desired orientations of TCDD relative to antimonene and doped-antimonene surfaces. Initially, configurations close to the target orientations were used, and the geometry optimization process made slight adjustments to the TCDD direction towards the antimonene surface. This adjustment was done in a manner that maximizes the binding strength between the two species while considering the initial geometry.

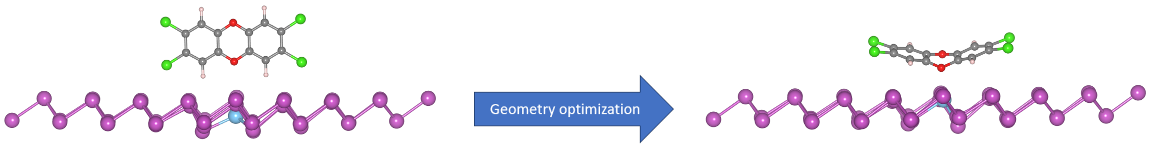

Initial configuration
X-TCDD-O

After optimization
X-TCDD

Figure 5.3: Illustration of the incapability to obtain optimized structures of TCDD perpendicular to the surface of X-doped-antimonene (X=Ca, Ti) through the O atom, and the tendency of these standing configurations to turn to the parallel ones.

For instance, when TCDD is positioned on antimonene with two chlorine atoms, the geometry relaxation process rotates and tilts the TCDD molecule slightly. This ensures that the two chlorine atoms are positioned as closely as possible to two Sb atoms in the case of pristine antimonene, or to a dopant atom and an Sb atom in the case of Ca- and Ti-doped antimonene. All optimized complexes can be found in Figure 5.4.

Interestingly, in the aforementioned study of TCDD adsorption on phosphorene by Zhang et al. (2017), the authors reported that the phosphorene layer tends to bend due to its strong interaction with TCDD. In contrast to phosphorene, neither pristine antimonene nor doped antimonene exhibit such a phenomen. As mentioned earlier, only a slight local distortion around the dopant atom compared with pristine antimonene was observed, but adsorption of TCDD did not cause any significant change to the adsorbents compared with the isolated surfaces. In other words, the antimonene layer sustains its planarity in all perpendicular cases and the case of parallel TCDD to pristine antimonene. In the latter case this could be attributed to the equal effect of all the Sb atoms. However, when TCDD is lying flat on doped antimonene the dopant atom attracts the oxygen atoms resulting in deformation of the planarity of TCDD (i.e., TCDD is bent) showing that the dopant atoms in doped antimonene have superior interactions with TCDD. As a consequence of this bending, the closest TCDD-adsorbate distance decreases from 3.88 Å (i.e., in the case of Sb-TCDD) to 2.35 Å and 2.64 Å (in the cases of Ti-TCDD and Ca-TCDD, respectively). Contrary to Ti-TCDD and Ca-TCDD, one can see that the structure of Ni-TCDD is, to large extent, similar to Sb-TCDD in terms of the planar structure of TCDD and the Ni-O distance ≈ 3.85 Å. This could be

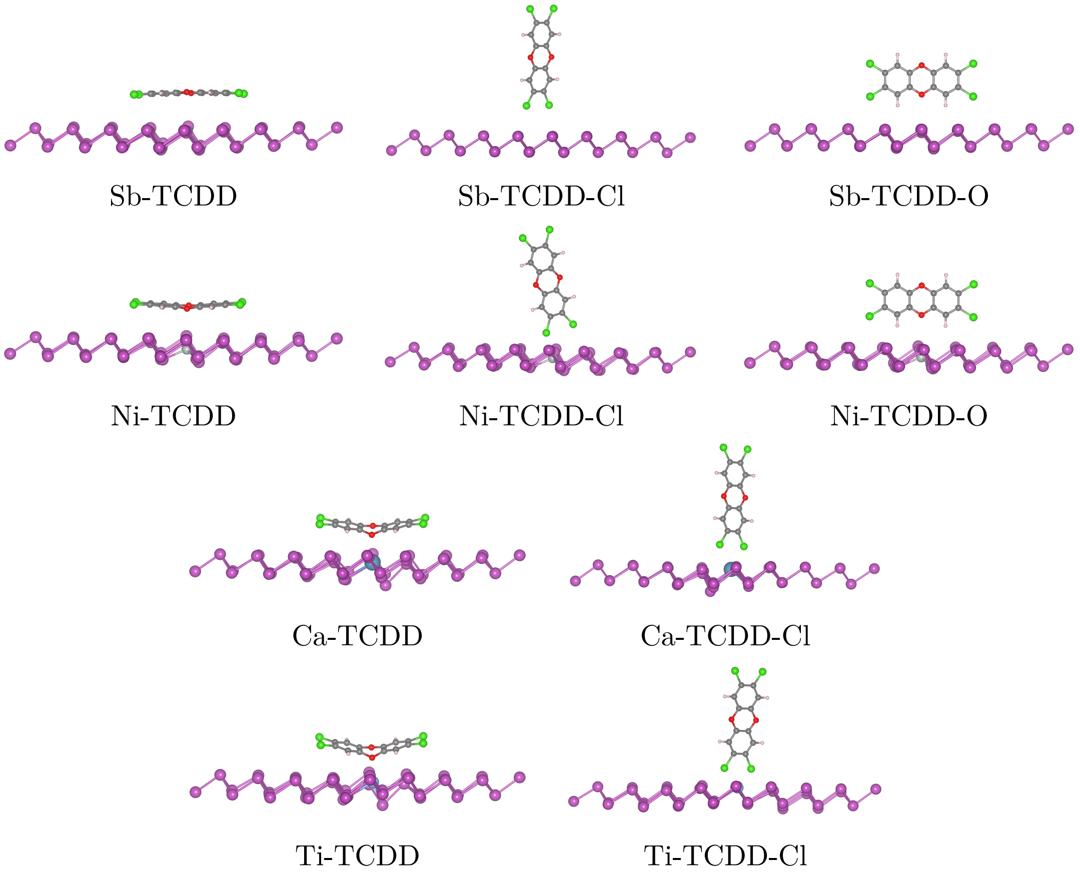
Sb-TCDD
Sb-TCDD-Cl
Sb-TCDD-O
Ni-TCDD
Ni-TCDD-Cl
Ni-TCDD-O
Ca-TCDD
Ca-TCDD-Cl
Ti-TCDD
Ti-TCDD-Cl

Figure 5.4: Optimized geometries of all considered configurations of the TCDD/Sb and TCDD/doped-Sb complexes.

rationalized based on the relatively small atomic size of the Ni atom compared with Sb preventing it from interacting with TCDD, otherwise, TCDD would either be too close to the Sb atoms or bent too much, and one may assume that none of these two options would be chemically stable.

The stability of the investigated complexes (depicted in Figure 5.4) and the trend of the strength of the adsorbate-adsorbent interaction in these complexes have been studied based on their adsorption energies that were calculated according to Eq 5.2. Figure 5.5 summarizes the calculated energies, while the actual values are given in Table 5.3. Inspecting these data, it has been noticed that all configurations are stable (i.e., their adsorption energies have negative signs).

Zhang et al. (2017) and Zhou et al. (2018b) reported that, regardless of the kind of substrate material, the strongest interaction between TCDD and a 2D surface takes place when TCDD is lying parallel to the surface. Inspection of the data displayed

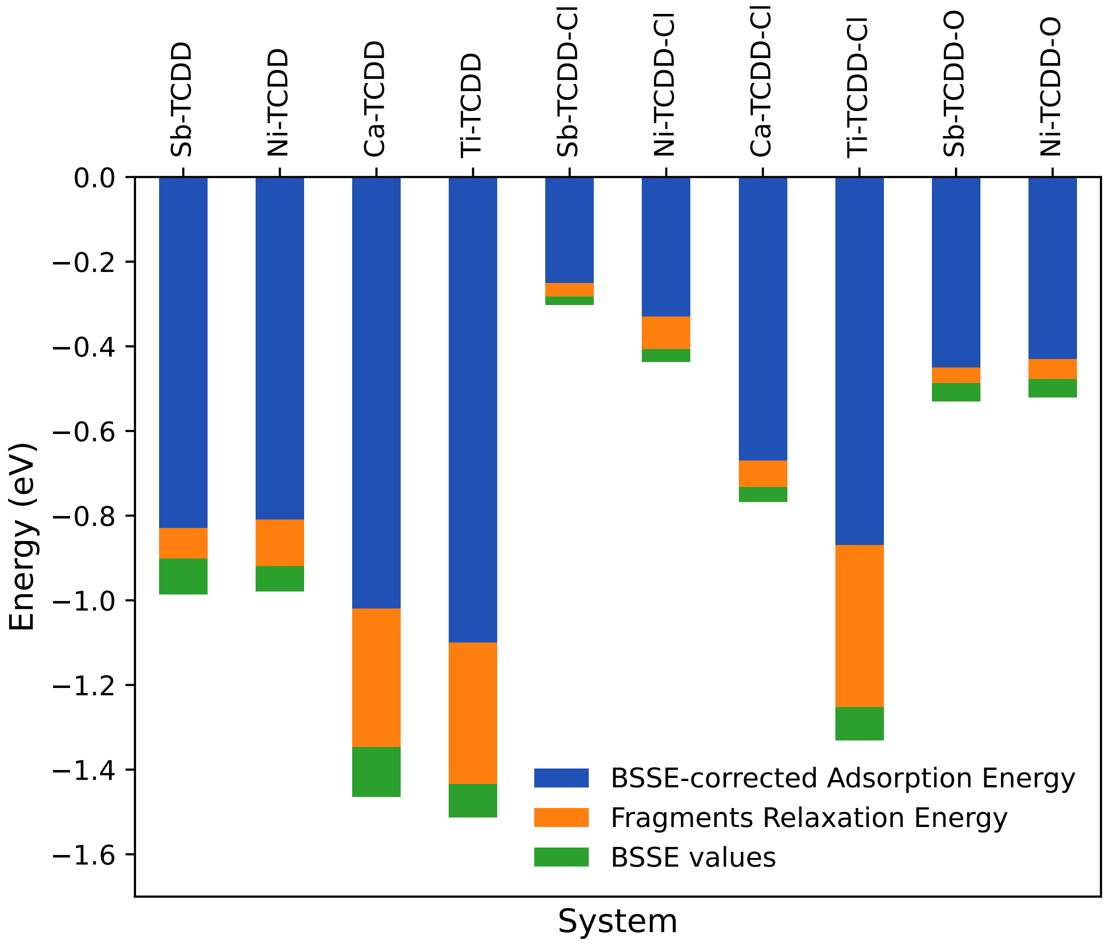

Figure 5.5: BSSE-corrected adsorption energies for the complexes depicted in Figure 5.4, their fragments relaxation energies (higher values indicate larger deformation of TCDD upon adsorption), and the corresponding basis set superposition error (BSSE) values.

in Figure 5.5 reveals that similar to other 2D materials, TCDD prefers the parallel configuration on both pristine and doped-antimonene. The next preference orientation is the perpendicular one through the Cl atoms. Lastly, comes the standing-via-O-atoms orientation.

It is noteworthy that many similar studies (Zhang et al., 2014, 2017; Zhou et al., 2018b) on different materials used almost the same setup of calculation and level of theory as employed in the current study. Hence, one can directly compare the values of adsorption energies for our systems with their counterparts in these previous studies. Interestingly, it has been found that the adsorption energy in case of pristine antimonene remarkably exceeds that of previously studied materials, including graphene (Zhang et al., 2014), carbon nanotube (Ganji et al., 2015), BN nanotube (Ganji et al., 2015), and phosphorene (Zhang et al., 2017), by roughly 50% to 250%.

Table 5.3: Numerical values (in eV) of BSSE-corrected adsorption energies for the complexes depicted in Figure 5.4, their fragments relaxation energies (larger values indicate larger deformation of TCDD upon adsorption), and the corresponding basis set superposition error (BSSE) values.

System	BSSE-corrected Adsorption Energy	Fragments Relaxation Energy	BSSE values
Sb-TCDD	-0.83	-0.07	-0.08
Ni-TCDD	-0.81	-0.11	-0.06
Ca-TCDD	-1.02	-0.33	-0.12
Ti-TCDD	-1.10	-0.33	-0.08
Sb-TCDD-Cl	-0.25	-0.03	-0.02
Ni-TCDD-Cl	-0.33	-0.08	-0.03
Ca-TCDD-Cl	-0.67	-0.06	-0.04
Ti-TCDD-Cl	-0.87	-0.38	-0.08
Sb-TCDD-O	-0.45	-0.04	-0.04
Ni-TCDD-O	-0.43	-0.05	-0.04

Given that pristine antimonene has such a superior ability to bind TCDD, particularly in the parallel configuration, raises the question of whether doping improves its performance. Comparing the values of adsorption energies of the pristine antimonene complexes with their doped antimonene counterparts indicates that in the case of vertical adsorption, i.e. in the X-TCDD-Cl configurations (where X=Ni, Ca or Ti), one can see how doping significantly improved the performance and raised the adsorption energy from -0.25 eV (in pristine antimonene) to -0.87 (in Ti-doped antimonene). To be specific, doping by Ni, Ca or Ti increased the adsorption energies by 32%, 168%, or 248%, respectively. On the other hand, the effect of doping is much less pronounced in the parallel configuration since the adsorption energy in the case of pristine antimonene is relatively high (namely, -0.83 eV). For this configuration, doping by Ca and Ti enhances the adsorption energies by 23% and 32%, respectively, while doping by Ni decreases the adsorption energy by 2%. For the standing-via-O (i.e., X-TCDD-O) configuration, doping by Ni showed almost no effect on the adsorption energy.

Finally, by examining the data in Figure 5.5 and Table 5.3, the fragments relaxation energy (i.e., the difference between the adsorption energy calculated considering optimized separate fragments and the adsorption energy calculated considering fragments at the adsorption structure) shows the degree of structural deformation occurs in the TCDD structure upon adsorption. For instance, comparing pristine antimonene with Ni-doped antimonene, one can see that the adsorption does not affect the planar structure of TCDD. On the contrary, comparing pristine antimonene with Ti-doped antimonene, it is clear that the adsorption significantly affects the geometry of TCDD, particularly the planar structure of TCDD in the parallel configurations.

5.3.2 Electronic properties

Since the adsorption energies calculations indicated that the parallel configuration is the most preferred one for both pristine and doped antimonene, the subsequent analysis will focus solely on this subset of systems.

5.3.2.1 Charges density differences

In order to analyze the electronic interaction between TCDD with antimonene and doped antimonene, the charge density differences $\Delta\rho(\mathbf{r})$, defined as the difference between the total charge density of X-TCDD complex (where X=Sb, Ni, Ca or Ti) with the subtraction of the sum of the charge density of the isolated TCDD and surface (cf. Eq. 5.3), were calculated. To obtain numerical values of transferred charge, the plane-averaged charge density differences $\Delta\rho(z)$ along the normal direction (z) of the surface (i.e., antimonene or doped antimonene) is calculated by integrating $\Delta\rho(\mathbf{r})$ within the basal plane at the z point. The amount of transferred charge at the point z ($\Delta Q(z)$) is computed as follows:

$$\Delta Q(z) = \int_{-\infty}^{z} \Delta\rho(z')dz' \tag{5.4}$$

The isosurfaces of $\Delta\rho(\mathbf{r})$, together with the $\Delta\rho(z)$ and $\Delta Q(z)$ curves are displayed in Figure 5.6.

Figure 5.6 shows that, in all cases, charge is transferred from TCDD to the antimonene surface. This can be seen from the isosureface plots in the top row of Figure 5.6 as well as the $\Delta\rho(z)$ and $\Delta Q(z)$ curves. Moreover, the charge density differences plots reveal a clear modification in the charge distribution (as well as the amount of charge transferred) in Ca- and Ti-doped-antimonene relative to pristine and Ni-doped-antimonene.

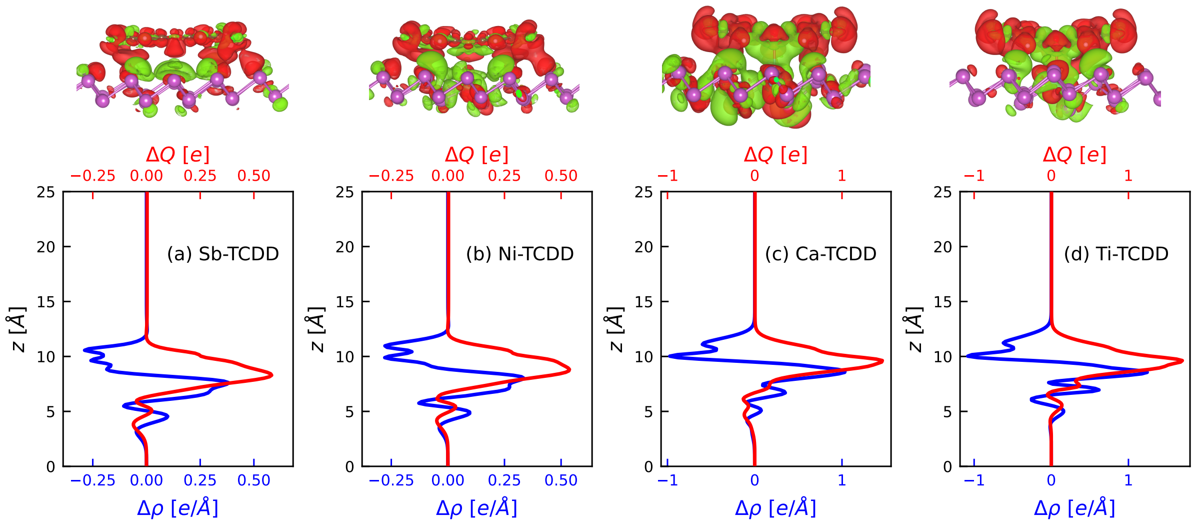

Figure 5.6: Top row: charge density difference isosurface plots (color map shows green for charge accumulation, while red is for depletion) of parallel TCDD over antimonene. Bottom row: $\Delta\rho(z)$ and $\Delta Q(z)$ curves of the corresponding isosurface.

The charge distribution in the cases of Ca- and Ti-doped-antimonene aligns with the relatively shorter distance between TCDD and doped antimonene as comnpared to the distance between TCDD and pristine and Ni-doped-antimonene. In other words, together the results displayed in Figure 5.6 and the molecular structures shown in Figure 5.4 suggest that the dominant interaction in the cases of Sb-TCDD and Ni-TCDD is VdW, whereas in the case of Ca-TCDD and Ti-TCDD a polar covalent bond could be formed between the dopant atom and the oxygen atom of TCDD.

5.3.2.2 Density of states

To gain a deeper understanding of the electronic properties of the investigated systems, the DOSs were calculated for the isolated pristine and doped antimonene, as well as for the complexes after adsorbing TCDD (focusing only on parallel configurations). Since there are two variables that could influence the electronic properties (i.e., doping and TCDD adsorption), the DOS will be examined in the two cases:

- Figure 5.7 displays the DOS of pristine and doped antimonene to explore the effect of doping.
- Figure 5.8 shows the DOS of each case before and after adsorption to investigate

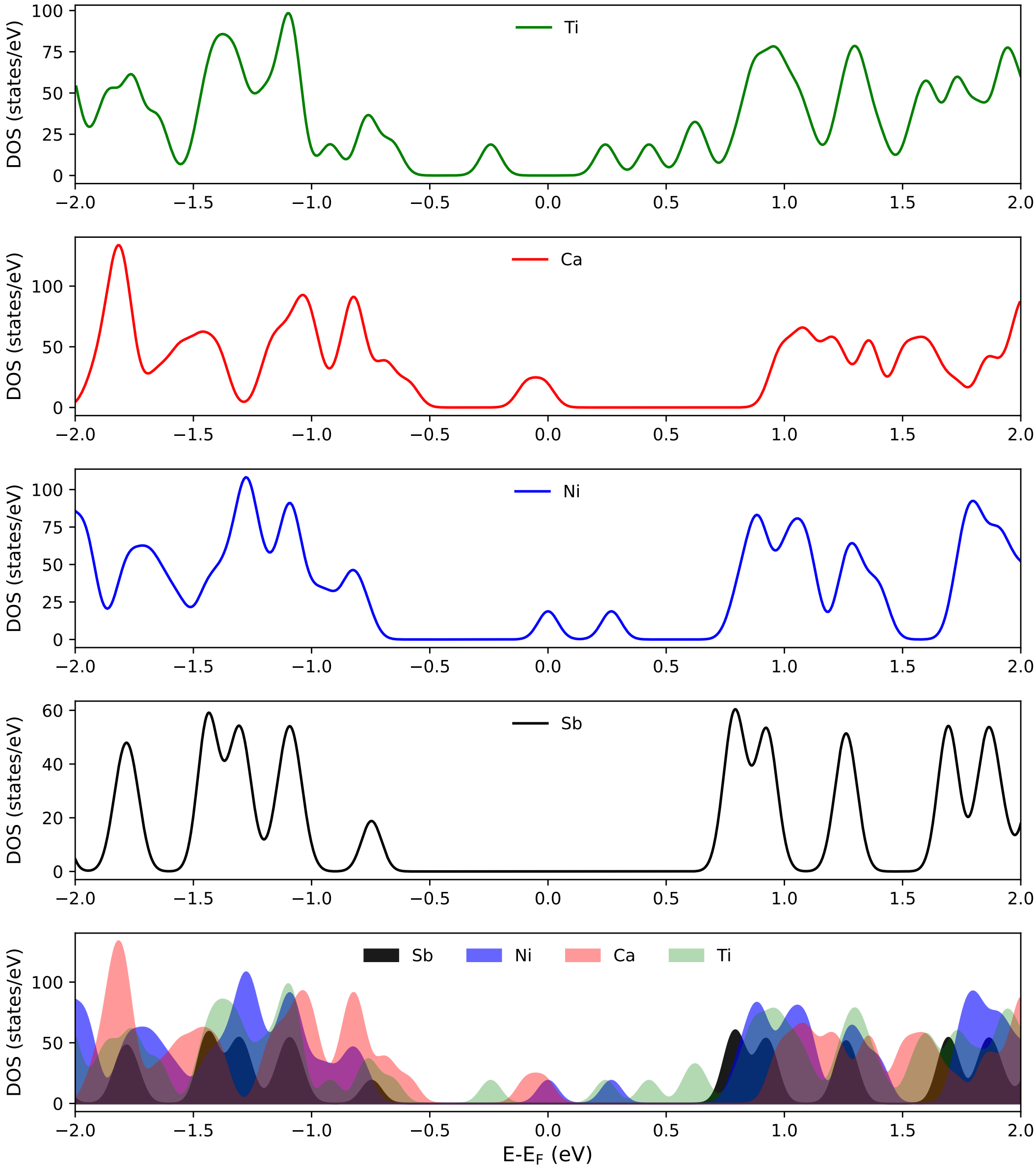

Figure 5.7: DOS of antimonene and doped antimonene. In the bottom row a direct comparison is given.

the effect of TCDD adsorption.

It is clear, from Figure 5.7, that doping has a substantial effect on the electronic properties of 2D antimonene. Namely, some peaks appear around the Fermi level in the DOS of Ni- and Ca-doped antimonene which are missing in the pristine case. Although Ti-doped antimonene has no peaks at the Fermi level, the band gap is significantly reduced relative to that of pristine antimonene. On the other hand, the adsorption of TCDD insignificantly affects the electronic properties of antimonene. As can be seen in Figure 5.8, TCDD adsorption on both pristine and doped antimonene substrates barely affects their electronic properties.

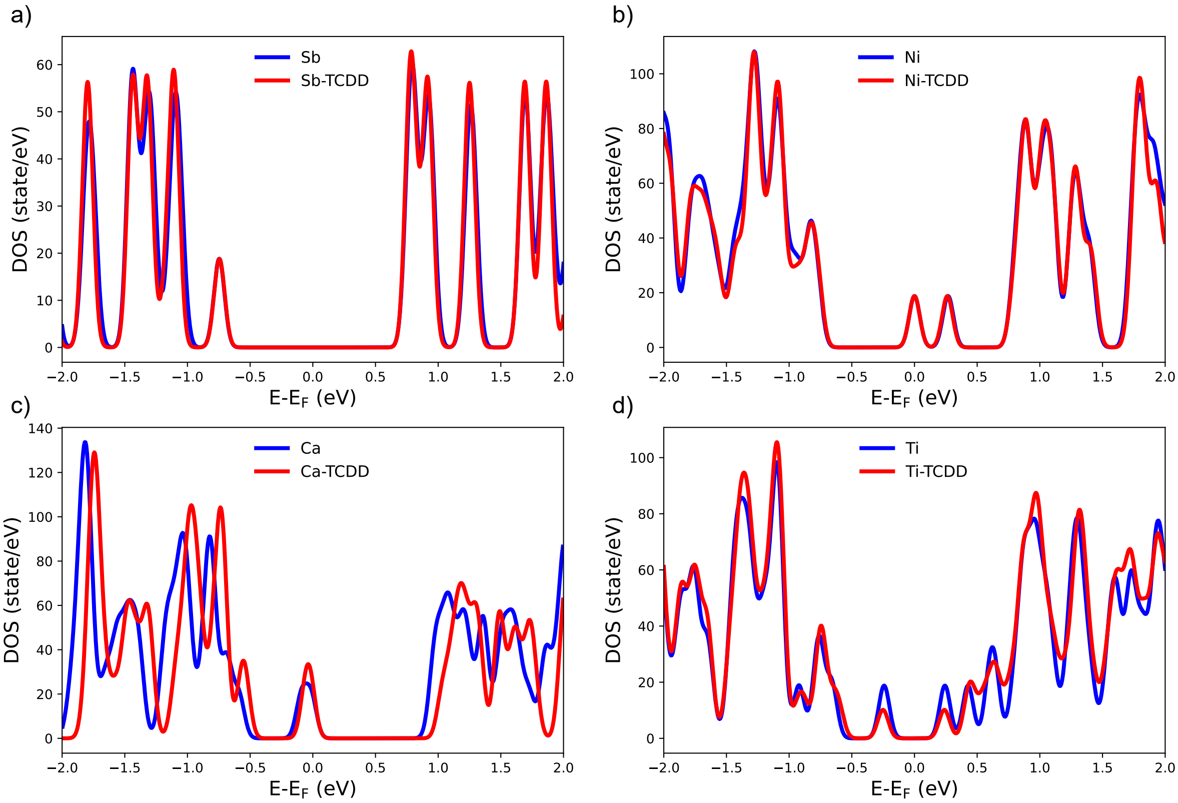

Figure 5.8: DOS of pristine and doped antimonene versus their corresponding complexes (only parallel configuration)

To get a deeper understanding of the origin of the peaks around the Fermi level that appear in the DOS of doped antimonene and to explore whether TCDD has any influence on the electronic properties of the systems, the PDOS of the dopant atoms (as well as the O atoms of TCDD) have been calculated and are given in Figure 5.9. Although it is clear that these peaks exist because of the dopant atoms, the PDOS plots show that their magnitudes do not coincide with the corresponding peaks in the total DOS. This implies that the Sb atoms surrounding the dopants may be also involved. Finally, the PDOS of the O atoms of TCDD confirm that TCDD adsorption on these substrates has no direct contribution to the electronic states around the Fermi level.

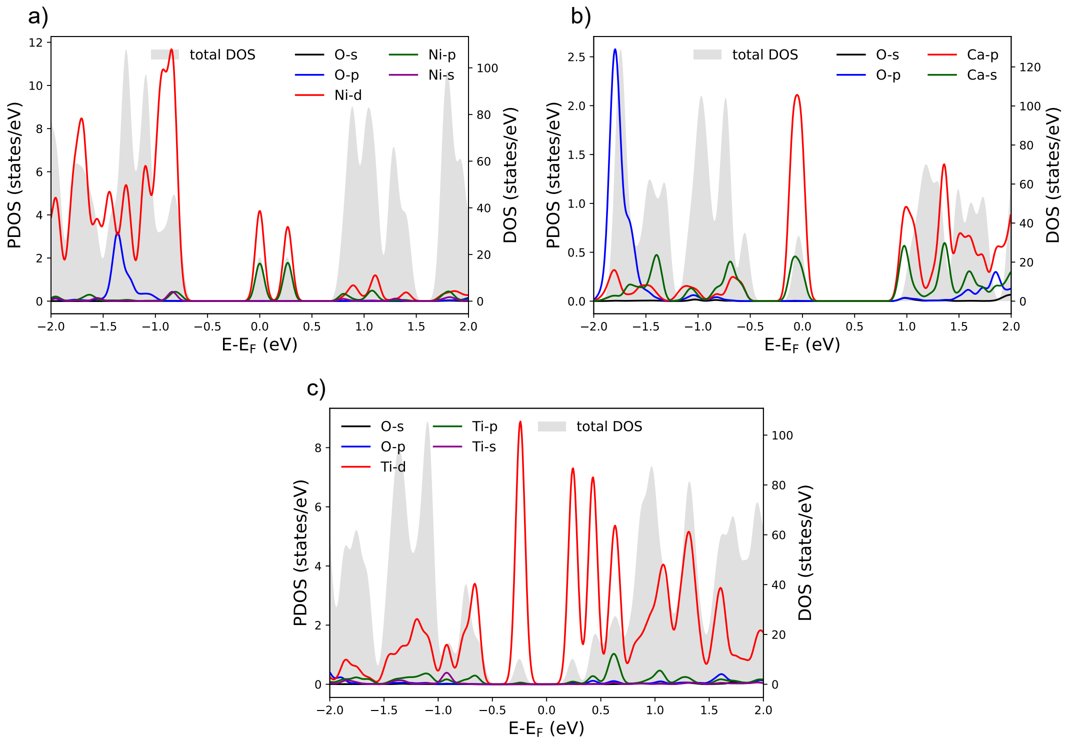

Figure 5.9: PDOS of oxygen (TCDD) and dopant atoms of the doped antimonene. The corresponding total DOS for each system is shown in the background.

5.4 Summary

The current work represents an endeavor to explore the capability of antimonene as a potential candidate for capturing the highly toxic dioxin molecule 2,3,7,8-tetrachlorodibenzo-p-dioxin (TCDD). DFT has been utilized to calculate the thermochemically stable structures of several adsorption configurations of TCDD on the surface of pristine as well as Ni-, Ca- and Ti-doped antimonene. While all the studied antimonene forms showed remarkable capability to capture TCDD, it has been found that doping (especially, by Ca and Ti) could improve the performance of pristine antimonene considering the most stable TCDD/antimonene interaction configuration (i.e., the parallel configuration). Specifically, doping antimonene with Ca or Ti enhances its ability to capture TCDD by 25% or 30%, respectively, whereas Ni-doped antimonene showed TCDD capture capability less than pristine antimonene by 5%. In addition, doping antimonene with Ca and Ti significantly increased its ability to capture TCDD through the configuration in which TCDD is perpendicular to the antimonene surface through the two Cl atoms.

The findings of the current study have been discussed in the light of the adsorption energies, the charge transfer between the adsorbent and the adsorbate, and the electronic properties of the complexes under investigation. Interestingly, the comparison between the results reported in the present work and the findings of similar studies revealed that pristine antimonene outperforms the other pristine nanomaterials (including phosphorene, pristine graphene, and BN nanotube) in capturing TCDD. Therefore, this study not only proposes antimonene as a promising candidate for dioxins capture but it also could be the basis for further investigations on tuning the properties of antimonene to maximize its capability to be utilized in similar environmental applications.

6 Summary and Outlook

The remarkable properties of 2D materials and their tunability position them as versatile candidates for a wide range of applications across diverse fields. One particularly promising avenue is harnessing the unique attributes of 2D materials (such as their high surface area and their ability to adsorb other molecules) and utilizing them as green solutions in the realm of environmental remediation. The present thesis compiles three case studies, namely: confined water dynamics/diffusion, polymers dynamics and their interaction with graphene in solution, and toxic molecule capture by 2D antimonene. Through this exploration, the aim is to contribute nuanced insights into understanding 2D materials.

The investigation of water confinement between graphene oxide (GO) layers highlighted the intricate dynamics of water molecules in restricted spaces. Extended tight-binding (xTB)-based MD simulations have been conducted with a focus on the impact of confinement on 2D self-diffusion of water. This topic had shown conflicting conclusions in previous studies utilizing different structural models and levels of theories, namely; density functional theory (DFT) versus classical force field. By designing six models representing varying inter-layer distances and GO functional groups orderings, the study aimed to bridge the gap between the previous reports on the topic. Results indicated that despite minor structural variations upon solvation, the presence of H-bonded bridges connecting GO layers significantly slowed down water diffusion. The competition between inter-layer H-bonding and intra-water liberation forces emerged as a crucial factor behind this slowdown, introducing a new aspect in understanding the effect of GO layers on water diffusion. These findings bear potential implications in membrane technology, offering insights for designing membranes that selectively permit species' movement while delaying others, thus enabling applications in selective separation processes.

The exploration of polymer behavior in diverse environments, particularly in the presence of graphene, unveiled valuable insights into the interaction and response of different polymer types, including polyethylene (PE), polyethylene oxide (PEO), and polystyrene

(PS), to various environmental situations. The study presented in chapter 4 focused on the dynamics of the different polymers at the graphene/water interface through analyzing their radius of gyration, solvent accessible surface area, interaction energies, and partial density profiles along z-axis, elucidating how different polymer types responded to graphene interaction and confinement. Notably, the ability of graphene to effectively capture the investigated polymers in confined spaces demonstrated promise for the removal of nanoplastics from aqueous environments. Further investigations aimed to delve into polymer and water diffusion under diverse conditions, necessitating more extensive molecular dynamics trajectories to gain a more detailed understanding of these dynamic processes.

In chapter 5, the study focused on the potential of antimonene to capture the highly toxic organic molecule 2,3,7,8-tetrachlorodibenzo-p-dioxin (TCDD). Utilizing DFT, the results revealed significant capability for antimonene in capturing TCDD. Different dopants (namely; Ni, Ca, and Ti) were explored for their impact on antimonene's performance in capturing TCDD. The results demonstrated that while doping with Ca and Ti improved antimonene's ability to capture TCDD, Ni-doped antimonene showed a marginal decrease in efficiency compared to pristine antimonene, indicating nuanced effects of doping on the material's capturing capabilities. These findings open avenues for further investigations aimed at optimizing antimonene's properties for potential applications in environmental remediation and toxic molecule removal.

The integration of insights from the aforementioned studies enhances our understanding of the behavior of 2D materials across diverse scenarios. While individual studies have delved into specific aspects their collective implications extend to broader fields such as membrane technology, environmental remediation, and tailored materials design for adsorption purposes. These findings form the foundation for future research endeavors, including scaling up simulations to emulate bulk-like behavior, crafting membranes with precise permeability control, and optimizing 2D materials for targeted environmental applications. Moreover, this work facilitates a deeper comprehension of toxic molecule capture dynamics, paving the way for the development of materials tailored for environmental remediation.

In conclusion, the insights derived from these studies, while essential for foundational understanding, should be viewed as initial steps in paving the way for potential interdisciplinary research. These findings have the capacity to inspire collaborations among material scientists, environmental engineers, and computational experts. It is crucial to acknowledge the preliminary nature of these studies, as they serve as building blocks rather than direct blueprints for real-world applications. The practical implications in environmental remediation, 2D materials design, and membrane technology underscore the potential significance of these foundational findings for future advancements in these domains. The interconnected nature of these studies contributes to a holistic understanding of 2D materials behavior, laying the groundwork for further exploration and innovation in the long journey toward practical applications.

A Supplementary Information for Chapter 3

A.1 Chemical reactivity of GO in neat water

The oxygen functions on the GO surface can be considered as potential active sites for chemical reactions between GO and the surrounding medium. Based on DFT MD simulations, Mouhat et al. (2020) observed that GO is chemically active in water and they reported the occurrence of two chemical reactions. Namely, (1) the epoxide ring opening through breaking of one of the C-O bonds, and (2) the deprotonation of OH groups. Interestingly, they did not observe the disruption of the C-C bond of an epoxide to form 1,2-ether that was proposed by Savazzi et al. (2018).

Recently, David and Kumar (2021) aimed at investigating the chemical reactivity of GO in neat water in more details. Therefore, they performed DFT-based MD simulations for hydrated GO models with two different oxidation ratios, namely, 25% and 50%. In addition, they considered five different initial configurations (extracted from prior force field MD simulations) for each model as starting points for 25 ps MD trajectory each (i.e., resulting in a total 125 ps for each oxidation level). This approach (i.e., sampling different oxidation levels and considering different configurations for each oxidation level as starting points resembling longer time scale) allowed them to observe even more chemical events not reported by Mouhat et al. (2020). One should note that the computational setup has been different in these two studies, e.g., with regard to the density functionals used.

David and Kumar (2021) found that the higher oxidation level, the more reactive GO is (i.e., in terms of the formation of new stable chemical species). Furthermore, they attributed the epoxide ring opening (and epoxide closing) to a release of the strain of the GO sheet. More important, and in contrast to the work by Mouhat et al. (2020), they concluded that the accessible time scales of DFT-based MD simulations are not enough to observe such rare (i.e., in terms of the number of functional groups that are involved) chemical events.

One can view these two papers as a manifestation of the fact that the observation of reactive events in GO might strongly depend on the used computational method and structure. The xTB method employed for the present simulations is perhaps not as accurate as DFT, but it holds the promise to enable long simulation times at modest effort and reasonable accuracy. Leaving aside a benchmarking of xTB for GO applications, which would be worth pursuing in future, the absence of chemical reactions in the current simulations could be attributed to several factors. For example, the run time may be insufficient for these reactions to take place and/or the arrangements of the functional groups in our models insure less strain of the GO sheet. Another important factor could be the ultra-confinement of the hydrated models of the present work since all the above mentioned studies considered a relatively larger inter-layer spacing (about 16 Å in (Mouhat et al., 2020) and 104 Å, including 70 Å of vacuum, in (David and Kumar, 2021)).

Although this situation is not satisfactory as far as reactive events are concerned, one may argue that such relatively rare events should have a minor effect on the main findings of the current study, i.e. the role of GO-H_2O-GO H-bridges in slowing down confined water diffusion (see the section A.2 below).

A.2 Validation of xTB

In order to evaluate the capability of the xTB method to describe the H-Bonded bridges relative to DFT, a smaller model consists of two GO sheets and one water molecule (cf. Figure A.1(b)) was constructed. To scan the potential energy surface with respect to the inter-layer spacing (and, hence, the formation of GO-water-GO HB bridge), the distance between the GO sheets was varied from 6.5 to 10 Å. The geometries of eight structures were partially optimized (i.e., constraint was applied on the carbon skeleton to preserve the desired inter-layer distance), and their energies were obtained at both xTB (Grimme et al., 2017) and DFT levels of theories. The DFT calculations were carried out using the PBE (Perdew et al., 1996) functional and the DZVP-GTH-PBE (Goedecker et al., 1996) basis set. The calculations were carried out using the CP2K software package (Hutter et al., 2014; Kühne et al., 2020).

As can be seen in Figure A.1(a), the energy profile obtained using the xTB method shows a reasonable agreement with its DFT counterpart. Both methods reveal that 6.5 Å is the optimum inter-layer distance for this model which insure the formation of a HB bridge consists of two strong HBs. Increasing the inter-layer distance weakens the HBs and eventually causes the deformation of the HB bridge, hence, rising up the energy.

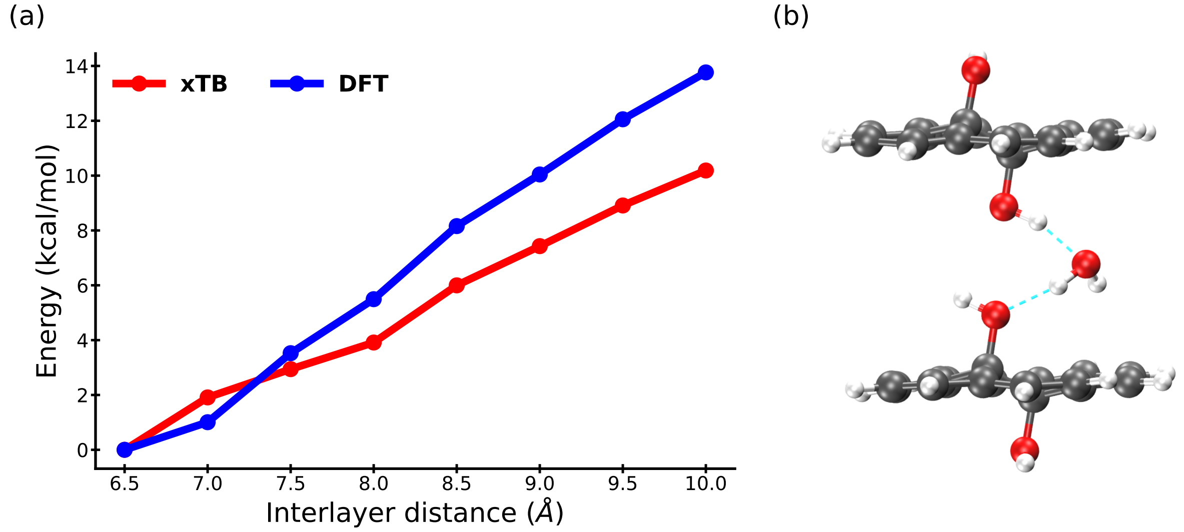

Figure A.1: (a) Potential energy surface of GO-water-GO H-bonded bridge, and (b) H-bonded bridge model.

A.3 Home-made python scripts for HBs-bridges analysis

This section provides pieces of the python code that has been used to analyze the HBs bridges.

```python
import numpy as np
```

First, the HBs were analyzed based on geometrical criteria. This was done by reading the xyz coordinates of all the atoms along the trajectory. Then the distances between the atoms, and the angles between the three atoms that potentially could form a HB were calculated. If the HBs' criteria were met, information (namely; time step, values of the donor-acceptor distance and acceptor-donor-H angle, and the indices of the three atoms) about this HB will be printed in an output file. Afterwards, the following python functions were used to analyze these information and to detect which of the found HBs are involved in a HB-bridge.

```python
def Read_HBs_data_file(fname=None):
    """
    Read data from a file containing hydrogen bond information.

    Parameters:
    - fname (str): The file name or path to the hydrogen bond data file.

    Returns:
    - NHBs_steps (numpy.ndarray): Steps and counts of hydrogen bonds.
    - HBs (numpy.ndarray): Indices of hydrogen bonds.
    - HBs_data (numpy.ndarray): Numerical data associated with hydrogen bonds.
    """
    with open(fname, 'r') as f:
        all_data = [line.split() for line in f if line and line[0] != '#']

    NHBs_steps = np.array([x for x in all_data if len(x) == 2], dtype=int)
    HBs_info = np.array([x for x in all_data if len(x) == 6])
    HBs, HBs_data = HBs_info[:, :3].astype(np.int), HBs_info[:, -3:].astype(np.float)

    return NHBs_steps, HBs, HBs_data
```

```
def Link(b1=None, b2=None):
    """
    Check whether two HBs are linked (i.e., have a common atom).

    Parameters:
    - b1 (list): The indices of the acceptor, donor, and H atoms of the first HB.
    - b2 (list): The indices of the acceptor, donor, and H atoms of the second HB.

    Returns:
    - link (list): The linked hydrogen bonds.

    """
    link = []

    if b1[0] == b2[0]:
        # link
        b1.reverse()
        for bi in range(len(b1)):
            link.append(b1[bi])
        for bj in range(1, len(b2)):
            link.append(b2[bj])

    elif b1[-1] == b2[-1]:
        # link
        b2.reverse()
        for bi in range(len(b1)):
            link.append(b1[bi])
        for bj in range(1, len(b2)):
            link.append(b2[bj])

    elif b1[0] == b2[-1]:
        # link
        # b2.reverse()
        for bj in range(len(b2)):
            link.append(b2[bj])
        for bi in range(1, len(b1)):
            link.append(b1[bi])

    elif b1[-1] == b2[0]:
        # link
        for bi in range(len(b1)):
            link.append(b1[bi])
        for bj in range(1, len(b2)):
            link.append(b2[bj])

    return link
```

```
def Find_Links(List1=None, List2=None):
    """
    Find links between HBs.

    Parameters:
    - List1 (list): The first list of HBs.
    - List2 (list): The second list of HBs.

    Returns:
    - filter_links (list): Filtered list of links between hydrogen bonds.

    Note:
    - If only List1 is provided, it finds links within List1.
    - If both List1 and List2 are provided, it finds links between List1 and List2.
    """
    if List2 is None:
        links = []
        for i in range(len(List1)):
            for j in range((i + 1), len(List1)):

                link = Link(b1=List1[i], b2=List1[j])

                if link:
                    links.append(link)

    elif List1 and List2:
        links = []
        for i in range(len(List1)):
            for j in range(len(List2)):
                ll1, ll2 = List1[i], List2[j]
                ll2.reverse()
                if List1[i][:3] != List2[j] and List1[i][-3:] != List2[j] \
                        and ll1[:3] != ll2 and ll1[-3:] != ll2 \
                        and (List1[i][0] > 204 or List1[i][-1] > 204):
                    link = Link(b1=List1[i], b2=List2[j])
                    if link:
                        links.append(link)

    filter_links = []
    for l in links:
        if l not in filter_links:
            filter_links.append(l)

    return filter_links
```

```
def Filter_duplicated_HB(given_list=None):
    """
    Check if there are duplicated hydrogen bonds in a given list.

    Parameters:
    - given_list (list): The list of hydrogen bonds to check.

    Returns:
    - bool: True if there are no duplicated hydrogen bonds, False otherwise.
    """
    try:
        visited = set()
        for _ in given_list:
            if _ not in visited:
                visited.add(_)
            else:
                raise Exception()
        return True

    except Exception:
        return False
```

```
def Filter_duplicated_link_path(list1=None, list2=None):
    """
    Check if two lists of links have the same set of links.

    Parameters:
    - list1 (list): The first list of links.
    - list2 (list): The second list of links.

    Returns:
    - bool: True if the lists have different sets of links, False otherwise.
    """
    set1 = set(list1)
    set2 = set(list2)
    if set1 == set2:
        return False
    else:
        return True
```

B Supplementary Information for Chapter 4

B.1 Validating the Adequacy of the produced trajectories

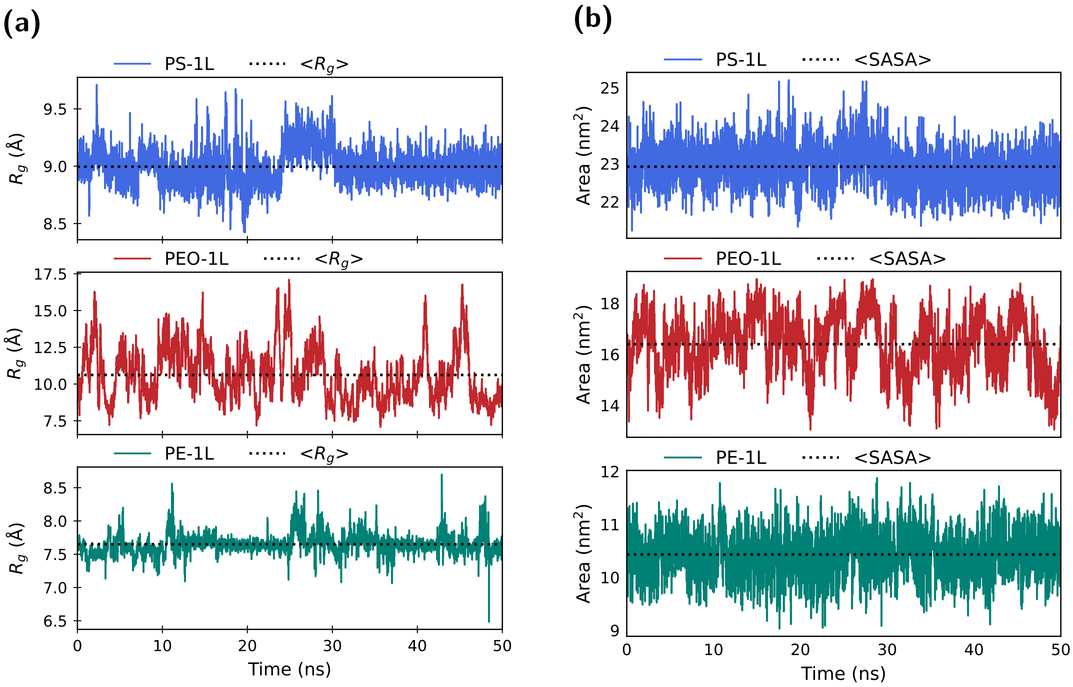

Figure B.1: (a) The radius of gyration of the NPs-1L models from the longer production run (i.e., extra 50 ns of NVT simulations) and (b) their corresponding SASA.

Despite the interesting findings mentioned earlier, the adequacy of the MD simulation runtime remains a point open to debate. While acknowledging the increased computational demands of longer simulations, their significance in validating the system's dynamics, particularly in establishing its equilibrium state, cannot be overstated. In this context, additional 50 ns of NVT MD simulations were carried out for the three NPs-1L systems to corroborate the previously discussed findings presented in Figure 4.7. The resulting R_g and SASA plots from these extended trajectories are visualized in Figure B.1.

In general, the longer MD simulations have exhibited a notable level of consistency with the shorter ones concerning both the average values of R_g and SASA, along with their ranges of fluctuations. This consistency strongly suggests that the systems were, to a certain extent, already in an equilibrium state. Notably, this trend is particularly apparent for the hydrophobic polymers, namely PE and PS.

Regarding PEO, the alignment between the results obtained from both the shorter and longer simulations has also been observed, albeit to a slightly lesser extent. Specifically, in the longer simulation, PEO displayed slightly broader ranges of fluctuations for both R_g and SASA (6.7 Å – 17.1 Å and 11.8 nm^2 – 19.1 nm^2 respectively), compared to the shorter simulation (7.1 Å – 16.7 Å and 12.8 nm^2 – 18.9 nm^2 respectively). This resulted in relatively larger average values of 10.7 Å and 16.3 nm^2 in the longer simulation, compared to 9.5 Å and 15.9 nm^2 in the shorter one.

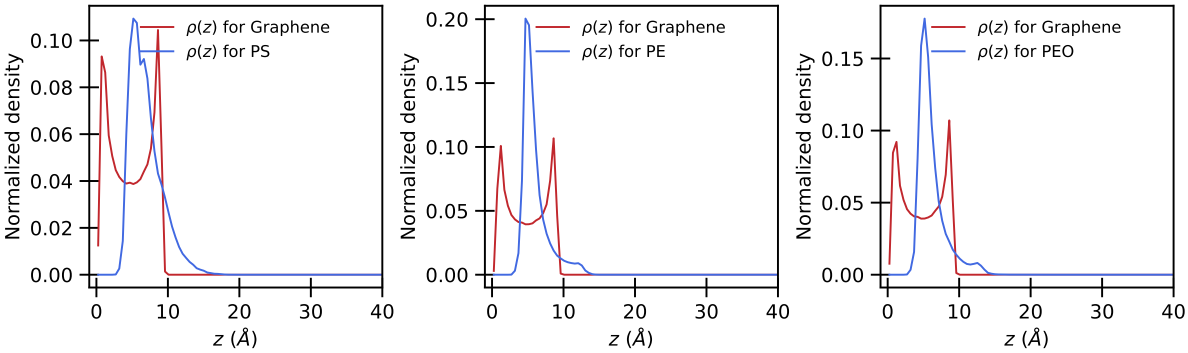

Figure B.2: Partial mass densities along z-axis for NPs and graphene in the NPs-1L models. These results are based on the extended (50 ns of NVT) MD trajectories. For better comparison, all partial densities were normalized according to Eq. 4.4.

C Supplementary Information for Chapter 5

C.1 CP2K input examples:

The objective is to offer specific insights into key selected input parameters, rather than serving as a comprehensive tutorial. For a more in-depth understanding, it is recommended to refer to the CP2K manual.

C.1.1 General example

One of the main blocks that any CP2K input should have is “FORCE_EVAL” which look like the following:

```
&FORCE_EVAL
    METHOD  QS
    STRESS_TENSOR  ANALYTICAL
 ...
&END  FORCE_EVAL
```

Based on the chosen level of theory and the topology of the system, several sub-blocks inside the “FORCE_EVAL” block. Within the context of the current study (i.e., chapter 5), the following two sub-blocks (namely, “DFT” and “SUBSYS”) should appear in the input. The example given below shows the parameters utilized to perform the DFT calculations of the present work. Some comments were added to explain some of the keywords. However, one might need to refer to “ `https://manual.cp2k.org/` ” for more information.

```
  &DFT
      BASIS_SET_FILE_NAME /path/BASIS_MOLOPT
      POTENTIAL_FILE_NAME /path/GTH_POTENTIALS
      CHARGE 0
!       MULTIPLICITY 2  # uncomment (i.e., remove the "!") \
!       LSD T           # in the cases of doped-antimonene
      &SCF
          MAX_SCF     500
          EPS_SCF     1e-5
          SCF_GUESS   RESTART
          &OUTER_SCF   T
            EPS_SCF   1.0E-5
            MAX_SCF   10
          &END OUTER_SCF
          &OT ON
              PRECONDITIONER   FULL_SINGLE_INVERSE
              MINIMIZER        DIIS
          &END OT
      &END SCF
      # Energy grids and corresponding cutoff
      &MGRID
          NGRIDS 4
          CUTOFF 600
          REL_CUTOFF 60
      &END MGRID
      # Functional choice
      &XC
          &XC_FUNCTIONAL PBE
          &END XC_FUNCTIONAL
          DENSITY_CUTOFF      1e-10
          GRADIENT_CUTOFF     1e-10
          TAU_CUTOFF          1e-10
          # Grimme corrections
          &VDW_POTENTIAL
              POTENTIAL_TYPE   PAIR_POTENTIAL
              &PAIR_POTENTIAL
                  R_CUTOFF     16
                  TYPE         DFTD3
                  PARAMETER_FILE_NAME /path/dftd3.dat
                  REFERENCE_FUNCTIONAL PBE
                  LONG_RANGE_CORRECTION T
              &END PAIR_POTENTIAL
          &END VDW_POTENTIAL
      &END XC
      &PRINT
...
      &END PRINT
  &END DFT
  &SUBSYS
    &CELL
      ABC    20.783798 20.784254 50.0 # the a and b vectors slightly
      ALPHA_BETA_GAMMA 90.0 90.0 120.0 # changes from one case to
      PERIODIC  XYZ                    # another, see the details
      MULTIPLE_UNIT_CELL  1 1 1      # in the discusion of chapter 5
    &END CELL
    &KIND H
       BASIS_SET DZVP-MOLOPT-GTH
       POTENTIAL GTH-PBE-q1
    &END KIND
    &KIND C
       BASIS_SET DZVP-MOLOPT-GTH
       POTENTIAL GTH-PBE-q4
    &END KIND
    &KIND O
       BASIS_SET DZVP-MOLOPT-GTH
       POTENTIAL GTH-PBE-q6
    &END KIND
    &KIND Cl
       BASIS_SET DZVP-MOLOPT-GTH
       POTENTIAL GTH-PBE-q7
    &END KIND
    &KIND Sb
       BASIS_SET DZVP-MOLOPT-SR-GTH
       POTENTIAL GTH-PBE-q5
    &END KIND
    &TOPOLOGY
      COORD_FILE_NAME    system.xyz # replace "system" with the
      COORD_FILE_FORMAT  xyz   # correct filename of the xyz file
    &END TOPOLOGY
  &END SUBSYS
```

C.1.2 BSSE calculations

C.1.2.1 BSSE Input example

```
&GLOBAL
...
  RUN_TYPE  BSSE  # notice the different run type
&END GLOBAL
```

```
&DFT
 ...
 &BSSE
  &FRAGMENT
    LIST 1..50
  &END FRAGMENT
  &FRAGMENT
    LIST 51..72
  &END FRAGMENT
  &CONFIGURATION
    GLB_CONF 1 0
    SUB_CONF 1 0
    CHARGE 0
    MULTIPLICITY 2
  &END CONFIGURATION
  &CONFIGURATION
    GLB_CONF 0 1
    SUB_CONF 0 1
    CHARGE 0
    MULTIPLICITY 1
  &END CONFIGURATION
  &CONFIGURATION
    GLB_CONF 1 1
    SUB_CONF 1 0
    CHARGE 0
    MULTIPLICITY 2
  &END CONFIGURATION
  &CONFIGURATION
    GLB_CONF 1 1
    SUB_CONF 0 1
    CHARGE 0
    MULTIPLICITY 1
  &END CONFIGURATION
  &CONFIGURATION
    GLB_CONF 1 1
    SUB_CONF 1 1
    CHARGE 0
    MULTIPLICITY 2
  &END CONFIGURATION
 &END BSSE
 ...
&END DFT
```

C.1.2.2 BSSE Output example

```
 ...
 ...
--------------------------------------------------------------------------------
-                                 BSSE RESULTS
-
-           CP-corrected Total energy:      -470.367376
-
-                 1-body contribution:      -307.728618
-                 1-body contribution:      -162.589266
-
-                 2-body contribution:        -0.049492
-           BSSE-free interaction energy:        -0.049492
--------------------------------------------------------------------------------
...
...
```

D Publications

D.1 Related to The Current Thesis

D.1.1 Published

- Moyassar Meshhal, and Oliver Kühn. “Diffusion of Water Confined between Graphene Oxide Layers: Implications for Membrane Filtration.” ACS Applied Nano Materials 5.8 (2022): 11119-11128.

D.1.2 In preparation

- Moyassar Meshhal, Ashour Ahmed, Oliver Kühn, Saadullah Aziz, Mohamed F. Shibl, and Kamal Soliman. “Two-dimensional Antimonene as a promising candidate for Dioxin capture.” (*In preparation*; a primary version is available on ChemRxiv: `https://doi.org/10.26434/chemrxiv-2023-f5ktf`)
- Moyassar Meshhal, Ashour Ahmed, Oliver Kühn. “Nanoplastics-Graphene interaction in solution.” (*In preparation*).

D.2 Other Publications

- Moyassar M. Meshhal, Safinaz H. El-Demerdash, and Ahmed M. El-Nahas. ”A thermochemical computational study on hydroxyquinolines and their azulene analogues.” Journal of Molecular Structure 1183 (2019): 70-77.
- Moyassar M. Meshhal, Mohamed F. Shibl, Safinaz H. El-Demerdash, and Ahmed M. El-Nahas. ”A computational study on molecular structure and stability of tautomers of dipyrrole-based phenanthroline analogue.” Computational and Theoretical Chemistry 1145 (2018): 6-14.

Bibliography

Abraham, M. J., Murtola, T., Schulz, R., Páll, S., Smith, J. C., Hess, B., et al. (2015). Gromacs: High performance molecular simulations through multi-level parallelism from laptops to supercomputers. *SoftwareX* 1, 19–25

Akinwande, D., Brennan, C. J., Bunch, J. S., Egberts, P., Felts, J. R., Gao, H., et al. (2017). A review on mechanics and mechanical properties of 2d materials—graphene and beyond. *Extreme Mechanics Letters* 13, 42–77

Andrady, A. L. (2011). Microplastics in the marine environment. *Marine pollution bulletin* 62, 1596–1605

Androulidakis, C., Zhang, K., Robertson, M., and Tawfick, S. (2018). Tailoring the mechanical properties of 2d materials and heterostructures. *2D Materials* 5, 032005

Bafekry, A., Ghergherehchi, M., and Shayesteh, S. F. (2019). Tuning the electronic and magnetic properties of antimonene nanosheets via point defects and external fields: first-principles calculations. *Physical Chemistry Chemical Physics* 21, 10552–10566

Baghsiyahi, F. B. and Yeganeh, M. (2020). The effect of strain on the zigzag and armchair phosphorene nanoribbon. *Physica E: Low-dimensional Systems and Nanostructures* 121, 114088

Baho, D. L., Bundschuh, M., and Futter, M. N. (2021). Microplastics in terrestrial ecosystems: Moving beyond the state of the art to minimize the risk of ecological surprise. *Global Change Biology* 27, 3969–3986

Bannwarth, C., Caldeweyher, E., Ehlert, S., Hansen, A., Pracht, P., Seibert, J., et al. (2021). Extended tight-binding quantum chemistry methods. *Wiley Interdisciplinary Reviews: Computational Molecular Science* 11, e1493

Barbosa, F., Adeyemi, J. A., Bocato, M. Z., Comas, A., and Campiglia, A. (2020). A critical viewpoint on current issues, limitations, and future research needs on micro-and nanoplastic studies: From the detection to the toxicological assessment. *Environmental Research* 182, 109089

Bianco, E., Butler, S., Jiang, S., Restrepo, O. D., Windl, W., and Goldberger, J. E. (2013). Stability and exfoliation of germanane: a germanium graphane analogue. *ACS nano* 7, 4414–4421

Bläsing, M. and Amelung, W. (2018). Plastics in soil: Analytical methods and possible sources. *Science of the total environment* 612, 422–435

Boer, F., Van Remoortere, F., North, P., and Neuman, M. (1972). The crystal and molecular structure of 2, 3, 7, 8-tetrachlorodibenzo-p-dioxin. *Acta Crystallographica Section B: Structural Crystallography and Crystal Chemistry* 28, 1023–1029

Brewer, A., Dror, I., and Berkowitz, B. (2020). The mobility of plastic nanoparticles in aqueous and soil environments: a critical review. *ACS ES&T Water* 1, 48–57

Buchsteiner, A., Lerf, A., and Pieper, J. (2006). Water dynamics in graphite oxide investigated with neutron scattering. *The Journal of Physical Chemistry B* 110, 22328–22338

Bussi, G., Donadio, D., and Parrinello, M. (2007). Canonical sampling through velocity rescaling. *The Journal of chemical physics* 126, 014101

Chen, B., Jiang, H., Liu, X., and Hu, X. (2017a). Molecular insight into water desalination across multilayer graphene oxide membranes. *ACS applied materials & interfaces* 9, 22826–22836

Chen, B., Jiang, H., Liu, X., and Hu, X. (2017b). Observation and Analysis of Water Transport through Graphene Oxide Interlamination. *The Journal of Physical Chemistry C* 121, 1321–1328. doi:10.1021/acs.jpcc.6b09753. Publisher: American Chemical Society

Chen, X., Ponraj, J. S., Fan, D., and Zhang, H. (2020). An overview of the optical properties and applications of black phosphorus. *Nanoscale* 12, 3513–3534

Choi, J., Choi, W., and Mhin, B. J. (2004). Solvent-specific photolytic behavior of octachlorodibenzo-p-dioxin. *Environmental science & technology* 38, 2082–2088

Choi, W., Choudhary, N., Han, G. H., Park, J., Akinwande, D., and Lee, Y. H. (2017). Recent development of two-dimensional transition metal dichalcogenides and their applications. *Materials Today* 20, 116–130

Choi, W., Hong, S. J., Chang, Y.-S., and Cho, Y. (2000). Photocatalytic degradation of polychlorinated dibenzo-p-dioxins on tio2 film under uv or solar light irradiation. *Environmental science & technology* 34, 4810–4815

Cohen-Tanugi, D., Lin, L.-C., and Grossman, J. C. (2016). Multilayer nanoporous graphene membranes for water desalination. *Nano letters* 16, 1027–1033

Csonka, G. I., Perdew, J. P., Ruzsinszky, A., Philipsen, P. H., Lebègue, S., Paier, J., et al. (2009). Assessing the performance of recent density functionals for bulk solids. *Physical Review B* 79, 155107

Cui, T., Mukherjee, S., Onodera, M., Wang, G., Kumral, B., Islam, A., et al. (2022). Mechanical reliability of monolayer mos2 and wse2. *Matter* 5, 2975–2989

David, R. and Kumar, R. (2021). Reactive events at the graphene oxide–water interface. *Chem. Commun* 57, 11697–11700

Delhaes, P. (2000). *Graphite and precursors*, vol. 1 (CRC Press)

Dettmann, L. F., Kühn, O., and Ahmed, A. A. (2021). Coarse-grained molecular dynamics simulations of nanoplastics interacting with a hydrophobic environment in aqueous solution. *RSC advances* 11, 27734–27744

Devanathan, R., Chase-Woods, D., Shin, Y., and Gotthold, D. W. (2016). Molecular dynamics simulations reveal that water diffusion between graphene oxide layers is slow. *Scientific reports* 6, 1–8

Di, J., Xiong, J., Li, H., and Liu, Z. (2018). Ultrathin 2d photocatalysts: electronic-structure tailoring, hybridization, and applications. *Advanced materials* 30, 1704548

Dreyer, D. R., Park, S., Bielawski, C. W., and Ruoff, R. S. (2010). The chemistry of graphene oxide. *Chemical society reviews* 39, 228–240

Duan, H., Wang, D., Gou, J., Guo, F., Jie, W., and Hao, J. (2023). Memristors based on 2d mose 2 nanosheets as artificial synapses and nociceptors for neuromorphic computing. *Nanoscale*

Ermolaev, G. A., Stebunov, Y. V., Vyshnevyy, A. A., Tatarkin, D. E., Yakubovsky, D. I., Novikov, S. M., et al. (2020). Broadband optical properties of monolayer and bulk mos2. *npj 2D Materials and Applications* 4, 21

Fagan, S. B., Santos, E., Souza Filho, A., Mendes Filho, J., and Fazzio, A. (2007). Ab initio study of 2, 3, 7, 8-tetrachlorinated dibenzo-p-dioxin adsorption on single wall carbon nanotubes. *Chemical Physics Letters* 437, 79–82

Falomir, H., Loewe, M., Muñoz, E., and Raya, A. (2018). Optical conductivity and transparency in an effective model for graphene. *Physical Review B* 98, 195430

Fernandez-Gonzalez, R., Yebra-Pimentel, I., Martinez-Carballo, E., and Simal-Gandara, J. (2015). A critical review about human exposure to polychlorinated dibenzo-p-dioxins (pcdds), polychlorinated dibenzofurans (pcdfs) and polychlorinated biphenyls (pcbs) through foods. *Critical reviews in food science and nutrition* 55, 1590–1617

Fotopoulou, K. N. and Karapanagioti, H. K. (2019). Degradation of various plastics in the environment. *Hazardous chemicals associated with plastics in the marine environment* , 71–92

Free, C. M., Jensen, O. P., Mason, S. A., Eriksen, M., Williamson, N. J., and Boldgiv, B. (2014). High-levels of microplastic pollution in a large, remote, mountain lake. *Marine pollution bulletin* 85, 156–163

Fu, W., Yang, S., Yang, H., Guo, B., and Huang, Z. (2019). 2d amorphous mos 3 nanosheets with porous network structures for scavenging toxic metal ions from synthetic acid mine drainage. *Journal of Materials Chemistry A* 7, 18799–18806

Galashev, A. and Vorob'ev, A. (2021). First principle modeling of a silicene anode for lithium ion batteries. *Electrochimica Acta* 378, 138143

Ganji, M. D., Alinezhad, H., Soleymani, E., and Tajbakhsh, M. (2015). Adsorption of tcdd molecule onto cnts and bnnts: Ab initio van der waals density-functional study. *Physica E: Low-dimensional Systems and Nanostructures* 67, 105–111

Geyer, J., Jambeck, J., and Lavender, K. (2017). Production, use, and fate of all plastics ever made, law sci. *Adv* 3, e1700782

Ghorbani-Asl, M., Kuc, A., Miró, P., and Heine, T. (2016). A single-material logical junction based on 2d crystal pds2. *Advanced Materials* 28, 853–856

Giese, K., Petković, M., Naundorf, H., and Kühn, O. (2006). Multidimensional quantum dynamics and infrared spectroscopy of hydrogen bonds. *Phys. Rep.* 430, 211–276

Gigault, J., Pedrono, B., Maxit, B., and Ter Halle, A. (2016). Marine plastic litter: the unanalyzed nano-fraction. *Environmental science: nano* 3, 346–350

Glavin, N. R., Rao, R., Varshney, V., Bianco, E., Apte, A., Roy, A., et al. (2020). Emerging applications of elemental 2d materials. *Advanced Materials* 32, 1904302

Goedecker, S., Teter, M., and Hutter, J. (1996). Separable dual-space gaussian pseudopotentials. *Phys. Rev. B* 54, 1703

Gogoi, A., Anki Reddy, K., and Mondal, P. (2018). Multilayer Graphene Oxide Membrane in Forward Osmosis: Molecular Insights. *ACS Applied Nano Materials* 1, 4450–4460. doi:10.1021/acsanm.8b00709. Publisher: American Chemical Society

Goharshadi, E. K., Akhlamadi, G., and Mahdizadeh, S. J. (2015). Investigation of graphene oxide nanosheets dispersion in water based on solubility parameters: a molecular dynamics simulation study. *RSC Advances* 5, 106421–106430. doi: 10.1039/C5RA19932H. Publisher: The Royal Society of Chemistry

Gómez-Navarro, C., Meyer, J. C., Sundaram, R. S., Chuvilin, A., Kurasch, S., Burghard, M., et al. (2010). Atomic structure of reduced graphene oxide. *Nano letters* 10, 1144–1148

Gregory, M. R. (2009). Environmental implications of plastic debris in marine settings—entanglement, ingestion, smothering, hangers-on, hitch-hiking and alien invasions. *Philosophical Transactions of the Royal Society B: Biological Sciences* 364, 2013–2025

Grimme, S., Bannwarth, C., and Shushkov, P. (2017). A robust and accurate tight-binding quantum chemical method for structures, vibrational frequencies, and noncovalent interactions of large molecular systems parametrized for all spd-block elements (z= 1–86). *Journal of chemical theory and computation* 13, 1989–2009

Grimme, S., Ehrlich, S., and Goerigk, L. (2011). Effect of the damping function in dispersion corrected density functional theory. *Journal of computational chemistry* 32, 1456–1465

Gu, J., Du, Z., Zhang, C., Ma, J., Li, B., and Yang, S. (2017). Liquid-phase exfoliated metallic antimony nanosheets toward high volumetric sodium storage. *Advanced Energy Materials* 7, 1700447

Hassan, J. Z., Raza, A., Babar, Z. U. D., Qumar, U., Kaner, N. T., and Cassinese, A. (2023). 2d material-based sensing devices: an update. *Journal of Materials Chemistry A*

He, H., Klinowski, J., Forster, M., and Lerf, A. (1998). A new structural model for graphite oxide. *Chemical physics letters* 287, 53–56

He, H., Riedl, T., Lerf, A., and Klinowski, J. (1996). Solid-state nmr studies of the structure of graphite oxide. *The Journal of physical chemistry* 100, 19954–19958

Heine, T. (2015). Transition metal chalcogenides: ultrathin inorganic materials with tunable electronic properties. *Accounts of chemical research* 48, 65–72

Hilarides, R. J., Gray, K. A., Guzzetta, J., Cortellucci, N., and Sommer, C. (1996). Feasibility, system design, and economic evaluation of radiolytic degradation of 2, 3, 7, 8-tetrachlorodibenzo-p-dioxin on soil. *Water environment research* 68, 178–187

Hong, L. and Lei, J. (2009). Scaling law for the radius of gyration of proteins and its dependence on hydrophobicity. *Journal of Polymer Science Part B: Polymer Physics* 47, 207–214

Hou, D. and Yang, T. (2018). A reactive molecular dynamics study of graphene oxide sheets in different saturated states: structure, reactivity and mechanical properties. *Physical Chemistry Chemical Physics* 20, 11053–11066

Humphrey, W., Dalke, A., and Schulten, K. (1996). Vmd: visual molecular dynamics. *Journal of molecular graphics* 14, 33–38

Hung, P. C., Chen, Q. H., and Chang, M. B. (2013). Pyrolysis of mwi fly ash–effect on dioxin-like congeners. *Chemosphere* 92, 857–863

Hutter, J., Iannuzzi, M., Schiffmann, F., and VandeVondele, J. (2014). cp2k: atomistic simulations of condensed matter systems. *Wiley Interdisciplinary Reviews: Computational Molecular Science* 4, 15–25

Island, J. O., Biele, R., Barawi, M., Clamagirand, J. M., Ares, J. R., Sánchez, C., et al. (2016). Titanium trisulfide (tis3): a 2d semiconductor with quasi-1d optical and electronic properties. *Scientific reports* 6, 22214

Jeffrey, G. A. and Jeffrey, G. A. (1997). *An introduction to hydrogen bonding*, vol. 12 (Oxford University Press New York)

Ji, J., Song, X., Liu, J., Yan, Z., Huo, C., Zhang, S., et al. (2016). Two-dimensional antimonene single crystals grown by van der waals epitaxy. *Nature communications* 7, 13352

Jia, B. (2019). 2d optical materials and the implications for photonics. *APL Photonics* 4

Jiang, H., Zheng, L., Liu, Z., and Wang, X. (2020). Two-dimensional materials: From mechanical properties to flexible mechanical sensors. *InfoMat* 2, 1077–1094

Jin, Y.-q., Ma, X.-j., Jiang, X.-g., Liu, H.-m., Li, X.-d., and Yan, J.-h. (2013). Hydrothermal degradation of polychlorinated dibenzo-p-dioxins and polychlorinated dibenzofurans in fly ash from municipal solid waste incineration under non-oxidative and oxidative conditions. *Energy & fuels* 27, 414–420

Jo, S., Kim, T., Iyer, V. G., and Im, W. (2008). Charmm-gui: a web-based graphical user interface for charmm. *Journal of computational chemistry* 29, 1859–1865

Joshi, R., Carbone, P., Wang, F.-C., Kravets, V. G., Su, Y., Grigorieva, I. V., et al. (2014). Precise and ultrafast molecular sieving through graphene oxide membranes. *science* 343, 752–754

Kang, H. S. (2005). Theoretical study of binding of metal-doped graphene sheet and carbon nanotubes with dioxin. *Journal of the American Chemical Society* 127, 9839–9843

Kang, M., Kim, B., Ryu, S. H., Jung, S. W., Kim, J., Moreschini, L., et al. (2017). Universal mechanism of band-gap engineering in transition-metal dichalcogenides. *Nano letters* 17, 1610–1615

Khannanov, A., Gareev, B., Batalin, G., Amirova, L. M., and Dimiev, A. M. (2019). Counterion concentration profiles at the graphene oxide/water interface. *Langmuir* 35, 13469–13479. doi:10.1021/acs.langmuir.9b01882

Khoei, A. and Khorrami, M. (2016). Mechanical properties of graphene oxide: A molecular dynamics study. *Fullerenes, Nanotubes and Carbon Nanostructures* 24, 594–603

Kim, J., Lim, Y. R., Yoon, Y., Song, W., Park, B. K., Lim, J., et al. (2019). A facile synthetic route to tungsten diselenide using a new precursor containing a long alkyl chain cation for multifunctional electronic and optoelectronic applications. *RSC advances* 9, 6169–6176

Koenig, S. P., Doganov, R. A., Schmidt, H., Castro Neto, A., and Özyilmaz, B. (2014). Electric field effect in ultrathin black phosphorus. *Applied Physics Letters* 104

Kokilathasan, N. and Dittrich, M. (2022). Nanoplastics: detection and impacts in aquatic environments–a review. *Science of The Total Environment* 849, 157852

Krack, M. (2005). Pseudopotentials for h to kr optimized for gradient-corrected exchange-correlation functionals. *Theoretical Chemistry Accounts* 114, 145–152

Kühne, T. D., Iannuzzi, M., Del Ben, M., Rybkin, V. V., Seewald, P., Stein, F., et al. (2020). Cp2k: An electronic structure and molecular dynamics software package-quickstep: Efficient and accurate electronic structure calculations. *The Journal of Chemical Physics* 152, 194103

Kulkarni, P. S., Crespo, J. G., and Afonso, C. A. (2008). Dioxins sources and current remediation technologies—a review. *Environment international* 34, 139–153

Kumar, N., Gusain, R., and Ray, S. S. (2023a). *Two-Dimensional Materials for Environmental Applications*, vol. 332 (Springer Nature)

Kumar, S., Himanshi, Prakash, J., Verma, A., Suman, Jasrotia, R., et al. (2023b). A review on properties and environmental applications of graphene and its derivative-based composites. *Catalysts* 13, 111

Kumbhakar, P., Chowde Gowda, C., and Tiwary, C. S. (2021). Advance optical properties and emerging applications of 2d materials. *Frontiers in Materials* 8, 721514

Kumbhakar, P., Jayan, J. S., Madhavikutty, A. S., Sreeram, P., Appukuttan, S., Ito, T., et al. (2023). Prospective applications of two-dimensional materials beyond laboratory frontiers: A review. *Iscience*

Lai, H., Liu, X., and Qu, M. (2022). Nanoplastics and human health: hazard identification and biointerface. *Nanomaterials* 12, 1298

Le Lay, G., Aufray, B., Léandri, C., Oughaddou, H., Biberian, J.-P., De Padova, P., et al. (2009). Physics and chemistry of silicene nano-ribbons. *Applied Surface Science* 256, 524–529

Lee, J., Cheng, X., Jo, S., MacKerell, A. D., Klauda, J. B., and Im, W. (2016). Charmm-gui input generator for namd, gromacs, amber, openmm, and charmm/openmm simulations using the charmm36 additive force field. *Biophysical journal* 110, 641a

Lerf, A., He, H., Forster, M., and Klinowski, J. (1998). Structure of graphite oxide revisited. *The Journal of Physical Chemistry B* 102, 4477–4482

Li, L., Yu, Y., Ye, G. J., Ge, Q., Ou, X., Wu, H., et al. (2014). Black phosphorus field-effect transistors. *Nature nanotechnology* 9, 372–377

Li, Z., Tan, X., Li, P., Kalisvaart, P., Janish, M. T., Mook, W. M., et al. (2015). Coupling in situ tem and ex situ analysis to understand heterogeneous sodiation of antimony. *Nano Letters* 15, 6339–6348. doi:10.1021/acs.nanolett.5b03373. PMID: 26389786

Lim, D.-H., Negreira, A. S., and Wilcox, J. (2011). Dft studies on the interaction of defective graphene-supported fe and al nanoparticles. *The Journal of Physical Chemistry C* 115, 8961–8970

Lippert, B. G., PARRINELLO, J. H., and MICHELE (1997). A hybrid gaussian and plane wave density functional scheme. *Molecular Physics* 92, 477–488

Liu, H., Neal, A. T., Zhu, Z., Luo, Z., Xu, X., Tománek, D., et al. (2014). Phosphorene: an unexplored 2d semiconductor with a high hole mobility. *ACS nano* 8, 4033–4041

Liu, J., Yang, Z., Wang, J., Gu, L., Maier, J., and Yu, Y. (2015). Three-dimensionally interconnected nickel–antimony intermetallic hollow nanospheres as anode material for high-rate sodium-ion batteries. *Nano Energy* 16, 389–398

Liu, X. and Zhang, Y.-W. (2018). Thermal properties of transition-metal dichalcogenide. *Chinese Physics B* 27, 034402

Luo, H., Auchterlonie, G., and Zou, J. (2017). A thermodynamic structural model of graphene oxide. *Journal of Applied Physics* 122, 145101

MacKerell Jr, A. D., Bashford, D., Bellott, M., Dunbrack Jr, R. L., Evanseck, J. D., Field, M. J., et al. (1998). All-atom empirical potential for molecular modeling and dynamics studies of proteins. *The journal of physical chemistry B* 102, 3586–3616

Martínez, L., Andrade, R., Birgin, E. G., and Martínez, J. M. (2009). Packmol: a package for building initial configurations for molecular dynamics simulations. *Journal of computational chemistry* 30, 2157–2164

Mas-Balleste, R., Gomez-Navarro, C., Gomez-Herrero, J., and Zamora, F. (2011). 2d materials: to graphene and beyond. *Nanoscale* 3, 20–30

Mattsson, K., Jocic, S., Doverbratt, I., and Hansson, L.-A. (2018). Nanoplastics in the aquatic environment. *Microplastic contamination in aquatic environments* , 379–399

Memisoglu, G., Murugesan, R. C., Zubia, J., and Rozhin, A. G. (2023). Graphene nanocomposite membranes: Fabrication and water treatment applications. *Membranes* 13, 145

Mills, R. (1973). Self-diffusion in normal and heavy water in the range 1-45. deg. *The Journal of Physical Chemistry* 77, 685–688

Mindess, S., Young, J., and Darwin, D. (2003). Response of concrete to stress. *Concrete, 2nd ed. Upper Saddle River, NJ: Prentice Hall* , 303–362

Mizukami, Y. (2005). Frontier density pattern of dioxins. *Journal of Molecular Structure: THEOCHEM* 713, 15–19

Mohan, V. B., Lau, K.-t., Hui, D., and Bhattacharyya, D. (2018). Graphene-based materials and their composites: A review on production, applications and product limitations. *Composites Part B: Engineering* 142, 200–220

Mouhat, F., Coudert, F.-X., and Bocquet, M.-L. (2020). Structure and chemistry of graphene oxide in liquid water from first principles. *Nature Communications* 11, 1566. doi:10.1038/s41467-020-15381-y

Nair, R., Wu, H., Jayaram, P., Grigorieva, I., and Geim, A. (2012). Unimpeded permeation of water through helium-leak–tight graphene-based membranes. *Science* 335, 442–444

Navarro-Moratalla, E., Island, J. O., Manas-Valero, S., Pinilla-Cienfuegos, E., Castellanos-Gomez, A., Quereda, J., et al. (2016). Enhanced superconductivity in atomically thin tas2. *Nature communications* 7, 11043

Novoselov, K. S., Geim, A. K., Morozov, S. V., Jiang, D.-e., Zhang, Y., Dubonos, S. V., et al. (2004). Electric field effect in atomically thin carbon films. *science* 306, 666–669

Novoselov, K. S., Jiang, D., Schedin, F., Booth, T., Khotkevich, V., Morozov, S., et al. (2005). Two-dimensional atomic crystals. *Proceedings of the National Academy of Sciences* 102, 10451–10453

Nurhuda, M., Perry, C. C., and Addicoat, M. A. (2022). Performance of gfn1-xtb for periodic optimization of metal organic frameworks. *Physical Chemistry Chemical Physics* 24, 10906–10914

Orasugh, J. T., Temane, L. T., and Ray, S. S. (2023). Application of mxenes in water purification, co2 capture and conversion. In *Two-Dimensional Materials for Environmental Applications* (Springer). 17–74

Orts Mercadillo, V., Chan, K. C., Caironi, M., Athanassiou, A., Kinloch, I. A., Bissett, M., et al. (2022). Electrically conductive 2d material coatings for flexible and stretchable electronics: a comparative review of graphenes and mxenes. *Advanced Functional Materials* 32, 2204772

Oyedele, A. D., Yang, S., Liang, L., Puretzky, A. A., Wang, K., Zhang, J., et al. (2017). Pdse2: pentagonal two-dimensional layers with high air stability for electronics. *Journal of the American Chemical Society* 139, 14090–14097

Paci, J. T., Belytschko, T., and Schatz, G. C. (2007). Computational studies of the structure, behavior upon heating, and mechanical properties of graphite oxide. *Journal of Physical Chemistry C* 111, 18099–18111

Pacile, D., Meyer, J., Girit, Ç., and Zettl, A. (2008). The two-dimensional phase of boron nitride: Few-atomic-layer sheets and suspended membranes. *Applied Physics Letters* 92

Palanisami, N., Chung, S. J., and Moon, I. S. (2015). Cerium (iv)-mediated electrochemical oxidation process for removal of polychlorinated dibenzo-p-dioxins and dibenzofurans. *Journal of Industrial and Engineering Chemistry* 28, 28–31

Pan, W., Qi, Y., Wang, R., Han, Z., Zhang, D., and Zhan, J. (2013). Adsorption of tcdd with 1-butyl-3-methylimidazolium dicyanamide ionic liquid: A combined molecular dynamics simulation and quantum chemistry study. *Chemosphere* 91, 157–164

Pan, W., Zhang, D., and Zhan, J. (2011). Theoretical investigation on the inclusion of tcdd with β-cyclodextrin by performing qm calculations and md simulations. *Journal of hazardous materials* 192, 1780–1786

Papageorgiou, D. G., Kinloch, I. A., and Young, R. J. (2017). Mechanical properties of graphene and graphene-based nanocomposites. *Progress in materials science* 90, 75–127

Perdew, J. P., Burke, K., and Ernzerhof, M. (1996). Generalized gradient approximation made simple. *Physical review letters* 77, 3865

Pham, T. A., Ogitsu, T., Lau, E. Y., and Schwegler, E. (2016). Structure and dynamics of aqueous solutions from PBE-based first-principles molecular dynamics simulations. *J. Chem. Phys.* 145, 154501

Qin, M.-Z., Fu, W.-X., Guo, H., Niu, C.-G., Huang, D.-W., Liang, C., et al. (2021). 2d/2d heterojunction systems for the removal of organic pollutants: A review. *Advances in Colloid and Interface Science* 297, 102540

Qin, W., Li, X., Bian, W.-W., Fan, X.-J., and Qi, J.-Y. (2010). Density functional theory calculations and molecular dynamics simulations of the adsorption of biomolecules on graphene surfaces. *Biomaterials* 31, 1007–1016

Raidongia, K., Gomathi, A., and Rao, C. (2010). Synthesis and characterization of nanoparticles, nanotubes, nanopans, and graphene-like structures of boron nitride. *Israel Journal of Chemistry* 50, 399–404

Rama, P., Gallego-Urrea, J. A., and Abbas, Z. (2023). Interfacial interactions of humic acids with polystyrene nano-plastics in aqueous/ionic environments: a molecular dynamics exploration. *Environmental Science: Nano* 10, 1385–1393

Ramasamy, B. S. S. and Palanisamy, S. (2021). A review on occurrence, characteristics, toxicology and treatment of nanoplastic waste in the environment. *Environmental Science and Pollution Research* 28, 43258–43273

Rao, C. and Nag, A. (2010). Inorganic analogues of graphene. *European Journal of Inorganic Chemistry* 2010, 4244–4250

Rao, C., Ramakrishna Matte, H., and Maitra, U. (2013). Graphene analogues of inorganic layered materials. *Angewandte Chemie International Edition* 52, 13162–13185

Ribeiro-Brasil, D. R. G., Brasil, L. S., Veloso, G. K. O., de Matos, T. P., de Lima, E. S., and Dias-Silva, K. (2022). The impacts of plastics on aquatic insects. *Science of The Total Environment* 813, 152436

Sadri, S. S. and Thompson, R. C. (2014). On the quantity and composition of floating plastic debris entering and leaving the tamar estuary, southwest england. *Marine pollution bulletin* 81, 55–60

Saibu, S., Adebusoye, S. A., and Oyetibo, G. O. (2020). Aerobic bacterial transformation and biodegradation of dioxins: a review. *Bioresources and Bioprocessing* 7, 1–21

Samara, F., Ghalayini, T., Abu Farha, N., and Kanan, S. (2020). The photocatalytic degradation of 2, 3, 7, 8-tetrachlorodibenzo-p-dioxin in the presence of silver–titanium based catalysts. *Catalysts* 10, 957

Savazzi, F., Risplendi, F., Mallia, G., Harrison, N. M., and Cicero, G. (2018). Unravelling some of the structure–property relationships in graphene oxide at low degree of oxidation. *J. Phys. Chem. Lett* 9, 1746–1749

Shams, M., Mansukhani, N., Hersam, M. C., Bouchard, D., and Chowdhury, I. (2023). Environmentally sustainable implementations of two-dimensional nanomaterials. *Frontiers in Chemistry* 11, 1132233

Shang, S., Liu, Y., Liu, M., Bai, Y., Wang, X., Wu, B., et al. (2022). Studying the adsorption mechanisms of nanoplastics on covalent organic frameworks via molecular dynamics simulations. *Journal of Hazardous Materials* 421, 126796

Sheehy, D. E. and Schmalian, J. (2009). Optical transparency of graphene as determined by the fine-structure constant. *Physical Review B* 80, 193411

Sheka, E. F. and Popova, N. A. (2013). Molecular theory of graphene oxide. *Physical Chemistry Chemical Physics* 15, 13304–13322. doi:10.1039/C3CP00032J

Shen, C. and Oyadiji, S. O. (2020). The processing and analysis of graphene and the strength enhancement effect of graphene-based filler materials: A review. *Materials Today Physics* 15, 100257

Simon, S. H. (2013). *The Oxford solid state basics* (OUP Oxford)

Singh, A., Dey, M., and Singh, A. K. (2022). Origin of layer-dependent electrical conductivity of transition metal dichalcogenides. *Physical Review B* 105, 165430

Srivastava, P., Jaiswal, N. K., et al. (2020). First-principles investigation of co2 and nh3 adsorption on antimonene nanoribbons. *Materials Today: Proceedings* 28, 65–69

Stanford, M. G., Rack, P. D., and Jariwala, D. (2018). Emerging nanofabrication and quantum confinement techniques for 2d materials beyond graphene. *npj 2D Materials and Applications* 2, 20

Subasinghege Don, V., David, R., Du, P., Milet, A., and Kumar, R. (2019). Interfacial Water at Graphene Oxide Surface: Ordered or Disordered? *The Journal of Physical Chemistry B* 123, 1636–1649. doi:10.1021/acs.jpcb.8b10987

Sun, X., Shi, L., Huang, H., Song, X., and Ma, T. (2020). Surface engineered 2d materials for photocatalysis. *Chemical Communications* 56, 11000–11013

Surendran, U., Jayakumar, M., Raja, P., Gopinath, G., and Chellam, P. V. (2023). Microplastics in terrestrial ecosystem: Sources and migration in soil environment. *Chemosphere* , 137946

Talyzin, A. V., Hausmaninger, T., You, S., and Szabó, T. (2014). The structure of graphene oxide membranes in liquid water, ethanol and water–ethanol mixtures. *Nanoscale* 6, 272–281

Tan, C., Cao, X., Wu, X.-J., He, Q., Yang, J., Zhang, X., et al. (2017). Recent advances in ultrathin two-dimensional nanomaterials. *Chemical reviews* 117, 6225–6331

Tian, W., Zhang, S., Huo, C., Zhu, D., Li, Q., Wang, L., et al. (2018). Few-layer antimonene: anisotropic expansion and reversible crystalline-phase evolution enable large-capacity and long-life na-ion batteries. *ACS nano* 12, 1887–1893

Trevisan, R., Ranasinghe, P., Jayasundara, N., and Di Giulio, R. T. (2022). Nanoplastics in aquatic environments: impacts on aquatic species and interactions with environmental factors and pollutants. *Toxics* 10, 326

Turunen, M., Brotons-Gisbert, M., Dai, Y., Wang, Y., Scerri, E., Bonato, C., et al. (2022). Quantum photonics with layered 2d materials. *Nature Reviews Physics* 4, 219–236

Ukisu, Y. and Miyadera, T. (2002). Dechlorination of polychlorinated dibenzo-p-dioxins catalyzed by noble metal catalysts under mild conditions. *Chemosphere* 46, 507–510

V. Nagarajan, R. C. (2019). Detection of trace level of hazardous phosgene gas on antimonene nanotube based on first-principles method. *Journal of Molecular Graphics and Modelling* 88, 32–40

Vallejo, M., San Román, M., Irabien, A., and Ortiz, I. (2013). Comparative study of the destruction of polychlorinated dibenzo-p-dioxins and dibenzofurans during fenton and electrochemical oxidation of landfill leachates. *Chemosphere* 90, 132–138

Van Der Spoel, D., Lindahl, E., Hess, B., Groenhof, G., Mark, A. E., and Berendsen, H. J. (2005). Gromacs: fast, flexible, and free. *Journal of computational chemistry* 26, 1701–1718

Van Mourik, T., Wilson, A. K., Peterson, K. A., Woon, D. E., and Dunning Jr, T. H. (1998). The effect of basis set superposition error (bsse) on the convergence of molecular properties calculated with the correlation consistent basis sets. In *Advances in Quantum Chemistry* (Elsevier), vol. 31. 105–135

VandeVondele, J. and Hutter, J. (2007). Gaussian basis sets for accurate calculations on molecular systems in gas and condensed phases. *The Journal of chemical physics* 127

VandeVondele, J., Krack, M., Mohamed, F., Parrinello, M., Chassaing, T., and Hutter, J. (2005). Quickstep: Fast and accurate density functional calculations using a mixed gaussian and plane waves approach. *Computer Physics Communications* 167, 103–128

Vicent-Luna, J. M., Apergi, S., and Tao, S. (2021). Efficient computation of structural and electronic properties of halide perovskites using density functional tight binding: Gfn1-xtb method. *Journal of chemical information and modeling* 61, 4415–4424

Vilela Oliveira, D., Laun, J., Peintinger, M. F., and Bredow, T. (2019). Bsse-correction scheme for consistent gaussian basis sets of double-and triple-zeta valence with polarization quality for solid-state calculations. *Journal of Computational Chemistry* 40, 2364–2376

V. Neklyudov, V., R. Khafizov, N., A. Sedov, I., and M. Dimiev, A. (2017). New insights into the solubility of graphene oxide in water and alcohols. *Physical Chemistry Chemical Physics* 19, 17000–17008. doi:10.1039/C7CP02303K

Wang, J., Liu, X., Li, Y., Powell, T., Wang, X., Wang, G., et al. (2019). Microplastics as contaminants in the soil environment: A mini-review. *Science of the total environment* 691, 848–857

Wang, J., Zhao, X., Wu, F., Niu, L., Tang, Z., Liang, W., et al. (2021a). Characterization, occurrence, environmental behaviors, and risks of nanoplastics in the aquatic environment: Current status and future perspectives. *Fundamental Research* 1, 317–328

Wang, L., Sun, Y., Lee, K., West, D., Chen, Z., Zhao, J., et al. (2010). Stability of graphene oxide phases from first-principles calculations. *Physical Review B* 82, 161406

Wang, X., Yu, X., Song, J., Huang, W., Xiang, Y., Dai, X., et al. (2021b). Two-dimensional semiconducting antimonene in nanophotonic applications–a review. *Chemical Engineering Journal* 406, 126876

Wei, N., Peng, X., and Xu, Z. (2014). Understanding water permeation in graphene oxide membranes. *ACS applied materials & interfaces* 6, 5877–5883

Williams, C. D. and Lísal, M. (2020). Coarse grained models of graphene and graphene oxide for use in aqueous solution. *2D Materials* 7, 025025. doi:10.1088/2053-1583/ab6f0c

Wu, J., Zhai, F., Lu, J., Wu, J., and Feng, X. (2020). Strain-tunable photogalvanic effect in phosphorene. *Materials Today Communications* 24, 101154

Xiao, Y., Zhou, M., Zeng, M., and Fu, L. (2019). Atomic-scale structural modification of 2d materials. *Advanced Science* 6, 1801501

Yan, J.-A. and Chou, M. Y. (2010). Oxidation functional groups on graphene: Structural and electronic properties. *Physical Review B* 82, 125403. doi:10.1103/PhysRevB.82.125403

Yang, L., Song, Y., Mi, W., and Wang, X. (2016). Prediction of spin-dependent electronic structure in 3d-transition-metal doped antimonene. *Applied Physics Letters* 109

Yang, Q., Su, Y., Chi, C., Cherian, C., Huang, K., Kravets, V., et al. (2017). Ultrathin graphene-based membrane with precise molecular sieving and ultrafast solvent permeation. *Nature materials* 16, 1198–1202

Yang, R. T., Long, R. Q., Padin, J., Takahashi, A., and Takahashi, T. (1999). Adsorbents for dioxins: a new technique for sorbent screening for low-volatile organics. *Industrial & engineering chemistry research* 38, 2726–2731

Yeoh, K. H., Yoon, T. L., Ong, D. S., Lim, T. L., et al. (2018). First-principles studies on the superconductivity of aluminene. *Applied Surface Science* 445, 161–166

Yive, N. S. C. K. and Tiroumalechetty, M. (2008). Dioxin levels in fly ash coming from the combustion of bagasse. *Journal of hazardous materials* 155, 179–182

Yu, X., Cheng, H., Zhang, M., Zhao, Y., Qu, L., and Shi, G. (2017). Graphene-based smart materials. *Nature Reviews Materials* 2, 1–13

Zaki, M. R. M. and Aris, A. Z. (2022). An overview of the effects of nanoplastics on marine organisms. *Science of the Total Environment* 831, 154757

Zbyszewski, M., Corcoran, P. L., and Hockin, A. (2014). Comparison of the distribution and degradation of plastic debris along shorelines of the great lakes, north america. *Journal of Great Lakes Research* 40, 288–299

Zhang, H., He, W., Luo, X., Lin, X., and Lu, X. (2014). Adsorption of 2, 3, 7, 8-tetrochlorodibenzo-p-dioxins on intrinsic, defected, and ti (n, ag) doped graphene: A dft study. *Journal of Molecular Modeling* 20, 1–7

Zhang, H.-p., Hou, J.-l., Wang, Y., Tang, P.-p., Zhang, Y.-p., Lin, X.-y., et al. (2017). Adsorption behavior of 2, 3, 7, 8-tetrachlorodibenzo-p-dioxin on pristine and doped black phosphorene: A dft study. *Chemosphere* 185, 509–517

Zhang, T., Gao, X., Li, J., Xiao, L., Gao, H., Zhao, F., et al. (2023). Progress on the application of graphene-based composites toward energetic materials: A review. *Defence Technology*

Zhang, X., Su, G., Lu, J., Yang, W., Zhuang, W., Han, K., et al. (2021). Centimeter-scale few-layer pds2: fabrication and physical properties. *ACS applied materials & interfaces* 13, 43063–43074

Zhao, C., Hirota, K., Taguchi, M., Takigami, M., and Kojima, T. (2007). Radiolytic degradation of octachlorodibenzo-p-dioxin and octachlorodibenzofuran in organic solvents and treatment of dioxin-containing liquid wastes. *Radiation Physics and Chemistry* 76, 37–45

Zhao, L.-D., Chang, C., Tan, G., and Kanatzidis, M. G. (2016). Snse: a remarkable new thermoelectric material. *Energy & Environmental Science* 9, 3044–3060

Zhou, K.-G., Vasu, K., Cherian, C., Neek-Amal, M., Zhang, J. C., Ghorbanfekr-Kalashami, H., et al. (2018a). Electrically controlled water permeation through graphene oxide membranes. *Nature* 559, 236–240

Zhou, Q., Su, X., Yong, Y., Ju, W., Fu, Z., and Li, X. (2018b). Adsorption of 2, 3, 7, 8-tetrachlorodibenzao-p-dioxin (tcdd) on graphane decorated with ni and cu: A dft study. *Vacuum* 149, 53–59

Eidesstattliche Versicherung

Hiermit versichere ich, dass ich die vorliegende Arbeit selbstständig verfasst und keine anderen als die angegebenen Quellen und Hilfsmittel benutzt habe, alle Ausführungen, die anderen Schriften wörtlich oder sinngemäß entnommen wurden, kenntlich gemacht sind und die Arbeit in gleicher oder ähnlicher Fassung noch nicht Bestandteil einer Studien- oder Prüfungsleistung war.

Rostock, 11. Dezember 2023

Moyassar Meshhal